UC Berkeley
UC Berkeley Electronic Theses and Dissertations

Title
Engineering the Magnetoelectric Coupling in Complex Oxides Heterostructures

Permalink
https://escholarship.org/uc/item/0w1689t5

Author
Yi, Di

Publication Date
2015

Peer reviewed|Thesis/dissertation

eScholarship.org Powered by the California Digital Library
University of California

Engineering the Magnetoelectric Coupling in Complex Oxides Heterostructures

by

Di Yi

A dissertation submitted in partial satisfaction of the

requirements for the degree of

Doctor of Philosophy

in

Engineering - Materials Science and Engineering

in the

Graduate Division

of the

University of California, Berkeley

Committee in charge:

Professor Ramamoorthy Ramesh, Chair

Professor Junqiao Wu

Professor Zi Qiang Qiu

Summer 2015

Engineering the Magnetoelectric Coupling in Complex Oxides Heterostructures

Copyright 2015
by
Di Yi

Abstract

Engineering the Magnetoelectric Coupling in Complex Oxides Heterostructures

by

Di Yi

Doctor of Philosophy in Engineering - Materials Science and Engineering

University of California, Berkeley

Professor Ramamoorthy Ramesh, Chair

Multiferroic magnetoelectric (ME) materials, which simultaneously show ferroelectricity and magnetic ordering, have attracted a huge scientific attention due to both the intriguing fundamental importance and the great technological potential, as a result of the coupling between the dual ferroic orderings. However there are only a few single-phase multiferroic materials in nature and the performance is limited by the low ordering temperature, the small polarization/magnetization or the weak coupling efficiency. Another promising pathway to engineer ME coupling is through designing heterostructures. The current studies of ME coupling (electric field control of magnetism) in heterostructures can be divided into 3 routes: (1) Using piezoelectric effects to change the strain (lattice); (2) Using ferroelectric polarization to tune the carriers (charge); (3) Using multiferroic materials to manipulate the moments by magnetic coupling (spin). Previous studies of an all-oxide model heterostructure system that consists of the ferromagnet $La_{0.7}Sr_{0.3}MnO_3$ (LSMO) and the $BiFeO_3$ (BFO) reveals an interesting charge and spin interactions at the interface. Following the same route, the first part of the dissertation focuses on two different pathways to improve the ME coupling in manganite/BFO model system. Chapter 3 demonstrates that the ME coupling in LSMO/BFO is dramatically different by changing the atomic stacking sequence at the interface. In chapter 4, another model system $La_{0.5}Ca_{0.5}MnO_3$ (LCMO), which is at the ferromagnetic/antiferromagnetic phase boundary, is studied instead of LSMO to explore the limit within this route. The results complementarily suggest the importance of a more comprehensive design rule at the atomic scale in order to achieve a better ME coupling efficiency.

Furthermore, although the coupling between the lattice, charge and spin has been intensively studied in terms of ME coupling, the orbital degree of freedom has been neglected so far. In principle, orbital is strongly coupled to lattice. Therefore a large ME coupling could be expected if a strong spin-orbit interaction could be established. The second part of the dissertation concentrates on pursuing this new ideal through two different pathways. Chapter 5 presents a systematic study of the in-situ strain effect on the magnetic and orbital orderings of a model system $Nd_{0.5}Sr_{0.5}MnO_3$. The results demonstrate the close correlation between the orbital ordering parameter and

the strain. However the magnetic ordering parameter is less sensitive to strain in this system. With the implication from chapter 5, 5d transition metal oxide $SrIrO_3$(SIO), which hosts a strong intrinsic spin-orbit coupling due to the large atomic number, is studied in chapter 6. Superlattice LSMO/SIO shows an interesting novel magnetic state with a large orbital momentum in the nominally paramagnetic SIO, which is likely to be a very promising candidate to engineer the ME coupling at the interface.

In summary, our studies on engineering the ME effects in heterostructures have revealed two key implications: 1. in the traditional routes that have been extensively studied, further improvements are possible by carefully engineering the interface; 2. the coupling between spin and orbital degrees of freedom is likely to be another promising route to investigate the ME coupling in heterostructures.

To my family and all my friends,

for their loves and supports

.

Contents

List of Figures

List of Tables

Acknowledgments

I would like to extend my deepest thanks to many truly amazing people for their supports in the last five years. It is my great honor to recognize their contributions to this thesis here.

First of all, I would like to thank my advisor, Professor Ramamoorthy Ramesh for introducing me into such an exciting field. I learned a lot from you during the process of the PhD program, not only the scientific insights you gave but also your never-ending passion and enthusiasm for science. The guidance from you helped me solve many puzzles along the journey whenever I needed. I will always be indebted to you.

I would also like to express my deepest gratitude to Professor Junqiao Wu, Professor Oscar Dubon, Professor Ziqiang Qiu and Professor Elke Arenholz for being on my qualifying exam and dissertation committee and providing important suggestions and comments on my research. Your feedback has been critical to this dissertation and also my graduate career.

I would like to give my special thanks to Professor Pu Yu and Dr.Jian Liu, as my greatest collaborator, mentor and friend. To Pu, thank you for your support when I first joined the group and also the continued advices. To Jian, thank you for your priceless insights from the endless discussions we had during all these years. Without the encouragement, patience and help from you guys, I couldn't have made it this far.

It has been my great honor to work with so many talented colleagues in the CONCEPT lab. I would like to thank the following previous and present members of the group for your help: To Dr.Ying-Hao Chu, Dr.Qing He and Dr.Jinxing Zhang, thank you for mentoring me in my early years of academic career and the close collaborations ever since then; To Dr.Morgan Trassin and Dr.Jayakanth Ravichandran, thank you for sharing your valuable experience for thin film deposition; To Dr.John Heron, thank you very much for your great support in device fabrication as well as many advices as a senior graduate student; To Dr.Weidong Luo, thank you for your valuable discussions and the physical insights; To Dr.Xavi Marti, thank you for sharing so many intriguing ideals and the fruitful collaborations; To Dr.Jiunhaw Chu, thank you for the value physical insights and the new perspective you brought to me and wish you a success as a young faculty; To Dr.Claudy Serrao, thank you very much for your expertise in solid state synthesis; To Shang-Lin Hsu, thank you for the contribution of wonderful TEM studies in the work. I especially want to thank Ajay Yadav, James Clarkson and Anthony Diamond for sharing the same memories of PhD studies and the support and friendship all these years. Of course there are many more people that I should enlist here: Dr.Jan Seidel, Dr.Shwaran Mishra, Dr.Dennis Meier, Dr.Seung-Yeul Yang, Dr.Guneeta Singh Bhalla, Dr.Tianliang Qu, Dr.Asif Islam Khan, Suraj Cheema, Oleg Sapunkov and Ryan Paull. Thank all of you for your help and support all along the way.

Also I would like to acknowledge the efforts of the following individuals and groups at various other institutions around the world for the productive collaborations: Professor Elke Arenholz and Dr.Padraic Shafer at Advanced Light Source at Lawrence Berkeley National Laboratory for the help of soft X-ray absorption and scattering measurements; Dr.Evguenia Karapetrova, Dr.Jong-woo Kim, Dr.Philip Ryan and Dr.Yongseong Choi at Advanced Photon Source at Argonne National Laboratory for the help of hard X-ray absorption and scattering measurements; Professor Yi-Chun Chen at National Cheng Kung University for macroscopic switching of ferroelectric thin films; Dr.Satoshi Okamoto at ORNL for valuable discussions about strong correlated physics as well as providing theoretical calculations for our work; Dr.Stephen Wu, Dr.Shane Cybart and Professor Robert Dynes at University of California at Berkeley and San Diego for magnetotransport measurements; Dr.Lipeng Zhang and Professor Haixuan Xu at University of Tennessee for first principal calculations in the superlattice work.

Last but not the least, I want to express my deepest gratitude to my family. I especially want to thank my parents for their understanding and support from when I was young. I can still remember clearly right now all the amazing things I saw in lab as a child, which attracted me into the wonderful world of science ever since then. I am also deeply grateful to Wenwen for her love and support all these years.

Chapter 1

Introduction

This chapter provides a brief introduction to the background and several key concepts to understand the ideal of the magnetoelectric coupling in complex oxides heterostructures. Firstly, a brief review of the history and the current research on the magnetoelectric/multiferroic materials is presented. Following is the physical background of the complex transition metal oxides, which provides the prerequisite knowledge for the subsequent discussions. The next section covers the different strategies to investigate the magnetoelectric coupling in oxides heterostructures, which serve as the central design rule for the dissertation. Finally this chapter ends with a summary of the organization of this dissertation.

1.1 A brief review of magnetoelectrics and multiferroics

This section covers a brief review of the history of the research on the magnetoelectric effects from the linear magnetoelectric coupling at the early age to the renaissance of magnetoelectrics/multiferroics recently. Then two types of single-component multiferroics will be presented.

1.1.1 History of the magnetoelectric effects

The magnetoelectric (ME) effect, by its most general definition, denominates the coupling between electric and magnetic fields in matter. The early research on ME coupling can date back to more than a century ago. A general consensus of the early stage works is that the ME response is only allowed in time-asymmetric media, which can be extrinsically realized through applying magnetic field or intrinsically occur in the form of long-range magnetic ordering [1]. One of the early model systems that show the magnetoelectric coupling effect, antiferromagnetic Cr_2O_3, was proposed by Dzyaloshinskii in the early 60s [2] and later experimentally confirmed [3,4]. Exchange

bias was observed in ferromagnet/Cr_2O_3 heterostructure [5], which was promising for the useful magnetoelectric devices. Later on, the exchange bias was proved to be isothermally electrically switchable by applying the electric and magnetic field simultaneously at ambient condition [6]. The sign of exchange bias was deterministically controlled by the term E·H (figure 1.1(a)), which is due to the switchable net moments at the surface of the antiferromagnetic domains (figure 1.1(b)).

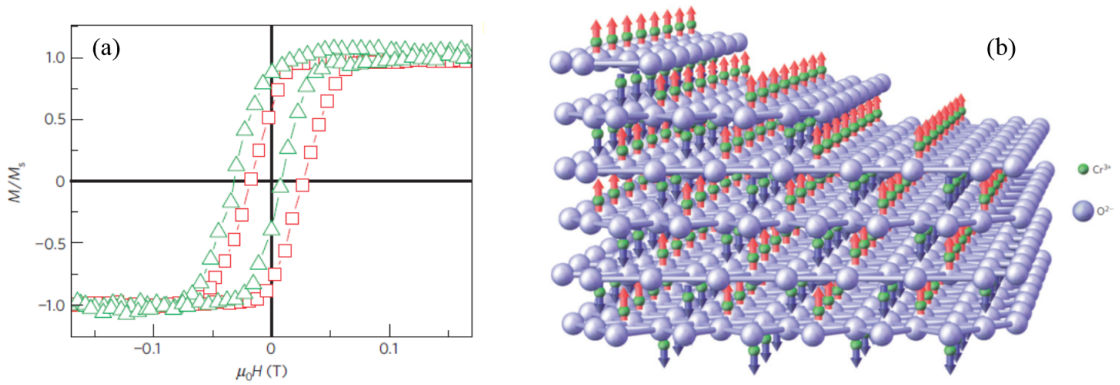

Figure 1.1: Magnetoelectric effect in antiferromagnetic Cr_2O_3. (a) Isothermal switch of exchange bias by using a combination of magnetic and electric field E·H (postive for green, negative for red). (b) Magnetic structure of antiferromagnetic Cr_2O_3. Adapted from [6].

Inspired by the observations in Cr_2O_3, the search for alternative ME materials extends to a variety of different compounds. It is worth discussing the theoretical upper limit of this coupling efficiency first, which would serve as a fundamental guide in the journey of exploration. The ME response is limited by the following formula $\alpha^2 < \chi^e \cdot \chi^m$ whereas χ^e and χ^m are the electric and magnetic susceptibility [7]. The result implies that the large ME coupling is only possible in materials with large electric and magnetic susceptibility, i.e. ferroelectric and/or ferromagnetic materials.

The discovery of multiferroic materials provides the best candidates to search for materials with large ME coupling efficiency. Multiferroics, by definition, are materials that show simultaneously more than one ferroic ordering (i.e.ferroelectric, ferromagnetic, ferroelastic and ferrotoroidicity) [1, 8–10]. In the realm of ME effects, the materials with both ferroelectric and ferromagnetic orderings are particularly intriguing since the potential coupling between the dual orderings can be relatively high. Therefore the terminology multiferroic generally refers to the materials with both ferroelectric and ferromagnetic ordering, which later on also extends to anti-ferroic orderings. Although the terminology multiferroic is very similar to the magnetoelectrics, they are actually different in the physical meaning. The scope of different classifications based on the magnetic and electric properties is summarized in figure 1.2. It can be seen clearly that magnetoelectrics are not identical to the mulitiferroics.

ME materials don't necessarily possess more than one ferroic ordering, such as Cr_2O_3. On the other hand, multiferroic materials don't always exhibit ME coupling, albeit with dual ferroic orderings.

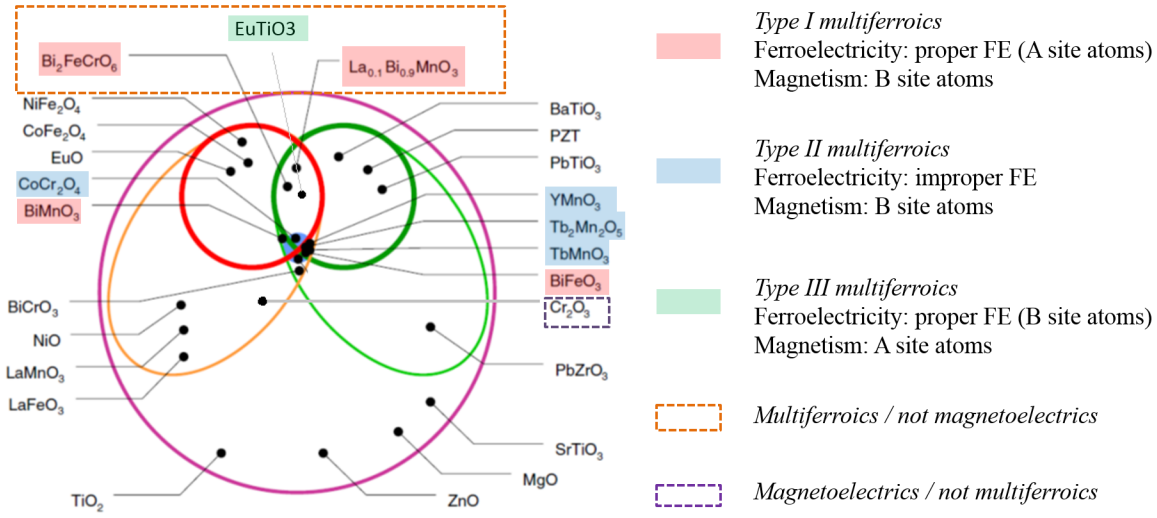

Figure 1.2: Classification of materials based on magnetic and electric response. The green and yellow ellipses correspond to the electric and magnetic polarizable materials. The green and red circles within the ellipses correspond to ferroelectric and ferro/ferri magnetic. Multiferroics correspond to the overlap of two ellipses. Adapted from [8].

Figure 1.2 unambiguously implies that there is only a small portion of materials that are multiferroic. So what is the fundamental physics behind the scarcity of the coexistence of the ferroelectric and magnetic ordering? To answer this question, we shall firstly understand the fundamental physics to account for ferroelectricity and ferromagnetism. Ferroelectric materials have the electrically switchable spontaneous polarization. Microscopically the spontaneous polarization is related to the cation off-centering, which is only possible in dielectric insulators with broken spatial inversion symmetry. $BaTiO_3$, one of the earliest discovered ferroelectrics, serves as a good example of this conventional mechanism of ferroelectricity. The off-center distortion of Ti^{4+} is the origin of ferroelectricity, which is microscopically ascribe to the hybridization of d^0 orbital and oxygen $2p$ orbital. On the other hand, ferromagnetism refers to the spontaneous long-range ordering of magnetic moments, which are switchable through magnetic field. The first prerequisite condition is that the atoms should have local moments, or in other words, the uncompensated electrons in d or f orbital in most cases. Different types of ferromagnetic interactions have been discovered. One group of well-known ferromagnetic materials is transition metals

Ni, Co, Fe and their alloys, in which the driving force is the imbalance of the density of states between the spin-up and spin-down states below the Fermi surface (s-d model) [11]. Another type of famous ferromagnet is the colossal magnetoresistance material, i.e.doped manganite, which is dominated by the double-exchange interaction first proposed by Zener [12]. The details of the double-exchange interaction will be covered later. Nevertheless, all the different mechanisms require itinerant electrons as the medium, which stand exactly opposite to the insulating nature of ferroelectricity.

The reasons for the scarcity of multiferroic materials have been elucidated explicitly by Spaldin in several review papers [13, 14]. In summary, the transition metal d electrons, which are essential for magnetism, reduce the tendency of off-center ferroelectric distortion, which is the conventional mechanism for ferroelectricity in materials such as $BaTiO_3$. The contra-indication can be circumvented by an alternative mechanism for ferroelectricity or magnetism. In the first approach, based on the different mechanisms of the inversion symmetry breaking, multiferroics can be roughly divided into two groups: the proper ferroelectrics by making use of the stereochemical activity of the lone pair on the A-site cation (Bi, Pb) and the improper ferroelectrics in which spontaneous polarization arises from other phase transitions as a secondary effect [15,16]. The different types of ferroelectricity in the multiferroic materials are summarized in table 1.1. In the second approach, magnetic cations with partially full orbital (usually f electrons) are used to substitute the non-magnetic A site cations.

1.1.2 Single-component multiferroics

In the first type of single-component multiferroics, ferroelectricity and magnetism originate from different sublattice of the structure. The interaction between the $6s$ electron pair of A-site atoms (such as Bi, Pb) with oxygen dominates the ferroelectric distortion. Meanwhile the magnetism arises from the B site atoms, which is usually $3d$ transition metal cations. One thing we should keep in mind is that ferroelectricity requires the insulating nature. Therefore the d^3 and d^5 cations are likely to be the best candidates (the reason will be discussed in the next session). The two most well-studied materials in this group are $BiMnO_3$ and $BiFeO_3$. The ferroelectric Curie temperature is relatively high in these two materials, $\sim$450K for $BiMnO_3$ [17, 18] and $\sim$1103K for $BiFeO_3$ [19]. $BiMnO_3$ is an interesting material that shows ferromagnetism with a significant magnetization, which is ascribed to a particular orbital ordering pattern [20, 21]. The major weak point of $BiMnO_3$ is the low Curie temperature of the ferromagnetic ordering ($\sim$100K) and the weak coupling between the two orders. Nevertheless, some interesting results suggest the possibilities to use this material in real devices [22]. On the other hand, $BiFeO_3$ is a G-type antiferromagnet with T_N around $\sim$643K [19]. What makes it promising is the strong coupling between the antiferromagnetic ordering and ferroelectric distortion [23, 24]. Furthermore, the net canting moment due to Dzyaloshinskii-Moriya interaction [25] and the uncom-

pensated spins at the domain walls provide additional functionality to couple with other ferromagnetic materials [26].

A good review of the second type of multiferroics can be found in reference [27,28]. The type II multiferroics is improper ferroelectric, which means the polarization is only a part of a more complex lattice distortion or it appears as an accidental by-product of some other orderings. Generally speaking, type II multiferroics can be divided into three subgroups based on the driving force. The first kind is structure driven improper ferroelectricity, for example the hexagonal $YMnO_3$. The electric dipole moment is induced by a nonlinear coupling to an non-polar lattice distortions, such as the buckling of R-O planes and tilt of manganese-oxygen bipyramids [29–31]. However since the polarization is locked by structure transition, the magnetoelectric coupling is not strong. In the second subgroup, the improper ferroelectricity originates from the non-center fashion of charge ordering. Therefore it is also called electronic ferroelectrics. Charge ordering is a phenomenon that electrons localize in a certain pattern in many narrow-band metals with strong electronic correlation. Electron dipoles can be induced when the center symmetry is broken during the process, such as charge-ordered manganite or $LuFe_2O_4$ [32–34]. The third subgroup is the frustrated magnetic material, in which the ferroelectricity is directly related to the frustrated spin structure. The orthorhombic manganite serves as a good example. The parent phase, $LaMnO_3$ is an A-type antiferromagnet (neighbouring spins couple parallel (FM) in the a-b planes and anti-parallel (AF) along the c axis. Consistently, spins in each a-b plane order ferromagnetically and the magnetization direction alternates along the c axis. If La is replaced by smaller ions such as Tb or Dy, the structure distortion induces next-nearest-neighbour AF exchange coupling in the a-b planes comparable to the nearest-neighbour FM exchange coupling, which then leads to a frustrated state. Actually, the spin spiral structure develops at low temperature and leads to ferroelectricity [35]. Although the electric dipole moment is very small in this subgroup, the magnetoelectric coupling is still in a reasonable range since the origin of ferroelectricity is deeply rooted in the magnetic structure.

Another type of multiferroic, which we can call it type III, solves the dilemma of ferroelectricity and magnetism coexistence by an alternative approach. The mechanism for ferroelectricity is the conventional B site cation off-center. However, cations with partially filled f orbital are synthesized in A sites, providing the magnetism. One good example is $EuTiO_3$, which in bulk is an antiferromagnetic and dielectric material. Theoretical calculations suggest that it would develop ferromagnetic and ferroelectric orderings by strain [36], which has been subsequently demonstrated experimentally [37]. However the major limitation is the low magnetic ordering temperature due to the nature of f orbital and chemical environment of A site cations.

So far we have reviewed briefly the developments of multiferroic materials and the different classifications of multiferroic materials that have been studied. One interesting phenomenon is that more than eighty percent of the multiferroic materials are in the perovskite structure. Therefore the next section will cover the brief review of

	Mechanism of Inversion Symmetry Breaking	Model Materials
Proper	Covalent bonding between $3d^0$ transition metal (Ti) and oxygen	$BaTiO_3$, Strained $EuTiO_3$
	Polarization of $6s^2$ lone pair of Bi or Pb	$BiMnO_3$, $BiFeO_3$, $Pb(Fe_{2/3}W_{1/3})O_3$
Improper	Structural transition "Geometric ferroelectrics"	K_2SeO_4, Cs_2CdI_4 hexagonal $RMnO_3$
	Charge ordering "Electronic ferroelectrics"	$LuFe_2O_4$
	Magnetic ordering "Magnetic ferroelectrics"	Orthorhombic $RMnO_3$, RMn_2O_5, $CoCr_2O_4$

Table 1.1: Classification of ferrolectrics. In proper ferroelectrics, the first type can be multiferroic (Type III) by using magnetic A site cations; the second type could be type I multiferroic with magnetic B site cations. The improper ferroelectrics with magnetic B site cations are type II multiferroics. Table adapted from [27]

.

the fundamental physics of perovskite in terms of crystallography, electronic structure and magnetic coupling in order to better understand the the subsequent discussions.

1.2 Complex perovskite oxides

The perovskite oxides and structure-related materials (like Ruddlesden-Popper type layered perovskites) have demonstrated a broad range of intriguing functionalities, such as ferromagnetism, colossal magnetoresistance (CMR), ferroelectricity, piezoelectricity, high T_c superconductivity, 2-D electron gas and also the multiferroics. Therefore they have been the playground for material scientists and condense matter physicists for many decades. A great deal of works have been devoted to unveil the nature of fundamental physics in the perovskite oxides system, which in turn serve as the guidelines to better design new functionalities. The session will present a brief summary of the structure, charge, spin and orbital degrees of freedom in perovksite oxides, the key knowledge to understand the varieties of novel functionalities.

1.2.1 Crystallographic structure of perovskite oxides

The typical structure of a perovskite oxide is shown in figure 1.3(a) with the general formula of ABO_3. In this structure, the A-site atom, on the corners of the lattice, is usually an alkaline earth or rare earth element. B site atom, on the center of the lattice, could be 3d, 4d or 5d transition metal cations. The B site atom, as shown in the figure, is surrounded by six nearest oxygen atoms, which form the octahedral. From the geometry point of view, there is another perspective to understand the

structure. As shown in figure 1.3(b), transition metal oxides of the ABO_3 perovskite class are consisted of two parts: the corner-sharing BO_6 octahedral with central B-site transition metal cation and the A-site cation. The physical reason behind the second description is that the BO_6 octahedral is usually considered as the functional unit of the perovskites due to the active role of B-O bond. Variations in the size (B-O bond length), shape (number of unequal B-O bond) and connectivity pattern (the rotation of octahedral with respect to each other that determines the B-O bond angle) provide access to a wide spectrum of different functionalities (figure 1.3(c),(d)). On the other hands, A-site atoms are typically regarded as the supporting inert backbones with a few exceptions such as the $6s$ electron pair of A-site Bi and Pb or f orbital of some A-site rare-earth atoms. But generally the majority of the properties is controlled by B-site atoms and A-site atoms mainly serve as the structural framework.

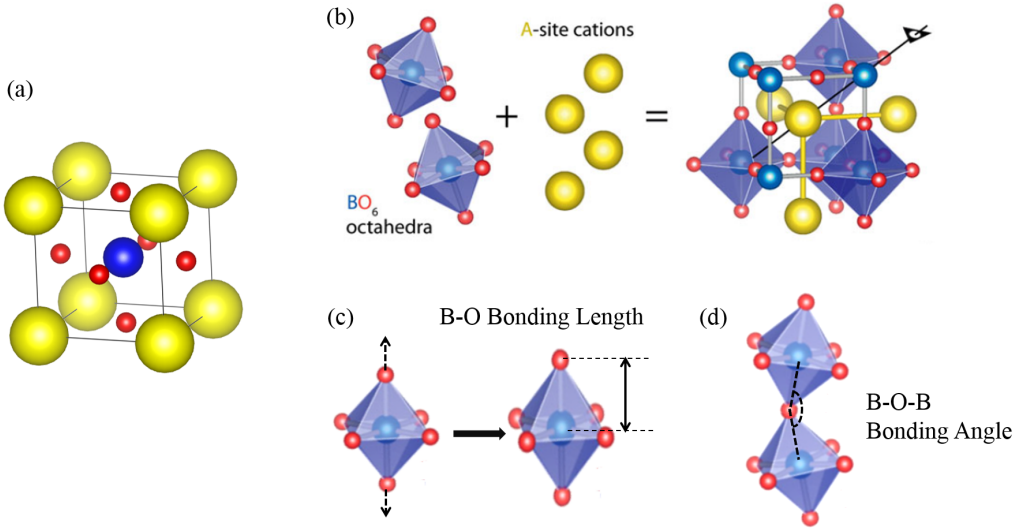

Figure 1.3: Crystallographic structure of perovskite oxides. (a) The schematic of one unit cell of cubic ABO_3 (yellow spheres are the A site atoms, blue are the B site and red are oxygen atoms). (b) Structure of pervoskite oxides can be considered as the A sites atom plus the oxygen octahedral that contains the B site atom. (c) Two main lattice distortions of the octahedral, bond elongation and octahedral rotation. Adapted from [38].

Most of the perovskite oxides are not perfect cubic. Depending on the octahedral shape and rotation pattern in three directions, there are three other structures with lower symmetry compared with cubic: tetragonal (P4mm), rhombohedral ($R\bar{3}c$) and orthorhombic (Pbnm). Studies of bulk system have established the guidelines to understand perovskite structure based on ionic radii of the constituents and inter-atomic bond length (e.g., tolerance factor) [39]. The tolerance factor is defined as

following:

$$\tau = \frac{R_A + R_O}{\sqrt{2}(R_B + R_O)} \tag{1.1}$$

In this equation, R_A, R_B and R_O are the ionic radii of A-site cation, B-site cation and oxygen anion respectively.

Before discussing the tolerance factor, we should first define the notation of octahedral rotation pattern. Here we use the Glazer notation by the manner in which adjacent octahedra rotates along a particular Cartesian direction: $a^{-(+)}$ indicates out-of-phase (in-phase) rotation, while a^0 denotes no rotation, about the Cartesian axis a [40]. When the tolerance factor is $\sim$1, the pervoskite is in the cubic structure (typical example is $SrTiO_3$). As the size of A-site atoms increases, the octahedral is elongated to increase the A-site coordinate volume, which leads to the tetragonal structure. Two type of distortions are permitted in this structure, i.e. the polar distortive B-site cation displacement ($BaTiO_3$, $PbTiO_3$) and the anti-ferro-distortive rotation ($SrTiO_3$ at low temperature [41]). Due to the low symmetry, rotation is only allowed about the c axis (figure 1.4(b)). On the other hand, as the size of A-site atoms decreases, the structure transforms into rhombohedral and orthorhombic in sequence ((figure 1.4(b))). In rhombohedral structure, the octahedral rotation pattern is $a^-a^-a^-$, which effectively rotates about [111] axis. Typical examples are $BiFeO_3$ or $LaNiO_3$. As for the $6s$ electron pair, the rhombohedral structure favors polar distortion. In orthorhombic structure, the octahedral rotation pattern is $a^-b^-c^+$. Typical example is $PbZrO_3$ and the rotation pattern favors the anti-ferrodistotive instability [42].

The close connection between the structure and properties lies in the key role of B-O-B bond. The change of bond length, associated with the modulation of octahedral shape and size, can lead to highly versatile changes of the properties, such as the orbital ordering and collective Jahn-teller distortion in manganite [43]. In addition, the change of octahedral connectivity, including the pattern and magnitude of rotation, determines the B-O-B bond angle. In perovskites one of the fundamental energy terms is the kinetic energy, usually expressed as the effective hopping interaction $t_{ij} \propto cos(\theta_{ij}/2)$ [44]. Therefore the bond angle could determine the bandwidth, manifesting itself as the metal-insulating transition demonstrated in rare-earth nickelate system by decreasing the size of A-site atoms [45, 46] and also in manganite system [44].

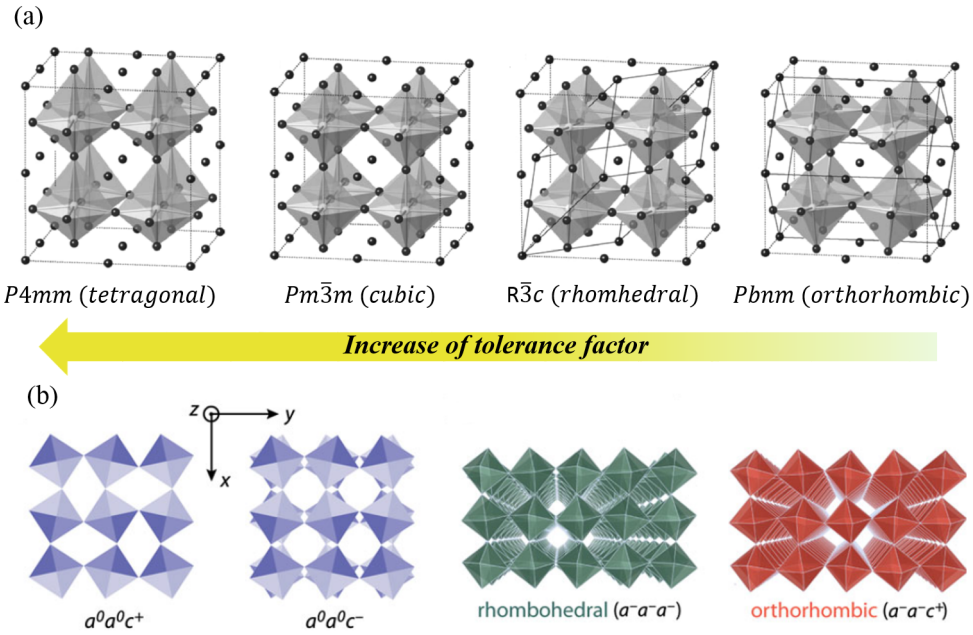

Figure 1.4: Four typical perovskite structures and the octahedral rotation patterns. (a) Unit cell of tetragonal, cubic, rhombohedral and orthorhombic ABO_3 from left to right. (b) Octahedral rotation pattern of the four symmetry group. (the notation a/c refers to the rotation axis and +, 0, - refer to in-phase rotation, no rotation and out-of-phase rotation). The structure and octahedral pattern are determined by the tolerance factor. Adapted from [38, 47].

At the end of this section, we briefly discuss the strain engineering effect. For decades, strain engineering, the method to control the lattice of films by choosing respective substrates, have been demonstrated to be extremely successful to tailor the dielectric, ferroelectric and magnetic properties. Although it is well-studied that the lattice tetragonality (c/a ratio) is controlled by the substrate strain, the response of octahedral is poorly understood mainly due to the lack of direct experimental methods. However, as stated above, it is the octahedral shape/size and connectivity that mainly determine the properties. A detailed review can be found in the reference [38] based on first principal calculation and recent synchrotron X-ray diffraction results. Generally speaking, compressive biaxial strain enhances the magnitude of the octahedral rotations about the [001] direction, while tensile strain favors the [110] direction in rhombohedral structure [48]. For orthorhombic structure, it is more complicated depends on the orientation of c axis ($a^-a^-c^+$) with respect to the substrate orientation (in-plane or out-of-plane).

1.2.2 Electronic structure of perovskite oxides

In the perovskite ABO_3 structure, the B site is always filled by the transition metal cation with partially filled d electrons. Despite of the variety of cations from d^0 to d^{10}, they all share the similar electronic structure. This session will cover the basic electronic structure of the perovskite materials, mainly focusing on the d orbital of a single cation in the oxygen octahedral, which accounts for the versatile properties.

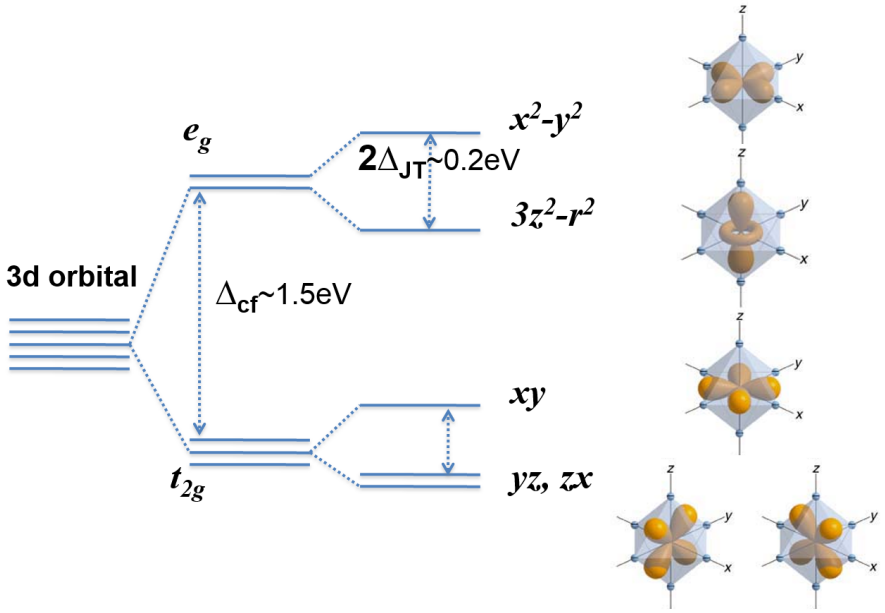

Figure 1.5: The energy splitting of $3d$ orbital in perovskites. Crystal field lifts the degeneracy of $3d$ orbital into high energy e_g orbital and lower energy t_{2g}. The energy gap is noted as $\triangle_{cf}$ in the order of 1eV. The degeneracy can be further lifted by lattice distortion like Jahn-teller effect as shown in the figure (the energy gap is in the order of 0.1eV). The right panel shows the spacial distribution of the five d orbitals.

There are two important energy terms that determine the d orbital energy level of a single cation in the oxygen octahedral. The first one is the spin-orbit coupling term (ξ_{so}), which describes the interaction of the electron's spin with its motion (orbital). This term originates from the relativistic effect in quantum physics and is proportional to Z^4 (Z is the atomic number). For $3d$ transition metal, the spin-orbit coupling term is very weak and usually neglected. Therefore the orbital energy level of the $3d$ transition metal cation is mainly determined by the second term, crystal field ($\triangle_{cf}$). Crystal field is the interaction between a transition metal cation and ligands that arises from the attraction between the positively charged metal cation and negative charged ligand. In perovskites, the B-site cation is always surrounded by six oxygen anions regardless of the different lattice distortion. Therefore the five-fold

degeneracy of the d orbital is lifted, leading to two degenerate high energy orbitals (e_g) and three degenerate low energy orbitals (t_{2g}). Figures 1.5 shows the energy gap formed by the crystal field is ~1eV. Furthermore the distortion of oxygen octahedral, which is discussed in last session, can further lift the degeneracy of e_g and t_{2g} orbital and open the energy gap in the order of 0.1eV (see figure 1.5).

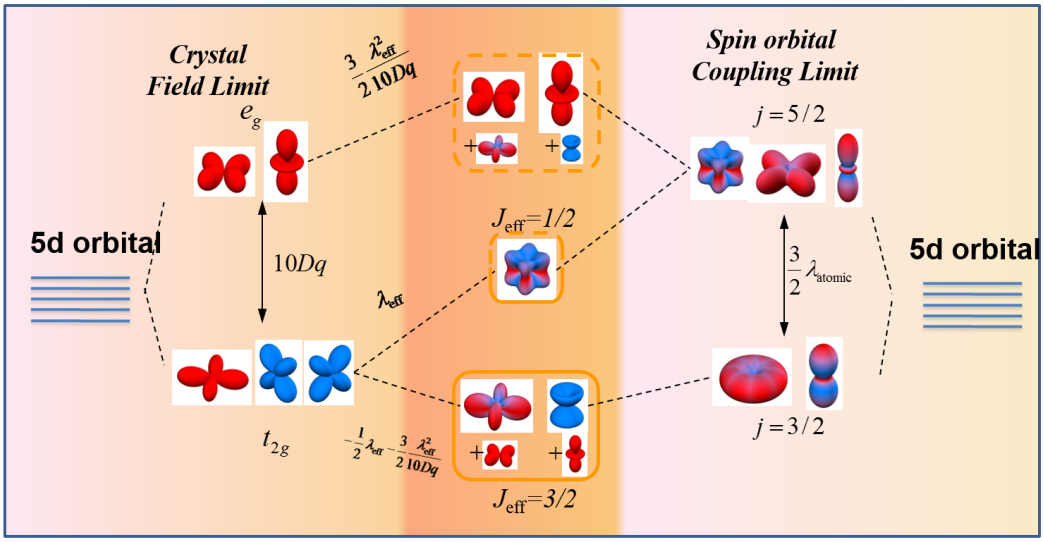

Figure 1.6: The energy splitting of $5d$ orbital in Iridate. The left panel shows the degeneracy of $5d$ orbital lifted by the crystal field in the strong crystal field limit ($\triangle_{cf} \gg \xi_{so}$). The right panel shows the degeneracy of $5d$ orbital lifted by the spin-orbit coupling in the strong spin-orbit coupling limit ($\triangle_{cf} \ll \xi_{so}$). For iridates (Ir), the two energy terms are similar in magnitude, which result in the orbital degeneracy shown in the middle panel. Courtesy of Dr.Jian Liu.

However for $5d$ transition metal cations, the energy term associated with the spin-orbital coupling is comparable to the crystal field, which manifests itself as the different degeneracy of d orbitals. One of the model systems that attracts lots of attentions recently is the iridates (such as Sr_2IrO_4). The spin-orbit coupling energy (ξ_{so}) is roughly 0.4eV, similar in the order of magnitude compared to the crystal field. Therefore the two energy terms play an equally important role to determine the $5d$ orbital energy levels [49], as illustrated in figure 1.6. The left panel of figure 1.6 reveals the energy splitting in the strong crystal field limit ($\triangle_{cf} \gg \xi_{so}$), which is exactly what happens in figure 1.5. On the other hand, the right panel shows the $5d$ orbital splitting in the strong spin-orbit coupling limit ($\triangle_{cf} \ll \xi_{so}$). When the two energy terms act simultaneously, the energy levels of Ir $5d$ orbital is shown in the middle panel, which is dramatically different from the $3d$ counterparts.

So far we discussed the energy degeneracy of d orbital of the single cation in

perovskite structure. The next step is to bridge these cations together and form the band structure of the crystal. A detailed review on this topic is beyond the scope of the dissertation and can be found in reference [50]. Generally speaking there are three important terms here, the filling number n, the kinetic energy (hopping integer) t and the coulomb repulsion U. The first term, filling number, describes the number of d electrons in the cation, which thus determines the valence state and the fermi level. The second term has been discussed in last session, which is closely related to the B-O-B bond. Physically it is proportional to the bandwidth W. The third term describes the electron-electron interaction in the same orbital. Basically the coulomb repulsion U favors the localized electrons (Mott insulator) and the kinetic energy t favors the itinerant electrons. Therefore the dedicate competition between the two with different number of d electrons leads to a variety of electronic structures in perovskites, such as the band insulator ($SrTiO_3$, $LaFeO_3$), mott insulator ($LaMnO_3$) and metal ($LaNiO_3$).

1.2.3 Magnetic interactions in perovskite oxides

This section covers the basic concept to understand the magnetism and magnetic orderings in perovskites. The question can be divided into two steps. First, the magnetic moment of a single cation will be discussed, which is the basic unit of the magnetic ordering (analogue to one atom in the crystal). Then the different types of magnetic interaction between single cations will be presented, which determine the long-range orderings.

In last section we consider how the d orbital splits due to the crystal field and spin-orbit coupling. However we haven't taken into account the spin degree of freedom. The degeneracy of spin-up and spin-down state can be lifted by the Hund's rule, which is ascribed to the repulsion of electrons in the same orbital. The competition of Hund's coupling (J_{Hund}) and crystal field ($\triangle_{cf}$) determines the spin configurations of $3d$ transition metal cations. If Hund's coupling is the dominant term, electrons occupy the high spin state (figure 1.7(a)). This is the case for Mn^{3+} (d^4), Fe^{3+} (d^5). However crystal field favors the low spin state (figure 1.7(b)), which is the case for the later half of the $3d$ transition metal cations such as Ni^{3+} (d^7). An interesting transition happens for Co^{3+} (d^6), which lies at the boundary between high-low spin state. As a matter of fact, $LaCoO_3$ shows interesting spin transition phenomena. It is low-spin at low temperature and a mixture of high and intermediate spin at high temperature [51, 52]. Furthermore, the magnetic ground state is tunable through epitaxial strain due to the modulation of crystal field [53].

So far we have introduced the basic spin configuration of the single cations. The next step is to explain how the magnetic moment of each cation couples with each other. The interaction is dramatically different from their metal counterparts like ferromagnetic Fe, Co or Ni if we take into account of the chemical environment of each cation. The nearest neighbor of each transition metal cation is the non-magnetic

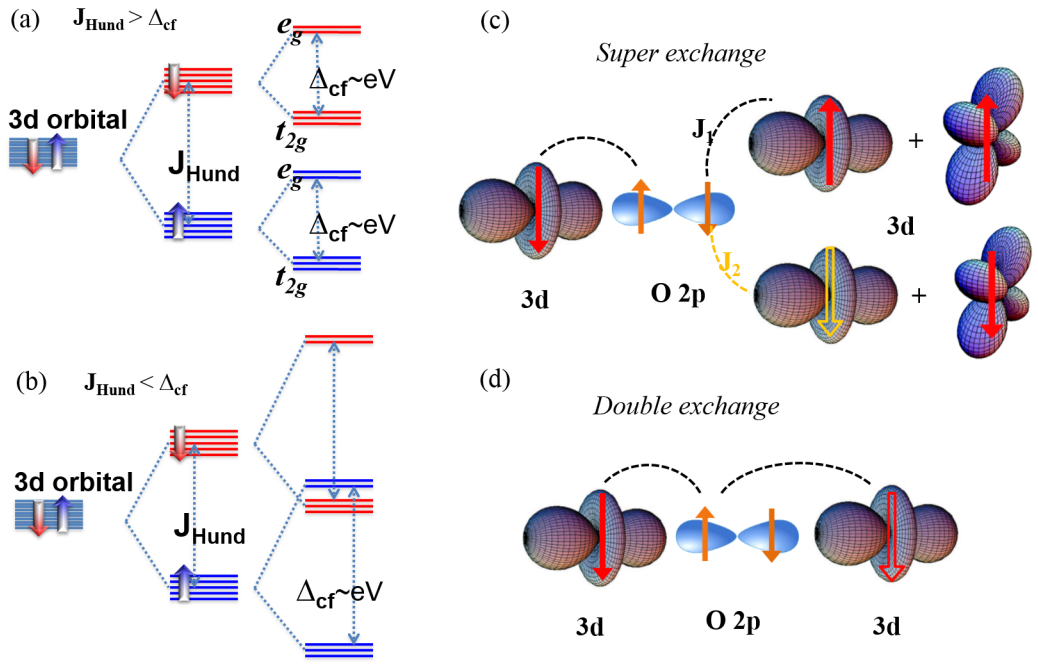

Figure 1.7: Spin configurations of single cations in perovksites and two types of magnetic coupling. Hund's energy (J_{Hund}) lifts the degeneracy of spin-up and spin-down states. Depends on the relative magnitude of Hund's energy (J_{Hund}) and crystal field ($\triangle_{cf}$), two types of spin configuration exists: (a) the high spin configuration ($\triangle_{cf} \gg J_{Hund}$) and (b) the low spin configuration ($\triangle_{cf} \ll J_{Hund}$). The right panel is the schematic of two types of magnetic interaction between cations in perovksite: (c) super-exchange and (d) double-exchange, the sign of super-exchange depends on the electron occupation of d orbital and double-exchange favors ferromagnetic coupling.

oxygen anion. Therefore the long-range magnetic ordering observed in many transition metal oxides perovskites clearly reveals the fact that the magnetic coupling is bridged by the oxygen anion between two nearest cations. The coupling mechanism, which was originally proposed by Kramer in 1930s, is known as superexchange right now. The ideal was later formulated by Anderson in 1950 [54] and followed by a series of models proposed by Goodenough [55, 56]. In 1958, Kanamori summarized the different semi-empirical rules and demonstrated the importance of symmetry consideration [57], which became the foundation of superexchange coupling and known as GKA (Goodenough-Kanamori-Anderson) rules. The core of superexchange theory is the visual electron hopping between the cation d electron and anion p electron. Although the sign of coupling depends on the geometry of the two orbitals, we only consider the 180 degree B-O-B bond here, which is dominant in perovskites. Depending on the number of d electrons and the spin configuration (high or low), the sign of coupling between d electron and p electron can be negative (antiparallel, the case

in which the active orbital is half-filled or more, J_1 in figure 1.7(c)) or positive (parallel, the case in which the active orbital is less than half-filled, J_2 in figure 1.7(c)). Therefore the effective coupling between two nearest cations can be ferromagnetic or antiferromagnetic. A detailed discussion of different combinations of d^n states can be found in reference [57]. It is worth pointing out that the visual hopping in superexchange model does not really happen. In other words, the electrons remain localized and the materials are insulating. There is another coupling mechanism which was proposed by Zener [12] and referred as double exchange. The mechanism explains the magnetic coupling in the metallic manganite with mixed Mn valence states. It contains two steps as shown in figure1.7(d), one p electron hops to the nearest empty d orbital and leave a hole where the d electron of another cation can fill in. Therefore the electrons are itinerant. Based on the Hund's rule, the magnetic coupling favors the parallel configurations between the p and d spins, which leads to the ferromagnetic long-range ordering.

At the end of this session, we would like to compare the two magnetic coupling mechanisms. The big difference is whether there is actual electron hopping or not. For perovskites with fixed valence state of cations, charge transfer is prohibited due to the large energy cost and thus dominated by the superexchange. On the other hand, for perovskites with mixed valence states, charge transfer is possible due to the small energy difference of different valence states and therefore the system will be dominated by double exchange. Superexchange would favor either ferromagnetism or antiferromagnetism based on the cations and the bond geometry. On the other hand, double exchange always leads to ferromagnetic ordering.

1.3 Multiferroic heterostructures

Although the discovery of magnetoelectric coupling can date back decades ago, the revival of this field is strongly driven by real application demands. The broad interest of studying multiferroic materials roots in the central question that whether we can use electric field to deterministically control the magnetic states, which are used in data storage after the discovery of giant magnetoresistance (GMR) effects. Electric field control is faster, more localized with lower energy cost, which in principal meet the requirements for the next-generation devices. However none of the single-component multiferroic material discussed in the first section is suitable. First of all, the majority of the multiferroics exhibit at least one order parameter below the room temperature (such as the ferroelectric ordering for many type II multiferroics). Second, the coupling between two orderings might be very weak (type I $BiMnO_3$ and type III $EuTiO_3$). Actually the only room temperature multiferroic that has been widely studied is $BiFeO_3$, which also shows a strong coupling. However $BiFeO_3$ is an antiferromagnet in nature. Although Dzyaloshinskii-Moriya interaction induces a small canting moments, the net magnetization is too small to be used directly.

There is also an alternative way that researchers have perused to design better multiferroics, which is to build the heterostructures. By combing two materials with separate ordering, one can artificially create the multiferroic heterostructures. The substantial ferroelectric and ferromagnetic materials provide researchers lots of freedom to design. Then the key question is how to couple the two orderings of two different materials together. Before we discuss the different design routes, let's first take a close look at the interface of the heterostructure.

1.3.1 Emergent phenomena at perovskite oxide interfaces

Geometrically interface is a two-dimensional plane where two different materials bond together. Trivial as it sounds to be, interfaces of perovskites oxides heterostructures actually show lots of exotic phenomena that are different from either one of the components. Recent technical advances in the atomic-scale synthesis of oxide heterostructures have provided a fertile new ground for creating novel states at their interfaces and have attracted huge amount of attentions. There are several good review papers that cover the emergent phenomena, the novel physics and the unsolved challenges for heterointerfaces [58–60]. In this section, we will briefly discuss the emergent phenomena based the coupling and reconstruction of lattice, spin, orbital and charge degree of freedom at the interface.

For spin degree of freedom, novel magnetic structure can be deduced at the interface. When materials with two different magnetic ordering parameters couple at the interface, magnetic moment at the interface is affected by the coupling on both sides, which therefore might lead to a frustrated states as shown in figure 1.8. More interestingly, since the cations on both sides are generally different, superexchange interaction across the interface might favor a coupling that is different from the bulk, which additionally contributes to the possible exotic states. For example, the superlattice of $LaFeO_3$ and $LaCrO_3$ shows ferromagnetism, which otherwise is antiferromagnetic in each components [61].

For charge degree of freedom, a famous interface phenomenon is the two dimensional electron gas that forms at the interface of two band insulator $SrTiO_3$ and $LaAlO_3$ with different polar discontinuity. Hwang reported this unexpected electron gas in 2004 [62] and later proposed a model based on polar catastrophe to explain the charge transfer [63] (see figure 1.8). Generally speaking, for ABO_3 perovskite, the A and B cations have following combinations in terms of valance states: $A^{4+}B^{2+}$, $A^{3+}B^{3+}$, $A^{2+}B^{4+}$, $A^{1+}B^{5+}$ and the middle two are the most common case. The charge neutrality is preserved in each one of the cases. However when two materials with different valence configuration meet, the interface might break the charge neutrality, which could be compensated either by defects or electrons. The two mechanisms were indeed observed at $SrTiO_3$ and $LaAlO_3$ interface when the termination changes.

For orbital degree of freedom, orbital reconstruction is observed at the interface. For example, when studying the interface of superconducting $(Y,Ca)Ba_2Cu_3O_7$

(YBCO) and ferromagnetic $La_{0.67}Ca_{0.33}MnO_3$, Chakhalian observed the reconstruction of Cu $d(3z^2 - r^2)$ orbital, which is otherwise filled and inactive in bulk (see lower right of figure 1.8). The reconstruction leads to a charge transfer from Cu to Mn, which then induces the ferromagnetism in YBCO and destructs the superconductivity at the interface [64]. The lattice degree of freedom has been covered briefly in last section when discussing the strain effect on lattice constant and octahedral rotation. Generally speaking, the tuning of octahedral connectivity is merely an interface effect and can be used to induce novel properties.

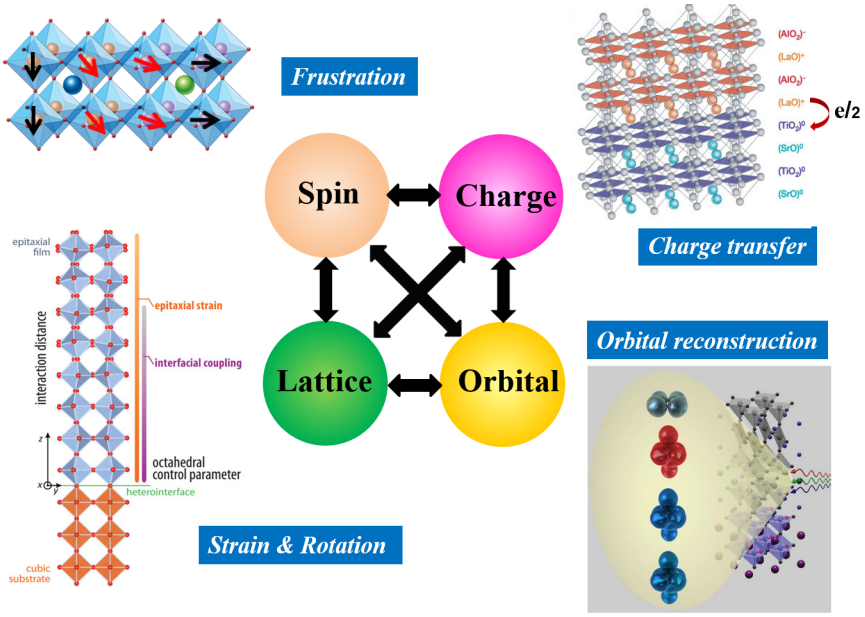

Figure 1.8: Emergent phenomena at the interface when materials with different ordering parameters couple together. For spin degree of freedom, different magnetic ordering leads to frustrated spin structure (upper left). For charge degree of freedom, charge transfer is possible for materials with a valence mismatch (upper right). For lattice degree of freedom, octahedral rotation can be manipulated (lower left). For orbital degree of freedom, orbital reconstruction is possible due to different chemical bonds. Adapted from [38, 62, 64]

So far we briefly discussed the novel states that emerge at the interface due to the differences in spin, charge, orbital and lattice degrees of freedom across the interface. However one should keep in mind that the four degrees of freedom are strongly entangled with each other, which therefore leads to various complicated but nontrivial emergent states.

1.3.2 Pathways to design artificial multiferroic heterostructures

Having discussed the emergent phenomena at complex oxides interface, we now return to the question that is raised earlier: With ferroelectric and ferromagnetic ordering coexist in the heterostructure, how can we couple the two orderings that are from different materials in a deterministic way, which therefore can be used for electric control of magnetism? The possible routes originate from the strong coupling between spin, charge, orbital and lattice degrees of freedom in complex oxides. If we can use electric field to control one of the parameters then it is possible to tune the magnetic ordering through the coupling effects.

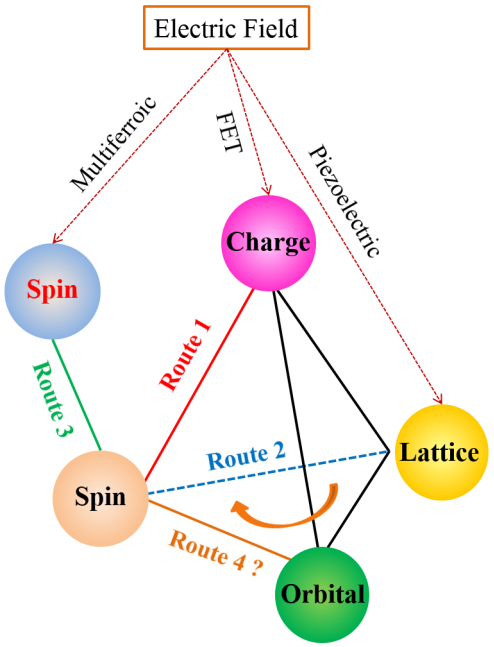

Figure 1.9: Possible routes for electric field control of magnetism based on the strong entanglement of spin, charge, orbital and lattice degree of freedom. In Route 1, electric field controls the charge degree of freedom through field-effect-transistor effect. In Route 2, electric field controls the lattice degree of freedom through piezoelectric effect. In Route 3, electric field controls the antiferromagnetic magnetic ordering of multiferroic, which is then coupled to the ferromagnetic ordering. All of the three routes have been intensively studied. Another possible route (route 4), which utilizes the orbital degree of freedom, remains a novel approach.

Figure 1.9 summarizes the possible pathways to control the spin degree of freedom by electric field. The first three routes have been intensively studied and will be presented in the rest of this section.

The first route utilizes the charge degree of freedom. Charge carrier can be modulated by electric field, which is the basic principal of field-effect-transistor (FET) in semiconductor devices. Furthermore the effect would be nonvolatile by replacing the dielectric layer of common FET device with ferroelectric materials. A good review of the ferroelectric oxides and thin film devices can be found in reference [65]. The key point is that the tunable range of carrier density is in the order of 10^{20} cm^{-3} by considering the typical polarization of ferroelectrics, which rules out most ferromagnetic metal and alloy with a much higher carrier density. Besides, the ferromagnetism should strongly depend on carrier density in the ferromagnetic candidates. The CMR manganite system turns out to be a very good candidate under the criteria, which is pursed both theoretically and experimentally [66,67]. Figure 1.10 shows the modulation of magnetization of the CMR $La_{0.8}Sr_{0.2}MnO_3$ in different ferroelectric polarization states. Based on the polarization direction, the manganite at interface will be electron doped (accumulation) or hole-doped (depletion), which then leads to different magnitude of magnetization. The mechanism was further proved by using near edge x-ray absorption spectroscopy (NEXAS) to probe the valence state of Mn cations in the LSMO layer as a function of external electric field, which mimics the ferroelectric hysteresis loop [67]. The important role of interface has also been investigated [68].

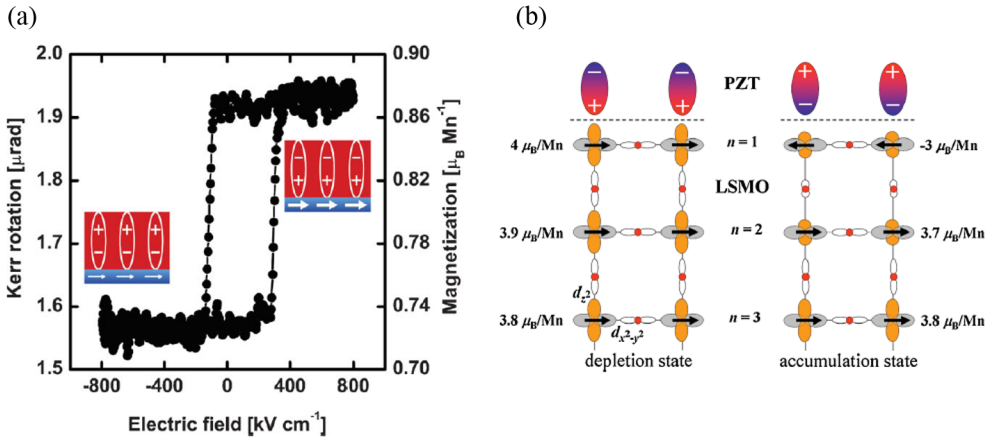

Figure 1.10: Electric field control magnetism by modulating the charge carrier density in ferroelectric/ferromagnetic heterostructure. (a) The modulation of magnetization measured by MOKE in the $PbZr_{0.2}Ti_{0.8}O_3/La_{0.8}Sr_{0.2}MnO_3$ heterostructure at 10K. (b) Schematic of the magnetization and carrier density in the bipolar polarization states. Adapted from [67]

The geometry of FET and the mechanism to tune the carriers are quite promising since this route is highly stable and nonvolatile. However there are a few weak points. The main intrinsic weakness is that FET effect and charge modulation can only tune

the magnitude of magnetization but not the direction, which is usually used as the information bit. Besides since it is mostly applicable to CMR manganites, the low curie temperature further prohibits the real application. Nevertheless it is worth investigating the limit of this route, i.e. how to get the maximum tunability. The answer hides in the phase diagram of manganite, which will be covered latter in the dissertation.

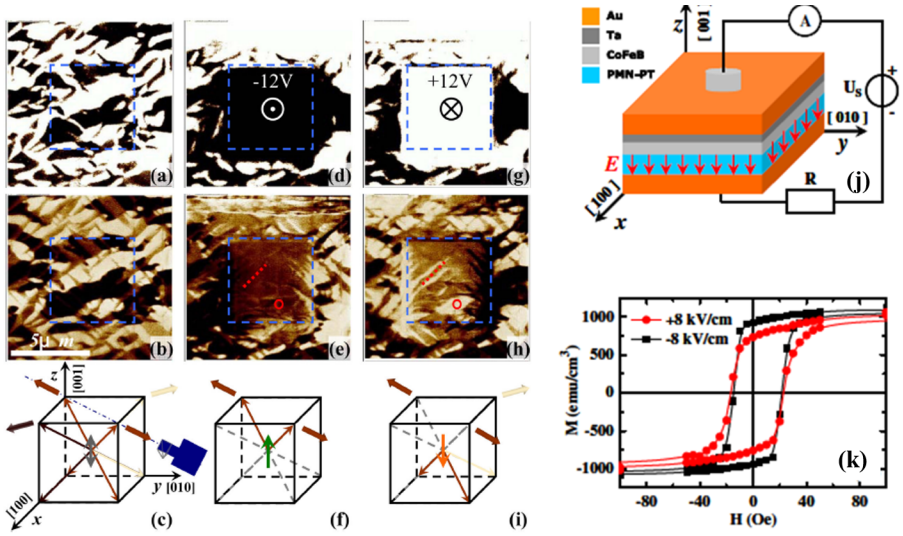

Figure 1.11: Electric-field control of nonvolatile magnetization in ferroelectric/ferromagnetic heterostructure. (a)-(f) shows the piezoelectric force microscopy (PFM) of $Pb(Mg_{1/3}Nb_{2/3})_{0.7}Ti_{0.3}O_3$: (a),(c),(e) shows the out-of-plane image of as grown, positive and negative switched states; (b),(d),(f) shows the respective in-plane images. (j) shows the schematic of the $Pb(Mg_{1/3}Nb_{2/3})_{0.7}Ti_{0.3}O_3/Co_{40}Fe_{40}B_{20}$ heterostructure and (k) shows the nonvolatile change of anisotropy by electric field. Adapted from [69]

The second route resorts to the lattice degree of freedom. In principal, the magnetization and magnetic anisotropy strongly depends on the lattice parameters of ferromagnetic crystal. And the lattice can be controlled through piezoelectric effects. Therefore large magnetoelectric coupling could be expected from piezoelectric/ferromagnetic heterostructures. Lots of research have been devoted in this direction in the early age and a good review is covered in reference [70]. The main weakness of this approach is that piezoelectric effect is volatile. Therefore it is useful as sensors instead of memories. However ferroelectric materials are also ferroelastic, which makes it possible to induce non-volatile modulation. Figure 1.11 shows a good example. Zhang et al. studied the $Pb(Mg_{1/3}Nb_{2/3})_{0.7}Ti_{0.3}O_3/Co_{40}Fe_{40}B_{20}$ heterostructure and observed a nonvolatile change of magnetic anisotropy as shown in figure 1.11(k). Upon a careful inspection of ferroelectric domains at different polarization states by

piezoelectric force microscopy (PFM), they found a non-symmetric domain change when the polarization is switched, which could be the reason of the nonvolatile effect.

The strain modulation mechanism is also very stable. Moreover, it can be applied to many ferromagnetic materials with reasonable magnetostriction efficiency. Thus there are many room-temperature candidates. The strain effect can be transferred to thin film beyond the interface region, which provides additional flexibility. However the main drawback has been discussed above. Although ferroelectric materials are possible to induce nonvolatile modulation effect, which have also been shown, the mechanism strongly depends on the local ferroelectric domain switch, which hasn't been fully understood in many systems. Therefore it still remains an open question to find out the design rule.

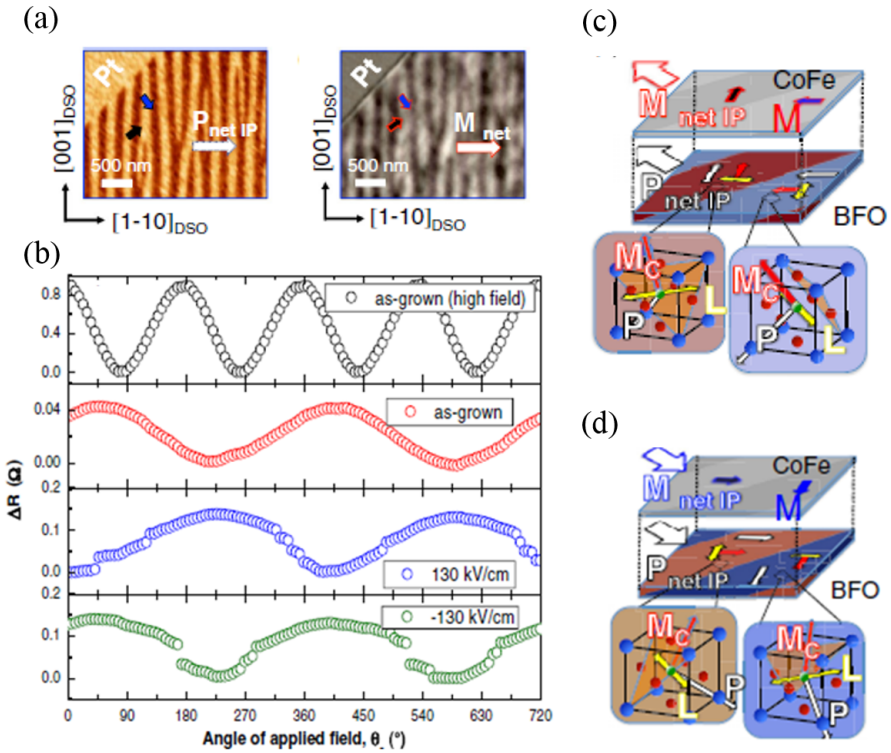

Figure 1.12: Electric-field control of magnetism by using the exchange bias coupling. (a) the PFM image (left) $BiFeO_3$ and PEEM image of of $Co_{0.9}Fe_{0.1}$, which shows a collinear coupling of net polarization and net magnetization. (b) the anisotropic magnetoresistance of as-grown, positive polarized and negative polarized states, which demonstrates the deterministic switch of magnetization. (c), (d) the schematic of polarization and magnetization in two states. Adapted from [71]

The third route directly controls the spin degree of freedom, which is usually the magnetic ordering of multiferroic materials. As discussed before, some single-

component multiferroics show a reasonable coupling between the ferroelectricity and magnetic ordering, such as the room-temperature $BiFeO_3$. However the antiferromagnetic nature of $BiFeO_3$ prohibits the direct application in current device geometry. One pathway is to couple a ferromagnet to the antiferromagnetic ordering of multiferroic materials, which leads to the unidirectional anisotropy (exchange bias coupling) in ferromagnetic layer [72]. The unidirectional anisotropy manifests itself as the shift of magnetization hysteresis loop, which actually determines the orientation of magnetization in the ferromagnetic layer. The physical origin is the coupling between the uncompensated spins in antiferromagnetic materials with high anisotropy energy and the ferromagnetic spins. Therefore the key ideal is to use electric field to control the orientation of antiferromagnetic axis, the magnitude of uncompensated spins or the coupling energy in order to deterministically control the ferromagnetic magnetization. The ideal has been pursued in different multiferroic systems and two successful demonstrations have been shown in Cr_2O_3 [6] and $YMnO_3$ [73]. However in both cases a small magnetic field is required to break the time inversion symmetry.

$BiFeO_3$ turns out to be another good model system. Early studies revealed the close correlation between the ferroelectric domains and the antiferromagnetic domains in $BiFeO_3$, which exhibit simultaneous change upon electric field switching [23]. Then the heterostructure $Co_{0.9}Fe_{0.1}/BiFeO_3$ was studied, which showed a local magnetization reversal by electric field [74]. However the complicated domain structures of $BiFeO_3$ on $SrTiO_3$ averaged the effect and prevented the application in larger length scale. Due to the advances in domain engineering of $BiFeO_3$ [75], Heron et al. studied the heterostructure $Co_{0.9}Fe_{0.1}/BiFeO_3$ on $DyScO_3$, which showed the long-range two variants domain patterns and demonstrated the electric field control of magnetism in large scale [71]. The work is followed by another study to replace the in-plane electric field by the out-of-plane electric field, which is applicable to current device geometry [76]. Figure 1.12 (a) shows the ferroelectric 109 domains of $BiFeO_3$ and the magnetic domains of $Co_{0.9}Fe_{0.1}$ revealed by Photoemission electron microscopy (PEEM), which clearly shows the collinear correlation of two orderings. Figure 1.12 (b) shows the anisotropic magnetoresistance (AMR) of $Co_{0.9}Fe_{0.1}$ at different ferroelectric polarization states and the phase is related to magnetization direction. The 180 phase change proves the deterministic control of magnetization by electric field. The coupling mechanism is shown schematically in figure 1.12 (c) and (d). The major problem in this metal-oxides heterostructure is the fatigue issue. The exchange coupling fades during the ferroelectric switch cycles, which is likely due to the metal-oxides interface barrier and redistribution of oxygen vacancies.

Actually in some heterostructures there more than one active coupling route, such as the $BiFeO_3/La_{0.7}Sr_{0.3}MnO_3$ heterostructure. $La_{0.7}Sr_{0.3}MnO_3$ is a ferromagnet and therefore the route 3 definitely plays a role. On the other hand $La_{0.7}Sr_{0.3}MnO_3$ is also a metallic material with low carrier density and therefore route 2 cannot be excluded. This heterostructure will be discussed in details in later chapter.

At the end of the section, let's look back at figure 1.9. The route to use the orbital

degree of freedom hasn't been fully explored yet and remains an open possibility, which we can call it route 4. A great number of works have demonstrated the close relationship between the lattice and orbital, which paves the foundation of this route. Then the key question is to find the close connection between the orbital degree of freedom and the spin degree of freedom. This topic will also be presented in later chapters.

1.4 Organization of the Dissertation

The dissertation is organized in the following way. Chapter 1 presents a brief introduction of multiferroic materials and fundamental physics of complex oxides, which is then followed by the discussion of different routes to achieve the electric control of magnetism in heterostructure. Chapter 2 covers the introduction of the techniques used in this dissertation. Chapter 3 presents the effects of interface engineering of $BiFeO_3/La_{0.7}Sr_{0.3}MnO_3$ heterostructure on magnetoelectric coupling. Chapter 4 shows the magnetoelectric coupling effect of $BiFeO_3/La_{0.5}Ca_{0.5}MnO_3$ heterostructure. The doping level of $La_{0.5}Ca_{0.5}MnO_3$ is near the phase boundary between ferromagnet and antiferromagnet. Therefore it is a good system to study the limit of charge modulation effect. Chapter 5 presents the results of electric field control of orbital ordering in $Nd_{0.5}Sr_{0.5}MnO_3$. $Nd_{0.5}Sr_{0.5}MnO_3$ shows an interesting orbital ordering, which is strongly correlated to spin ordering. Therefore the results provide important information to explore the route 4 proposed in last section. Chapter 6 discusses the magnetic ordering in superlattice that contains the strong spin-orbit coupling $5d$ element. The intrinsic coupling between orbital and spin in the atomic limit provides another possible pathway to pursue route 4. Then chapter 7 serves as a summary of the dissertation and proposes new directions based on the findings presented.

Chapter 2

Introduction to the growth and characterization techniques

This chapter presents an introduction to the growth and characterization techniques used in this dissertation, which serve as the necessary tools to understand the discussion in the rest of the dissertation.

2.1 Pulsed laser deposition and RHEED

The main thin film deposition technique used in this dissertation is the Pulsed Laser Deposition (PLD). The schematic of a standard PLD system is shown in figure 2.1 (a) and the technique is conceptually simple. A focused pulsed-laser beam leads to a rapid removal of material from a solid target and to the formation of an energetic plasma plume, which then condenses onto a substrate. The mechanism contains several steps, which include ablation, plasma formation, plume propagation and nucleation and growth. Physics of each step is complex and has been extensively studied in the past [77, 78], which won't be fully reviewed here. Moreover, reflection high energy electron diffraction (RHHED) is utilized to in-situ monitor the change of surface structure of the deposited materials. The RHEED assisted PLD system (figure 2.1 (b)) is also referred as Laser MBE system.

The PLD technique is ideally suitable for growing the functional oxides for the following reasons: it provides a nearly stoichiometric composition transfer from the target to the sample if the growth conditions are optimized; it is compatible with oxidant pressures ranging from ultra-high vacuum (UHV) to atmospheric; also it is capable of ablating a wide variety of materials. The chief advantages are the relatively modest cost and, after optimization of the growth conditions, the nearly faithful composition transfer from target to substrate [80]. Furthermore, with the help of RHEED, growth can be controlled at the atomic scale, which is the prerequisite for high quality superlattices. Before we discuss the implication of RHEED, let's first review the

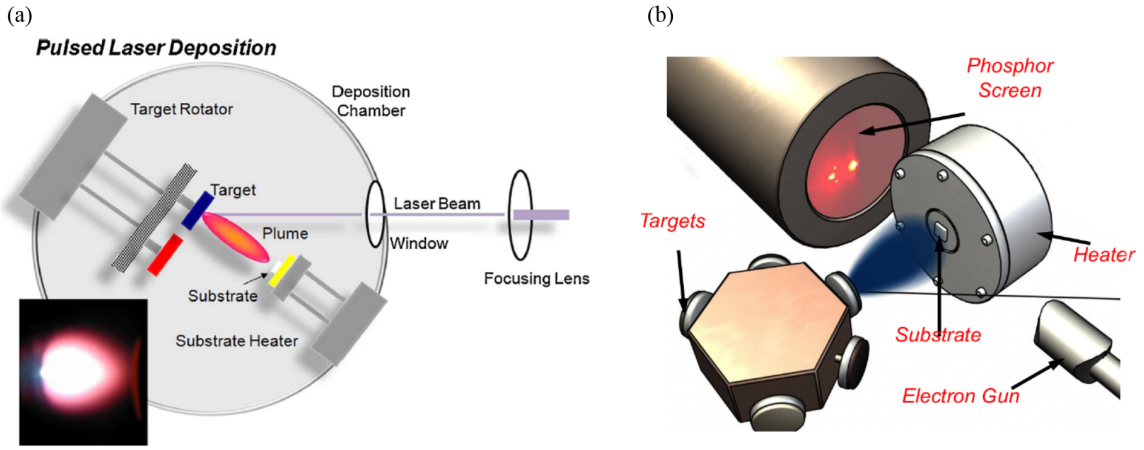

Figure 2.1: Schematic of pulsed laser MBE system assisted by the reflection high energy electron diffraction. (a) Schematic of a standard pulsed laser deposition system and the deposition process. (b) The geometry of the reflection high energy electron diffraction (RHEED) assisted Laser MBE system. Adapted from [79]

different growth modes of thin film. There are three major thin film growth modes: (1) FrankVan der Merwe or layer-by-layer growth, (2) VolmerWeber or island growth and (3) StranskiKrastanov growth, which are illustrated in figure 2.2 (a). These different growth modes can be described by using the simple thermodynamic models for the nucleation and growth, basically dominated by the surface energy of different interfaces. In layer-by-layer (LBL) growth the deposited atoms or molecules are more strongly bonded to the substrate than each other and each layer is progressively less strongly bonded than the previous layer, which in principal leads to the formation of each planner sheet before the second one. On the other hand, in the island growth mode the deposited atoms are strongly bonded to each other, therefore leading to the 3D cluster islands.

In order to control the growth down to unit cell scale, LBL mode is preferred, which could be tuned carefully by substrate surface treatment and choosing the right combination of growth conditions. Actually the different growth mode can be observed from the RHEED patterns. Figure 2.2 (b) shows the principal of RHEED. Similar to most diffraction techniques like TEM or XRD, RHEED pattern is also determined by the reciprocal lattice [81]. Then based on the different surface structures, the RHEED pattern presents different characters. For a nearly smooth 2D surface, the reciprocal lattice consists of the fine rods, which then lead to the sharp diffraction spots in a 2D pattern, as shown in figure 2.2 (c)1. As the smooth surface becomes rougher (for example formation of many steps in atomic scale), the reciprocal rods expand and the RHEED spots elongate (2.2 (c)2). When the surface becomes 3D islands, the diffraction is essentially the transmission diffraction of 3D clusters, which

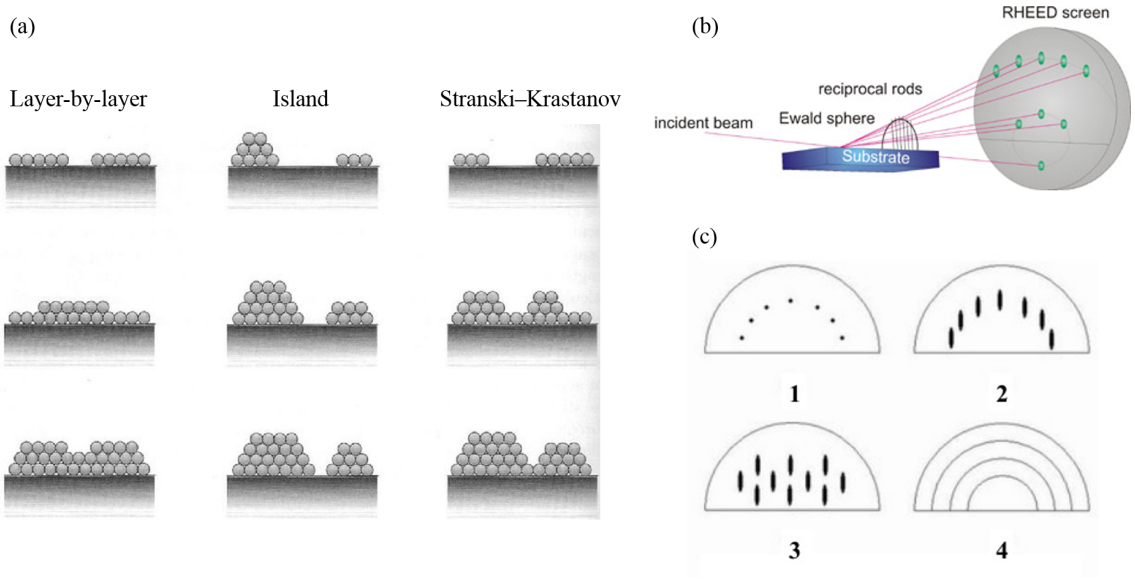

Figure 2.2: Schematic of thin film growth mode and respective RHEED patterns. (a) Illustrations of the basic growth modes including FrankVan der Merwe (layer-by-layer), VolmerWeber (island) and StranskiKrastanov growth. (b) Illustration of the RHEED patterns determined by the reciprocal space of surface. (c) Schematic of typical RHEED patterns for different surface structure: 1. nearly ideal smooth surface; 2. smooth surface with high density steps in atomical scale; 3. transmission diffraction from 3D clusters; 4. diffraction from noncrystalline or textured surface [79]

leads to the pattern quite similar to TEM diffraction pattern (2.2 (c)3). Finally if the film loses the epitaxy and becomes noncrystalline, the RHEED presents the power rings (2.2 (c)4). Therefore the RHEED pattern is quite sensitive to the surface structures.

If the film is stabilized in LBL growth mode, the intensity of RHEED pattern oscillates and the periodicity represent the formation of a planar sheet with one unit cell thickness. Figure 2.3 (a) shows the typical RHEED pattern of a smooth 2D surface, such as the surface of a high quality substrate. If the material is deposited in the layer-by-layer mode, the intensity (usually the specular spot) is determined by the surface coverage/roughness. When the coverage approaches 0.5, the surface becomes rougher and the intensity decreases. When the coverage approaches 1, the surface becomes smooth again and the intensity increases. Figure 2.3 (b) schematically shows the correlation between the film deposition process and the intensity oscillation. By using the RHEED intensity oscillation, we can realize the atomical control of material deposition.

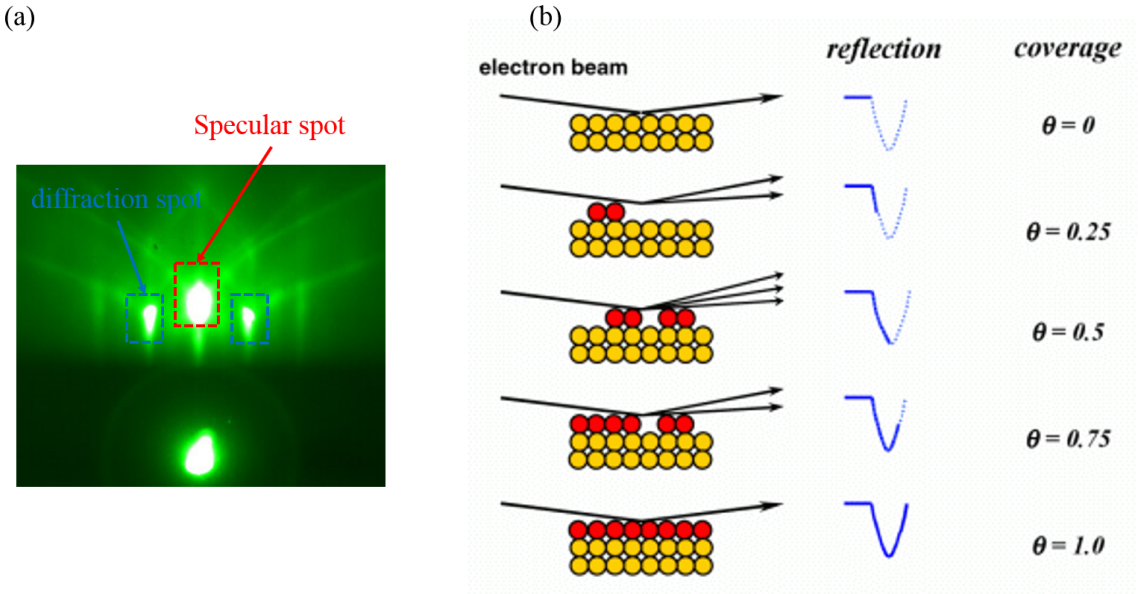

Figure 2.3: Schematic of RHEED intensity oscillation for the film in LBL growth mode. (a) Typical RHEED pattern of a smooth 2D surface. (b) Schematic of the correlation between the RHEED specular spot intensity and the surface coverage.

2.2 Structure characterization

2.2.1 X-ray diffraction

X-ray diffraction (XRD) is a routine analysis technique that is used by material scientists to get the crystal structural information such as the lattice constants, the octahedral rotation patterns, the texture relationship, etc. The overview of fundamental theory and application of X-ray diffraction techniques can be found in different literatures [82, 83]. As for thin film study in this dissertation, two kinds of modes are extensively used for the structural characterizations.

The first mode is θ-2θ measurement, which is done in a geometry where X-ray source is incident on the sample and the detector is used to collect the diffracted beam. In real measurements, the offset of θ is determined via alignment of single crystal substrate, the crystal structure of which is well-known. The θ-2θ measurement reveals a lot of information in the out-of-plane direction. Figure 2.4 shows a typical θ-2θ XRD measurement of one superlattice sample, from which many useful information can be extracted. Firstly the main Bragg diffraction peak (red) reveals that superlattice shows a good epitaxial growth on STO since only (001) diffraction peak is observed. Secondly, the satellite diffraction peaks (blue region), which correspond to the periodicity artificially created in superlattice, reveal the thickness of

each repetition and also the high quality of interface. Thirdly, the presence of Kiessig fringes reveals the information of total thickness and also indicates a smooth surface. The x axis is define by out-of-plane q vector L (corresponds to the reciprocal lattice $L = \lambda/(d \cdot \sin\theta)$.) Within this experiment geometry, another measurement is also widely used, which is the rocking curve scan. The rocking curve scan is a just θ scan with the 2θ angle fixed. As the θ angle moves away from the Bragg condition, the intensity of peak reduces significantly. Therefore the rocking curve can be used to quantify the degree of texturing along certain crystallography direction.

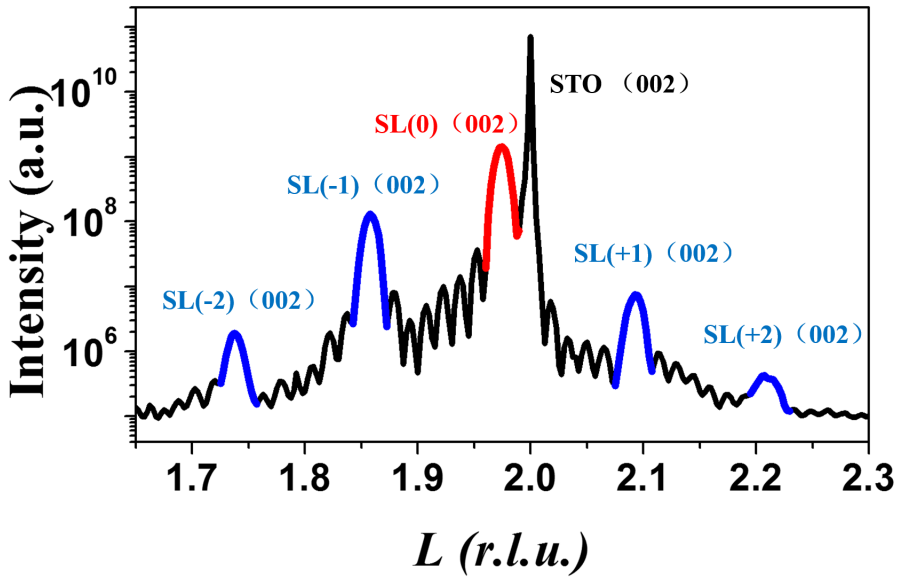

Figure 2.4: The θ-2θ XRD pattern of a superlattice sample. The substrate is STO (001) and the superlattice consists of 3 unit cells of $La_{0.7}Sr_{0.3}MnO_3$ and 5 unit cells of $SrIrO_3$ in one periodicity.

Furthermore, another mode of X-ray diffraction is also utilized in the thin film studies, mainly to gain more in-pane structural information. This technique is called reciprocal spacing mapping (RSM). As the name suggests, RSM is a full intensity mapping around certain diffraction peak (hkl). In real case, it consists of a serial of θ-2θ scans with one parameter changing and therefore covers the whole region of reciprocal spacing on and off the bragg peak. One of main information extracted from RSM is the in-plane lattice constant or the strain states. RSM around certain (hkl) with h,k$\neq$0 provides information about the in-plane axis. By comparing the lattice from film and substrate, an important term, whether the film is fully strained or not, can be extracted unambiguously. Actually high-resolution RSM over several

reciprocal peaks can be used to deduced the full set of parameters for the crystal structure.

2.2.2 Atomic force microscopy

Atomic force microscopy (AFM) is a very high resolution type of scanning force microscopy (SPM) that is used to image the surface structure and roughness. The principal of AFM is very straightforward. The information is gathered by 'feeling' or 'touching' the surface with a mechanical probe. Based on the working principals of AFM, a family of SPMs has been designed, one of which is the piezoelectric force microscopy (PFM). The basic operation mechanism will be discussed in the next section. As for AFM, two kinds of modes are usually used, i.e. contact mode and tapping mode. In contact mode, the tip directly contacts the surface of the sample and the contours of the surface are mapping out by the deflection of tips. In the tapping mode, the cantilever is driven to oscillate at or near its resonance frequency. As the tip approaches the surface, the amplitude and phase of the oscillations change, which provides information of the distance between the tip and sample surface. AFM offers a very high resolution in the Z direction, which is in the order of 0.1 nm. The length resolution in the film plane is limited by the size of tip, which is usually around 20-30 nm.

2.2.3 Transmission electron microscopy

Transmission electron microscopy (TEM) is a microscopy technique in which a beam of electrons is transmitted through an ultra-thin specimen, interacting with the specimen as it passes through. It offers very high resolution of image due to the small de Broglie wavelength of electrons, which enables the examination of fine details as small as a single column of atoms. The electrons are accelerated by high voltage (100-300 KeV) and then focused into a thin electron transparent sample. The transmitted electrons carries the information of the sample and are received by the phosphor screen. More details about the operation mechanism, theoretical description and experimental modes can be found in [84]. As for oxides thin film, the most widely used technique is the scanning transmission electron microscope (STEM), which is one type of TEM. It is distinguished from the conventional transmission electron microscopes (TEM) by focusing the electron beam into a narrow spot which is then scanned over the sample in a raster. By using a STEM and a high-angle detector (high-angle annular dark-field imaging, HAADF), it is possible to form atomic resolution images where the contrast is directly related to the atomic number (z-contrast image), which is heavily applied in the studying of oxides heterostructures. The contrast provides direct information of the sharpness of the interface. The rastering of the beam also makes STEM suitable for chemical analysis techniques such as mapping by energy

dispersive X-ray (EDX) spectroscopy or electron energy loss spectroscopy (EELS), which will also be used in the rest of the dissertation.

2.3 Electric characterization

2.3.1 Transport characterization

Transport measurements in this dissertation is performed by using the commercial Physical Property Measurement System (PPMS) from Quantum Design. The electrode contacts are made either by micro-fabrication process and wire-boding or directly attached by silver paste, depending on the size of contact area. The contact geometry will be presented in each case separately in the rest of the dissertation.

2.3.2 Ferroelectric characterization

There are two major methods to test the ferroelectric properties in the dissertation. The first one it to measure the ferroelectric polarization hysteresis loop, which is measured with Radiant Technologies Inc. RT6000S ferroelectric tester probe station. In the measurement, ferroelectric thin film is sandwiched by two electrodes and switching current is recorded during the ferroelectric polarization switch, which is then converted into the polarization magnitude. This method provides the macroscopically averaged information of the ferroelectric materials, such as the polarization value and the coercive field.

In order to get the microscopic information, a popular and widely used SPM technique, called Piezoresponse force microscopy (abbreviated as PFM in the rest of dissertation), has been extensively applied in studying ferroelectric materials. PFM is based on the detection of surface deformation due to the converse piezoelectric effect induced by the ac voltage applied to the tip. The typical experimental PFM setup for low-frequency imaging is very simple: it includes a commercial microscope working in a contact mode with conducting tip complemented with additional function generator and several lock-in amplifiers, as shown in figure 2.5. Basically an ac voltage from a functional generator is applied between the tip and the bottom electrode in the form:

$$V_{tip} = V_{dc} + V\cos\omega \cdot t \tag{2.1}$$

As the sample expands and contracts due to the converse piezoelectric effect, the tip deflection is monitored using a lock-in amplifier so that the tip oscillation

$$A = A_0 + A_{ac}\cos\omega \cdot t + \varphi \tag{2.2}$$

is recorded. Here A_0 is the static surface displacement and φ is the phase shift between the driving voltage V_{ac} and the voltage induced deformation A_{ac}. In other words, the

piezo-response is acquired simultaneously with the typologic [85]. Figure 2.5 (a)-(d) show the different forms of tip deflection that depend on the relative orientation between ac field and ferroelectric polarization, which makes it possible to analyze the in-plane (abbreviated as IP) and out-of-plane (OOP) polarization separately.

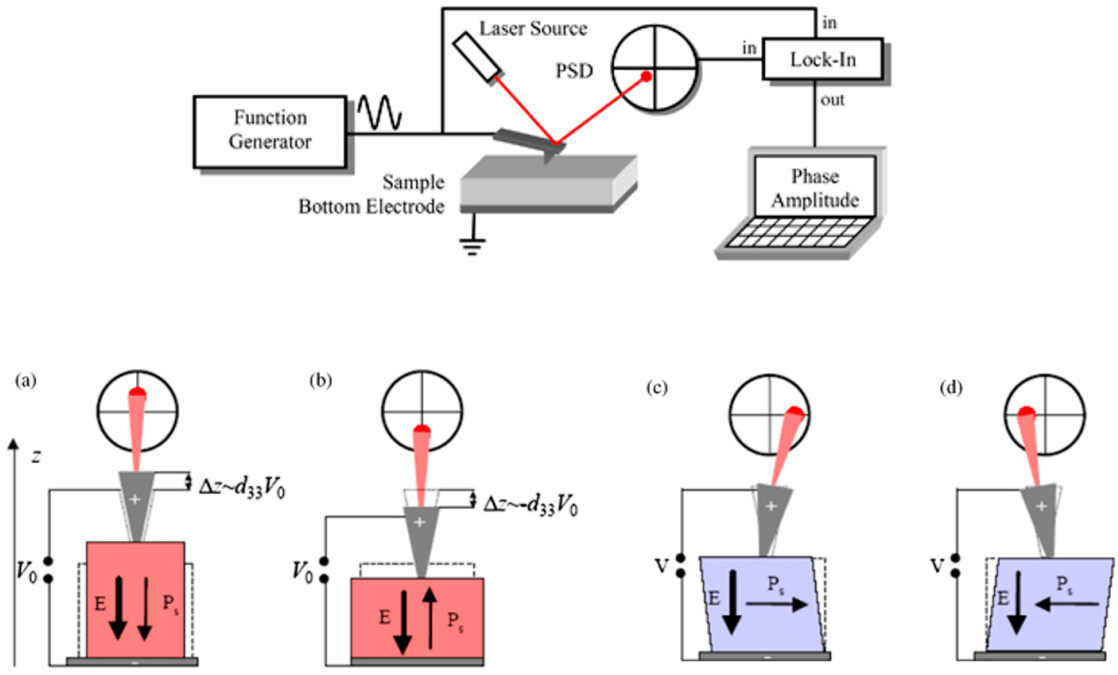

Figure 2.5: Piezoresponse force microscopy experimental setup and basic working principal. The upper panel shows the experimental setup for the simultaneous acquisition of topography and piezoresponse. An ac voltage from a functional generator is applied between the tip and the bottom electrode. The induced cantilever deflection is measured as an electrical signal by lock-in amplifiers. The different cases for deflection are shown in the bottom panel: (a),(b) Electric field aligned parallel or antiparallel to the spontaneous polarization results in a vertical displacement of the cantilever (d_{33} effect). (c),(d) Electric field applied perpendicular to the polarization results in a shear deformation related to d_{15} coefficient. Adapted from [86]

The PFM amplitude provides information on the magnitude of the local electromechanical coupling, while the PFM phase image provides information on the ferroelectric domain orientation. Typically the imaging resolution of PFM is ultimately limited by the tip and sample contact area, which is about 30nm. Therefore PFM can be used in two modes, the image mode provides the information of local ferroelectric domains and the spectroscopy mode (voltage hysteresis) provides the magnitude of piezo-response efficiency (can be converted to d_{33}) and the coercive field.

To use the PFM image (amplitude and phase) to reconstruct the ferroelectric

domain, one should understand the relationship between the confinements of crystal symmetry and the PFM contrast from different scanning directions. As for the rhombohedral $BiFeO_3$, the standard has been established in early literatures [87].

2.4 Magnetic characterization

The magnetism are characterized by two major methods. The commercial MPMS magnetometer with Quantum Design (SQUID) is used to get the magnetization information at different temperature and fields macroscopically. However, another powerful technique, which is based on the synchrotron X-ray absorption, is also used to provide additional information. Figure 2.6 (a) shows the process of X-ray absorption (XAS). Core electrons are excited in the absorption process into empty states above the Fermi energy and the energy is the fingerprint of each element. The L-edge x-ray absorption spectra ($2p$ to $3d$) of the transition of metals and oxides are dominated by two main peaks (L_2 and L_3), which arise from the spin orbit interaction of the 2p core shell and the total intensity is proportional to the number of holes in d orbital.

If the X-ray is polarized, then we can expect the dichroism. The origin of the dichroism effect can be anisotropy of the charge or the spin in the material. Depending on the nature of X-ray polarization, X-Ray Magnetic Circular Dichroism (XMCD) and X-Ray Magnetic Linear Dichroism (XMLD) are widely used. The concepts of XMCD spectroscopy, which is illustrated in reference [89], is shown schematically in figure 2.6 (b) and (c). For a magnetic material the d shell has a spin moment which is given by the imbalance of spin-up and spin-down electrons or holes. In order to measure the difference in the number of d holes with up and down spin, we need to make the x-ray absorption process spin dependent. This is done by use of right or left circularly polarized photons which transfer their angular momentum to the excited photoelectron. If the photoelectron originates from a spin-orbit split level, such as the $p_{3/2}$ level (L_3 edge), the angular momentum of the photon can be transferred in part to the spin through the spin-orbit coupling. Since the $p_{3/2}$ (L_3) and $p_{1/2}$ (L_2) levels have opposite spin-orbit coupling, the spin polarization will be opposite at the two edges. Therefore the the XMCD signal has different sign of different absorption edge. Actually the XMCD spectra can be quantitatively related by sum rules to the number of d holes and the size of the spin and orbital magnetic moments. The spin moment is propositional to A-2B and the orbital moment is propositional to A+B.

For XMLD spectroscopy, the electric field vector E of linearly polarized x-rays acts as a search tool to probe the charge distribution of holes caused by anisotropy bonds Therefore it is a perfect tool to study the lattice-orbital couple and the effect of strain engineering. Furthermore, in magnetic ordered materials, spin-orbit coupling leads to preferential charge order relative to the spin direction, which is the basis for the determination of the spin axis in ferromagnetic and especially antiferromagnetic systems. Actually XMLD has been widely used to determine the antiferromagnetic

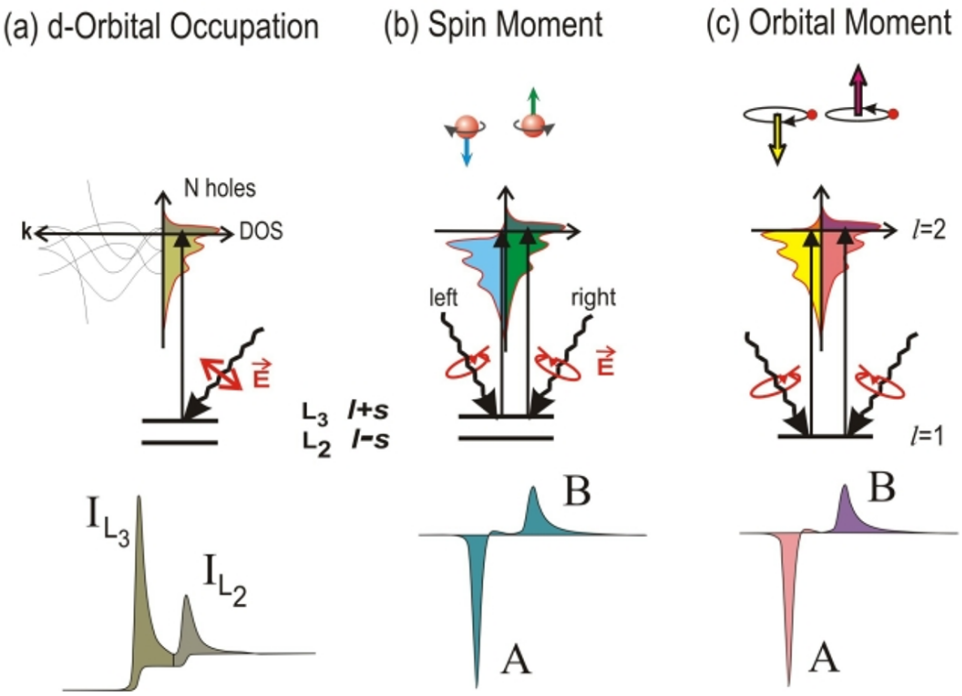

Figure 2.6: Principal of X-ray magnetic circular dichroism. (a)Electronic transition in conventional L-edge x-ray absorption. (b),(c) X-ray magnetic circular dichroism illustrated in a one-electron model. The transitions occur from the spin-orbit split 2p core shell to empty conduction band states. In conventional x-ray absorption the total transition intensity of the two peaks is proportional to the number of d holes (first sum rule). By using the circularly polarized x-rays the spin moment (b) and orbital moment (c) can be determined from linear combinations of the dichroic difference A and B, according to other sum rules. Adapted from [88]

axis, which is not sensitive to other experimental methods (figure 2.7 (b)).

Finally let's sum up the two techniques. Both of the two techniques are based on X-ray absorption and therefore the information are element selective (figure 2.7 (a)), which is perfect to study the heterostructures with different components. Moreover, the information can be related to either surface or bulk depending on the way to collect data. For example, total-yield-electrons come from just a few nanometers at the surface, which makes the information quite surface sensitive. On the other hand, the fluorescence signal originates from the bulk of materials. XMCD is commonly used to study ferromagnetic materials since it provides the information of magnetization direction, magnitude and spin and orbital components. XMLD (XLD) is usually utilized to determine the orbital splitting by strain or the antiferromagnetic axis.

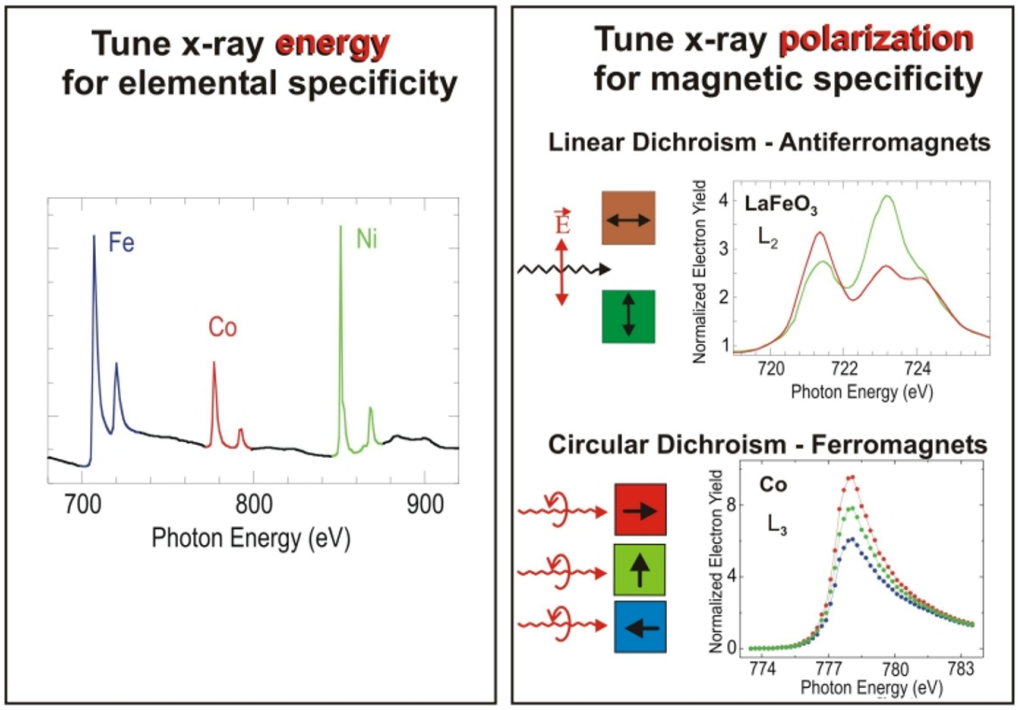

Figure 2.7: Schematic of XAS, XMLD and XMCD experiment. (a) XAS spectra of different elements, which demonstrates the advantage of element-selection. (b)X-ray magnetic linear dichroism of $LaFeO_3$ with different antiferromagnetic axis. (c)X-ray magnetic circular dichroism of Co with different spin orientations. Adapted from [88]

Chapter 3

Interface engineering of magnetoelectric coupling in BFO/LSMO heterostructure

This chapter presents the results on how to use the interface atomical structure to tune the magnetoelectric coupling in the $BiFeO_3/La_{0.7}Sr_{0.3}MnO_3$ heterostructure, which is one model system to explore the combination of route 1 and route 3 in figure 1.9. A series of previous works unambiguously demonstrated the electric control of exchange bias coupling in this system, which therefore motivated more efforts to optimize the coupling coefficient. The results in this chapter demonstrate that the interface atomic sequence, a neglected factor previously, actually imposes a significant effect on the magnetoelectric coupling.

The first section will cover the fundamental knowledge of the multiferroic $BiFeO_3$ and ferromagnetic $La_{0.7}Sr_{0.3}MnO_3$. Then the previous work will be briefly reviewed. The fabrication method will be discussed in the next section to show how to control the interface atomic sequence. Then the third section presents the key results on the exchange bias coupling of two different interfaces under electric field control.

3.1 Previous work of model system BFO/LSMO

3.1.1 Introduction of BFO and LSMO

As mentioned briefly in the first chapter, $BiFeO_3$ (abbreviated as BFO) is the only single-component multiferroic at room temperature. Although it has been intensively studied in terms of mangnetoelectric coupling since the stabilization of thin film in 2003 [19], it is actually a pretty old material. Polycrystalline BFO Powders have been successfully synthesized more than half a century ago. Structure characterization revealed a rhombohedrally distorted perovskite-like structure corresponding to space

group R3c. Two main types of lattice distortions were observed. The first one is the cation displacement along [111], which is the origin of ferroelectricity (figure 3.1 (a)). Secondly, oxygen octahedral rotates out of phase ($a^-a^-a^-$) about 13 degrees around the [111] axis [90] (figure 3.1 (b)).

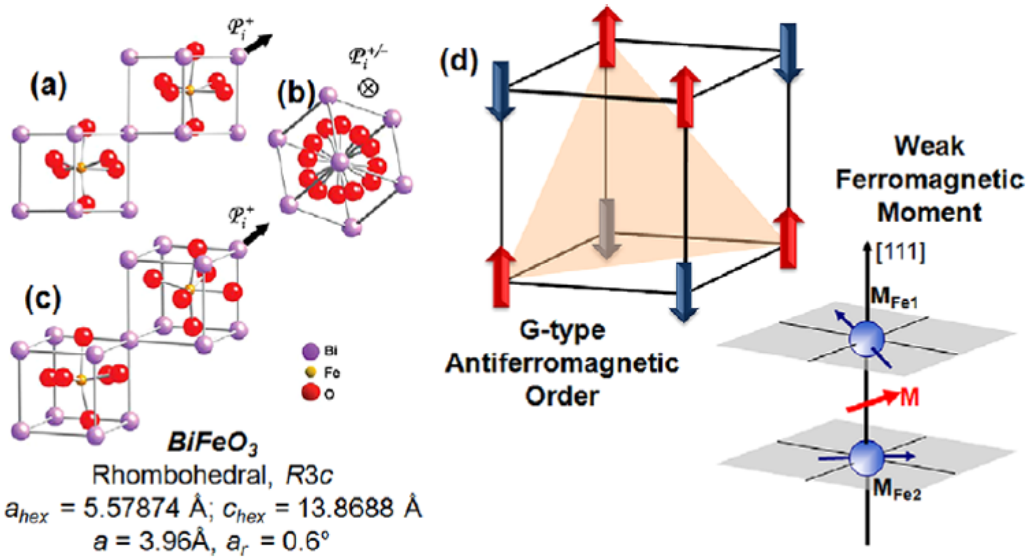

Figure 3.1: Crystallography and magnetic structure of BFO. (a) Projected structure along pseudocubic-[110]. (b) Projection along the pseudocubic-[111]. (c) A general three dimensional view of the structure. (d) Schematic of G-type antiferromagnetic ordering of BFO. (e) Schematic of the weak ferromagnetism moment due to canting. Adapted from [91]

Although being identified as a ferroelectric material with high curie temperature, early electric measurement revealed a very small polarization value, $\sim 6.1 \mu C/cm^3$ along [111] direction, controversial to the high T_c [92]. In 2003, Wang et al fabricated the high quality thin film of BFO and measured the polarization to be an order of magnitude higher, $\sim 90 \mu C/cm^3$, which is then also confirmed in single crystal BFO [93]. Therefore it is likely the small value in the early age is related to the poor sample quality. The high curie temperature ($\sim$1100K) has been proved by different experiment methods [90,94]. It is worth mentioning that the ferroelectricity originates from Bi $6s$ electrons, which has been discussed in the first chapter.

With the knowledge of magnetic coupling in chapter 1, it is easy to understand the magnetic ordering of BFO. Since Fe^{3+} cation has five d electrons and is in the high spin state, the nearest neighboring spins couple antiferromagnetically with each other due to the superexchange coupling, which yields the G-type antiferromagnetism with Neel temperature $\sim$670K [90]. Furthermore, a cycloidal structure along [111] direction with the periodicity of 62 nm was also observed [95] in bulk BFO. On the other hand, the

lattice-mismatch-induced strain is found to break the easy-plane magnetic symmetry of the bulk, which depresses the cycloidal structure [96]. Furthermore, the magnetic easy axis can be crafted by using epitaxial strain from substrates [97]. Finally it is worth mentioning that the canting of the antiferromagnetically coupled moments is permitted by the symmetry of BFO, which leads to a tiny net moment as shown in figure 3.1 (e) that is referred as the weak ferromagnetism due to Dzyaloshinskii-Moriya interaction.

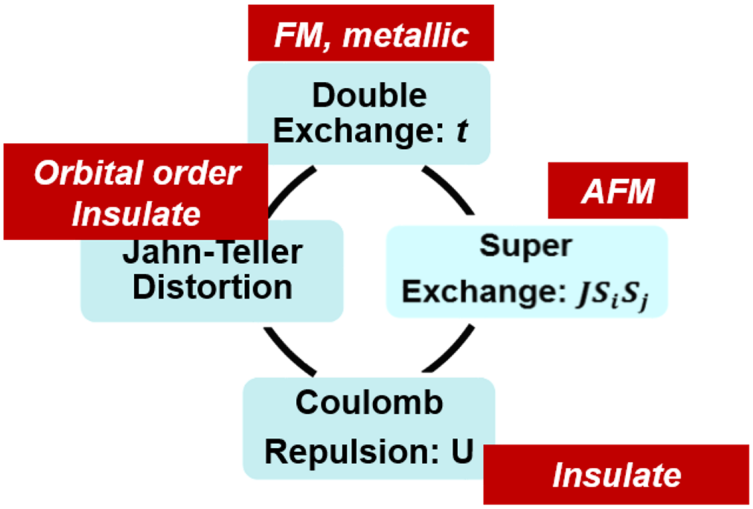

Figure 3.2: Summary of different competing energy terms in manganite system. The ground state of manganite is determined by the competition between double/super-exchange, columbic interaction and Jahn-teller distortion, which prefer different electronic/magnetic ground states. Generally speaking, double exchange is compatible with metallic FM, super-exchange is associated with localized electrons, the same effect as the columbic interaction. Jahn-teller distortion usually lifts the orbital degeneracy, which leads to the decrease of bandwidth.

LSMO is one member of the big family of manganites, which has been one hot topic in the condense matter physics for many decades. The enormous number of studies were first triggered by the discovery of ferromagnetism in mixture of two antiferromagnetic parent phase and was latter demonstrated to show the colossal magnetoresistance (CMR) [98]. Ever since then a full careful mapping of manganites with different A-site cations (different size and doping ratio) have been carried out and a great deal of interesting phenomena have been reported in different degrees of freedom. The rich physics of manganites has been reviewed in details in reference [44].

The varieties of different ground states in manganite originates from the comparable energy scale of different competing energy terms. As shown in figure 3.2, the double-exchange interaction is dominate by the electron transfer integer t and favors

a metallic ferromagnetic ground state. The columbic repulsion U favors the insulating state. At certain doping level, collective Jahn-teller distortion would further lift the degeneracy of orbital, which leads to orbital ordering and insulating state. All these terms are similar in magnitude of energy, which leads to a rich spectrum of novel functionalities and physics. Despite of the complexity, manganite can be divided into three main groups based on the A-site cation size. As discussed in chapter 1, the physics of transition metal oxides strongly depends on the nature of B-O-B bond, which is closely tied to the size of A-site cation. In manganite, the La-Sr and La-Ba cation mixture has the largest size, which yields to a maximal bandwidth (or the transfer interger). Therefore they are usually ferromagnetic metal. As the size decreases, for example the mixture of Nd-Sr, Pr-Sr or La-Ca, the bandwidth reduces and becomes comparable in magnitude with Jahn-teller distortion and columbic energy. Therefore charge ordering and metal-insulator ferromagnetic-antiferromagnetic transition have been observed in this series at intermediate temperature. Further reduction of A-site size leads to the smallest bandwidth, insulating ground state and orbital ordering with very high transition temperature.

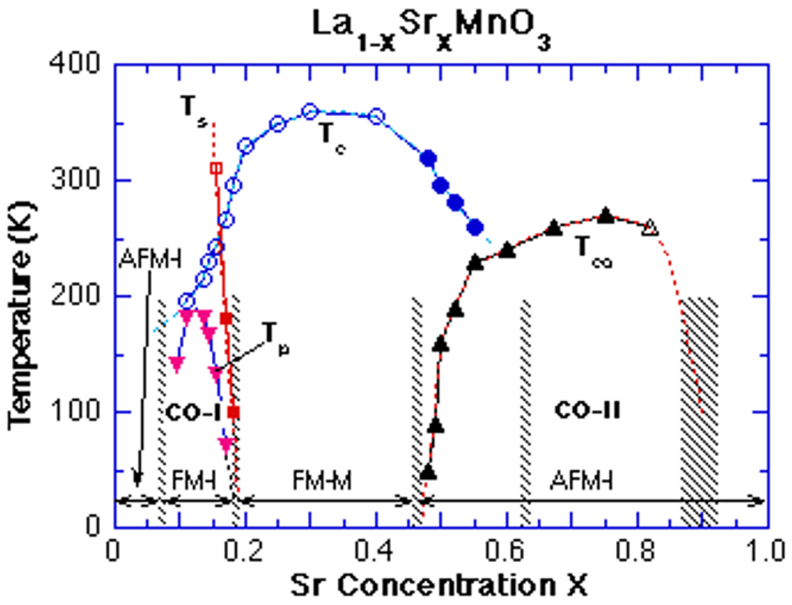

Figure 3.3: Phase diagram of $La_{1-x}Sr_xMnO_3$. Phase diagram of $La_{1-x}Sr_xMnO_3$ as a function of doping ratio. AF: antiferromagnetic; FM: ferromagnetic; I: insulator; M: Metal. Adapted from [99].

The phase diagram of the large bandwidth $La_{1-x}Sr_xMnO_3$ is shown in figure 3.3. On the left side the parent compound is $LaMnO_3$, in which the Mn cation has 4 d electrons. $LaMnO_3$ has been identified to possess an orbital ordering pattern, which then prefers the A-type antiferromagnetic ordering and Mott insulating. On the

other side, SrMnO3 has 3 d electrons and therefore a band insulator with G-type antiferromagnetic ordering. By progressive doping of LMO, various magnetic and charge ordered phases emerge. At first it is ferromagnetic and insulating, in which the magnetization might originate from canting effects. Then it becomes metallic ferromagnet where double-exchange interaction dominates. Further doping leads to an antiferromagnetic insulating ground state. Several different charge orderings are observed at some commensurate doping values as shown in the diagraph. It is worth emphasizing that the optimal doping x$\sim$1/3 in the $La_{1-x}Sr_xMnO_3$ series exhibits the highest Curie temperature of 380K and a nearly 100 percent spin polarization [100]. In the work presented in this chapter we use the $La_{2/3}Sr_{1/3}MnO_3$ compound, which will be abbreviated as LSMO in the following.

3.1.2 Magnetoelectric coupling in BFO/LSMO heterostructure

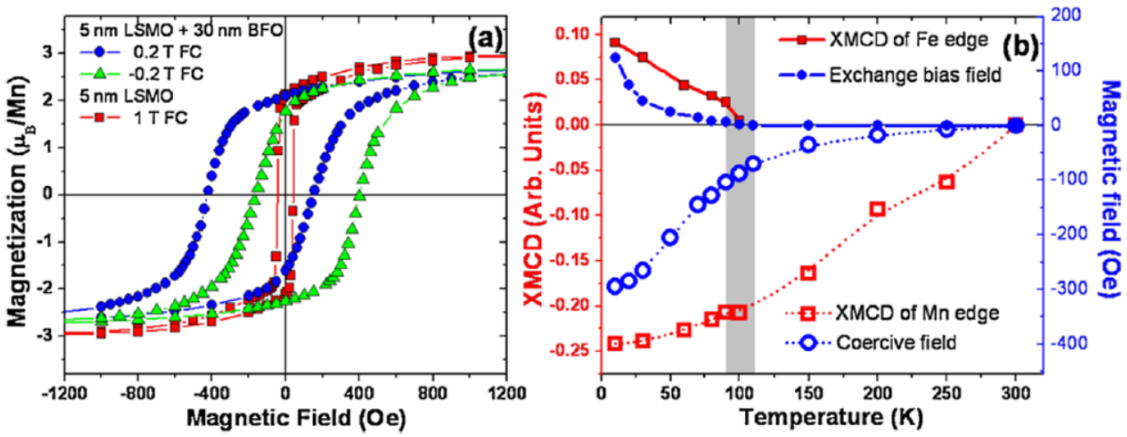

Figure 3.4: Exchange bias coupling of BFO/LSMO heterostructure. (a) Exchange bias in BFO/LSMO heterostructure at 10K after field cooling in opposite directions. (b) The correlation between XMCD and magnetic properties. Adapted from [101].

The early research on the magnetoelectric coupling in BFO/LSMO heterostructure was first inspired by the unexpected exchange bias [101]. Exchange bias, one of the most important phenomena which was first discovered in the 1950s [102], has been widely used in the architecture of modern magnetic memory device units [103]. The characteristic signature of exchange bias is the shift of the center of magnetic hysteresis loop from its normal position at H=0 to $H_E \neq 0$. It occurs in a large variety of systems which are composed of an antiferromagnet (AF)that is in atomic contact with a ferromagnet (FM). The traditional mechanism proposed to understand this

phenomena has two major points: the uncompensated spins at the interface of AF and the large anisotropy energy of the AF [104]. The uncompensated spins, which remain unchanged during the FM spin flip, are the origin of this unidirectional anisotropy. More details about the microscopic model and theoretical description can be found in the reference [72, 104, 105].

BFO is the G-type antiferromagnet (anti-parallel between nearest neighbors, figure 3.1 (d)). Therefore there are no uncompensated spins at the (001) surface. Surprisingly the exchange bias was observed in the heterostructure as shown 3.4 (a). Furthermore XMCD measurements revealed the onset of enhanced ferromagnetism of BFO at the interface, which is closely related to the exchange bias (figure 3.4 (b)). The blocking temperature (when H_E decreases to zero) of exchange bias is ∼100K in this system. The enhanced moments of interfacial BFO are likely due to the strong coupling with FM LSMO, which then leads to a frustrated state at the interface, especially at the domain walls.

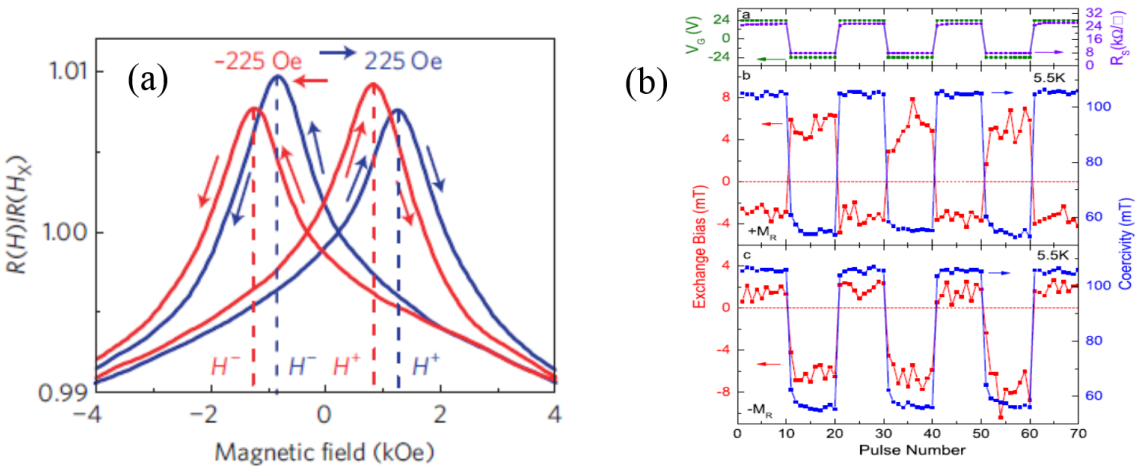

Figure 3.5: Electric control of exchange bias coupling in BFO/LSMO. (a) Transport measurement that is used to demonstrate the exchange bias. (b) Electric control of exchange bias and coercive field under sequence of gate voltage. Adapted from [106, 107].

More interestingly, the exchange bias was demonstrated to be electric controllable [106, 107]. Figure 3.5 (a) shows the transport measurement that is used to test the exchange bias when the heterostructure is patterned into devices. The red and blue curves correspond to the opposite field cooling directions. The shift of the loop center, the sign of which is determined by the field direction, is the character of exchange bias. By using the device in the Field-effect-transistor (FET) geometry, successive positive and negative voltage is applied on the gate to switch the ferroelectric polarization of BFO as shown in figure 3.5 (b) (top panel) and then the exchange bias is measured

at each polarization state. The middle and bottom panel of figure 3.5 (b) reveal the modulation of exchange bias and coercivity in different polarization states. The sign reversal of the exchange bias implies the occurrence of 180 degree switch of spins at the interface during the ferroelectric switch process. The remanent magnetization (field cooling direction) is opposite for the middle and bottom panel. However both show the similar electric control behavior. Therefore it has been clearly demonstrated that the exchange bias could be deterministically controlled by electric field, although with a relatively low blocking temperature.

3.1.3 BFO/LSMO interface engineering

The ideal of interface engineering has been applied in oxide thin film heterostructure for a long time. For example in the half-metallic LSMO magnetic tunneling junction, it was found that a few monolayer of $LaMnO_3$ will greatly enhance the magnetoresistance, which is due to the charge transfer at the interface [108]. In the high T_c superconductor YBCO, interface modification was applied to create the Josephson junctions. [109]. Another kind of interface structure, the atomic stacking sequence attracted attentions after Kawasaki el al successfully prepared the $SrTiO_3$ (STO) substrate with single termination surface [110]. The crystal structure of perovskite has been discussed before in chapter one. As shown in figure 1.3 (a), it actually has two possible terminations (sub-layer), AO and BO_2, in terms of (001) surface. Therefore one can imagine that there are two kinds of interface with different atomic stacking sequences.

The importance of interface atomic sequence attracted more and more attentions after the pioneer work of $LaAlO_3/SrTiO_3$ 2d electron gas (2DEG) [62]. In this work it was shown that the 2DEG is only observed at the interface with TiO_2-LaO-AlO_2, but not in TiO_2-SrO-AlO_2. The mechanism is explained in the so-called polar discontinuities or polar catastrophe [63]. In STO, both $Sr^{2+}O^{2-}$ and $Ti^{4+}O_2^{2-}$ layers are charge neutral, while charge states in the LAO are positive for $La^{3+}O^2$ layer, and negative for $Al^{3+}O_2^2$. The polarity discontinuity arises at the interface, leading to divergent electrostatic potential, which is called as polar catastrophe. To avoid the associated large energy cost, a net charge transfer across the interface is energetically favorable. The LaO/TiO_2 interface attracts extra electron, which fills the empty d orbital of Ti^{4+} and leads to the metallic 2DEG. On the other hand, SrO/AlO_2 interface favors extra hole, which in real case is compensated by valencies and results in a semiconducting behavior.

Inspired by this work, the interface engineering of atomic sequence is carried out in BFO/LSMO heterostructure [111]. It was found that the interface can actually determine the direction of bulk ferroelectric polarization. Figure 3.6 shows the two kinds of interface here: MnO_2-BiO-FeO_2 (interface A) and MnO_2-LaSrO-FeO_2 (interface B). The PFM images clearly demonstrate the as-grown polarization is opposite in A and B, which can be explained as the different polar discontinuity that leads

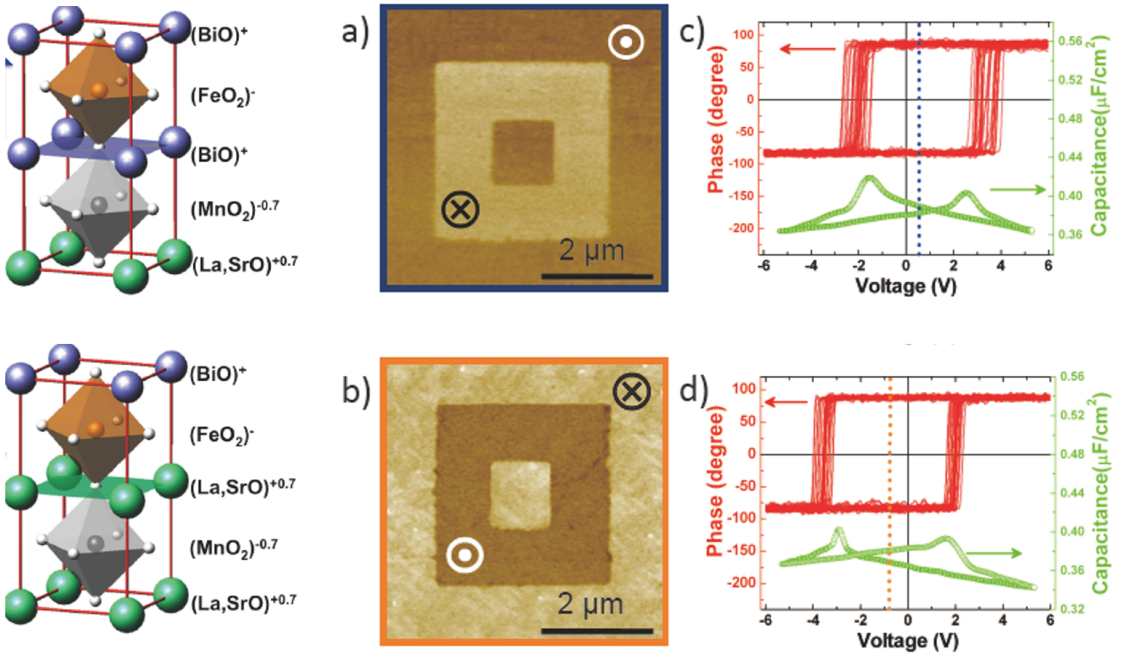

Figure 3.6: Interface control of bulk ferroelectricity. The left image shows the schematic of two interface atomic sequence of BFO/LSMO heterostructure. (a) PFM and (c) d_{33} hysteresis of MnO_2-BiO interface. b) PFM and (d) d_{33} hysteresis of LaSrO-FeO_2 interface. Adapted from [111].

to the opposite interface electrostatic potential. This can be proved by checking the shift of d_{33} hysteresis loops, which are opposite as shown in figure 3.6 (b) and (d). In summary, the interface engineering can alter the bulk properties far away from the interface. However it remains an puzzle that how the interface engineering modifies the magnetoelectric coupling across the interface, which is the central topic of this chapter.

3.2 Fabrication of BFO/LSMO with different interfacial atomic sequence

All of the growth in this chapter were performed on $SrTiO_3$ (001) (STO) single crystal substrates, which provide good lattice match to BFO and LSMO. Before the growth, a buffered HF acid-etch and thermal treatment process was used to obtain fully TiO_2 (B site)-terminated surfaces [110]. Atomic force microscopy (AFM) measurements reveal the perfect one unit-cell-height terrace structure (figure 3.7 (a)), which confirms the single terminated substrate.

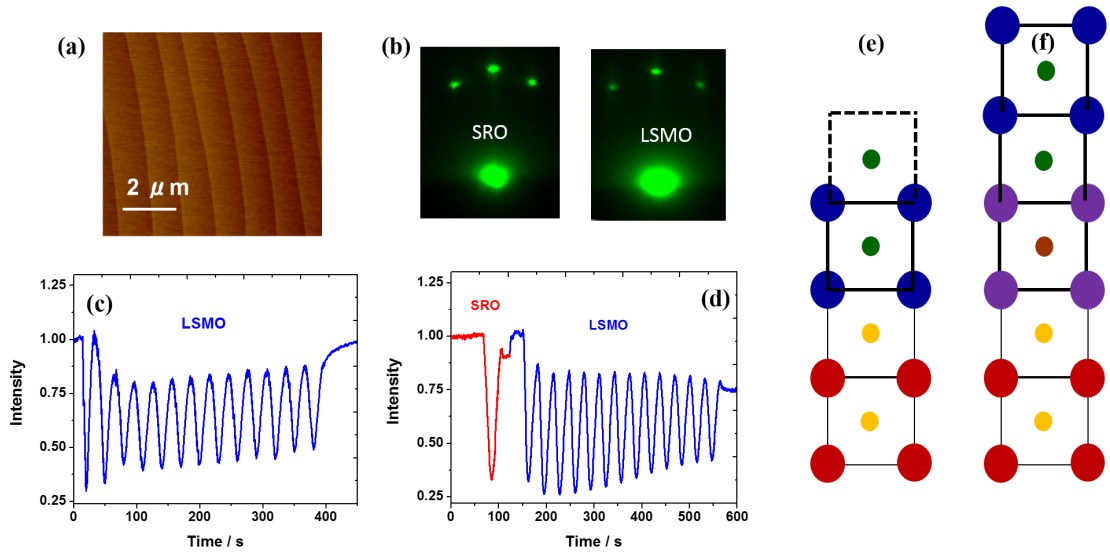

Figure 3.7: Fabrication of BFO/LSMO with different terminations. (a) AFM image of chemically and thermally treated STO substrate. (b) RHEED pattern of SRO and LSMO grown on the substrate. (c),(d) RHEED oscillations of LSMO and SRO/LSMO on STO. (e), (f) Schematic of two different surface terminations followed by the procedure in (c) and (d), red refers to STO, blue refers to LSMO and purple refers to SRO, only two unit cells of LSMO are shown here.

LSMO is grown at 690 C and 150 mTorr. Figure 3.7 (c) shows the RHEED oscillations of 13 unit cells of LSMO grown on treated STO substrate, which demonstrates a good layer-by-layer growth mode. The post-growth RHEED pattern of LSMO still preserves the 2D RHEED pattern and AFM reveals similar morphology as the substrate. Since the substrate is treated to be B-site terminated, the LSMO is also terminated with MnO_2 sub-layer as shown in figure 3.7 (e). Then BFO is deposited at the same growth condition and the interface atomic sequence was MnO_2-BiO-FeO_2 (interface A). The key point to achieve the second interface atomic sequence is to use $SrRuO_3$ (SRO). It has been demonstrated that the during the growth of SRO a self-organized conversion of the terminating atomic layer from RuO_2 to SrO occurs [112] at the first unit cell. Therefore the surface is switched to A-site termination with an atomically flat morphology as shown by both AFM and RHEED pattern (figure 3.7 (b)). LSMO keeps the layer-by-layer growth mode on SRO as revealed by the RHEED oscillations in figure 3.7 (d) and ends up with LaSrO sub-layer. Thus the MnO_2-LaSrO-FeO_2 (interface B) is successfully fabricated (shown schematically in figure 3.7 (f)). All the heterostructures deposited in this chapter consist of 200nm BFO and 13 unit cells of LSMO. One oscillation of SRO is deposited on STO to

switch the termination.

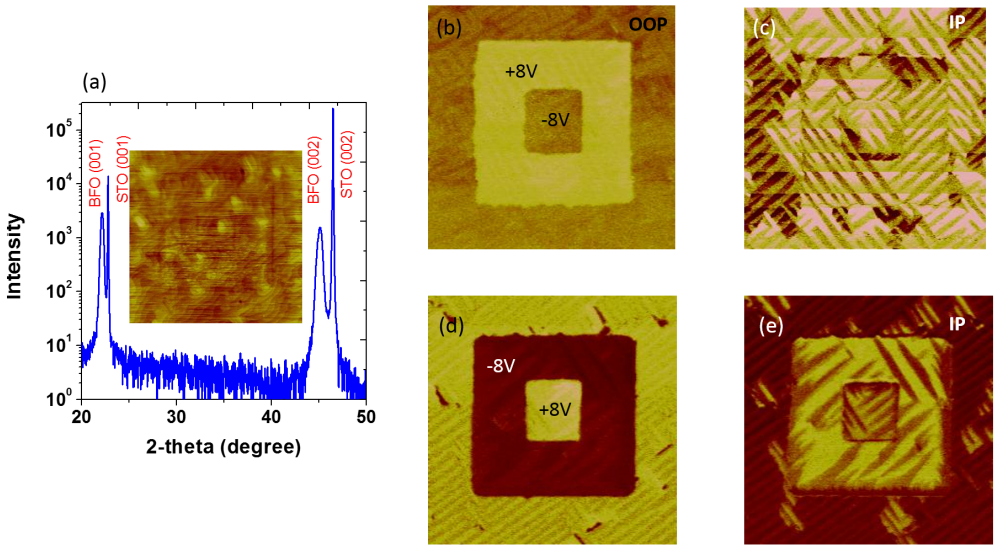

Figure 3.8: Structure characterization and PFM of BFO/LSMO with different terminations. (a) XRD θ-2θ scan of BFO/LSMO heterostructure. (b), (d) Out-of-plane PFM image of BFO/LSMO heterostructure with interface A and B. The polarization direction is checked by the box-in-box switch (c),(e) In-plane PFM image of BFO/LSMO heterostructure with interface A and B.

Structural characterizations of BFO/LSMO heterostructures were carried out by using x-ray diffraction (XRD) as shown in figure 3.8 (a), which reveals the pure phase of BFO. The inset of figure 3.8 (a) is the AFM image of one BFO/LSMO heterostructure, which shows the flat surface with atomical terrace. This is consistent with our previous work and reveals the high quality of crystal structure. PFM is also performed to check the polarization direction as well as the domain structures during the switching process. During the scan, ac bias of 4 V_p at 6.39 kHz is applied to the conducting probe, which scans along the [1-10] direction. The procedure to use PFM to map the ferroelectric domains of BFO can be found in [113]. Figure 3.8 (b)-(e) show the OOP and IP ferroelectric domain structure of BFO (60 nm) /LSMO (5 nm) heterostructure with different terminations. Two opposite voltages were applied successively to switch the ferroelectric polarization and the polarity of voltage is shown in the figures. The as-grown polarization in the OOP images exhibits the same interface control phenomena as the previous work [111]. The IP images show similar stripe-like ferroelectric domain structures (71^o domains) in BFO layer in both interfaces.

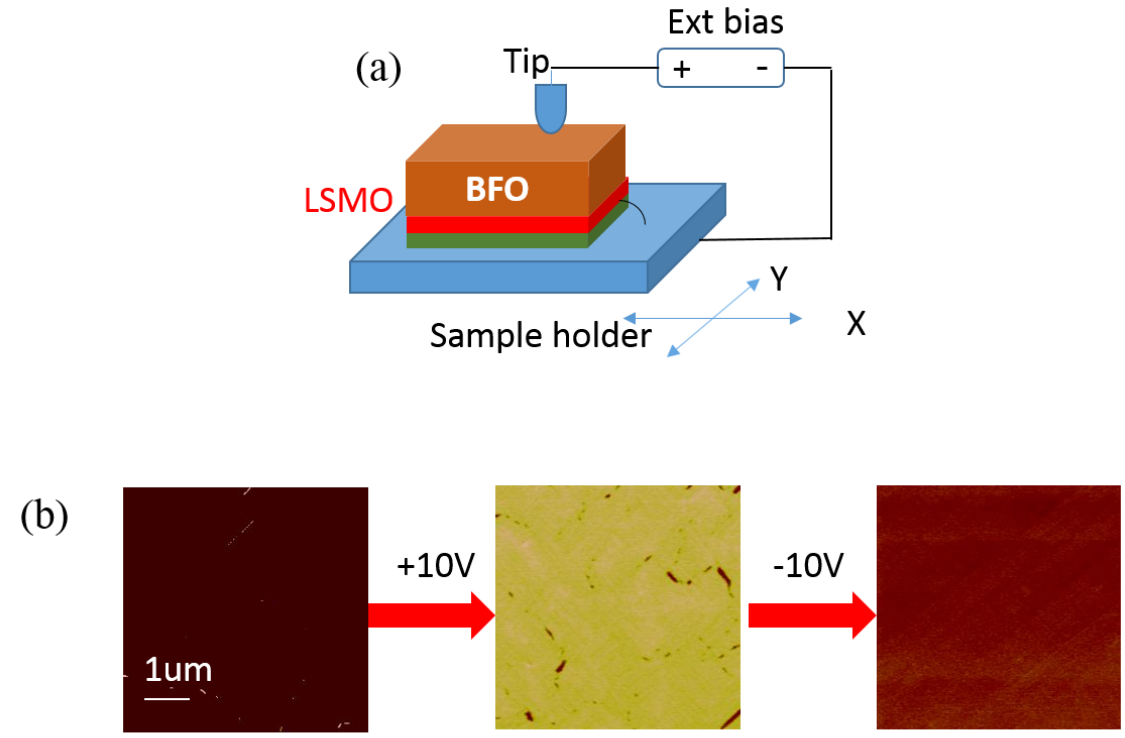

Figure 3.9: Macroscopic switch of BFO polarization. (a) Schematic of the scanning metal-probe setup to macroscopically switch the BFO. The sample holder can move in X and Y direction to fully pole the entire sample. (b) OOP PFM images of as-grown, positively switched and negatively switched BFO/LSMO heterostructure with interface A.

3.3 Magnetoelectric coupling behavior of different interfaces

In order to study the magnetoelectric coupling of the two kinds of interfaces, the ferroelectric polarization of BFO layer is switched macroscopically by using a scanning metal-probe setup (see figure 3.9 (a)). The working mechanism is very similar to that of PFM except that the metal probe has a 50 μm diameter spherical tip, which leads to a tip-sample contact area of tens of μm^2 that makes the macroscopic switching possible. Due to the round-tip geometry, the poled region has a high coverage of the sample area. Figure 3.9 (b) shows the randomly selective OOP PFM image of the BFO/LSMO (interface A) in the as-grown state, switched by positive voltage and reversed back by the negative voltage, which reveals the nearly 100 percent switch of the OOP polarization and the high stability in each polarization state.

As macroscopic measurements are possible in our samples, we measure directly the magnetization of the samples by using state-of-the-art magnetometer, MPMS SQUID, instead of using microscopic methods, such as magneto-optic Kerr effect [67, 114], photoemission electron microscopy [74] or magnetic transport [106].On the identical samples, we can compare the magnetic hysteresis loops measured before and after the ferroelectric polarization switch, as shown in figure 3.10 (a). Additionally the samples have been switched back to check the reversibility of the effect. In the discussion below, the direction of ferroelectric polarization is called as upwards or downwards with respect to the interface. The in-plane components are neglected because of the less importance and similarity before and after the switch.

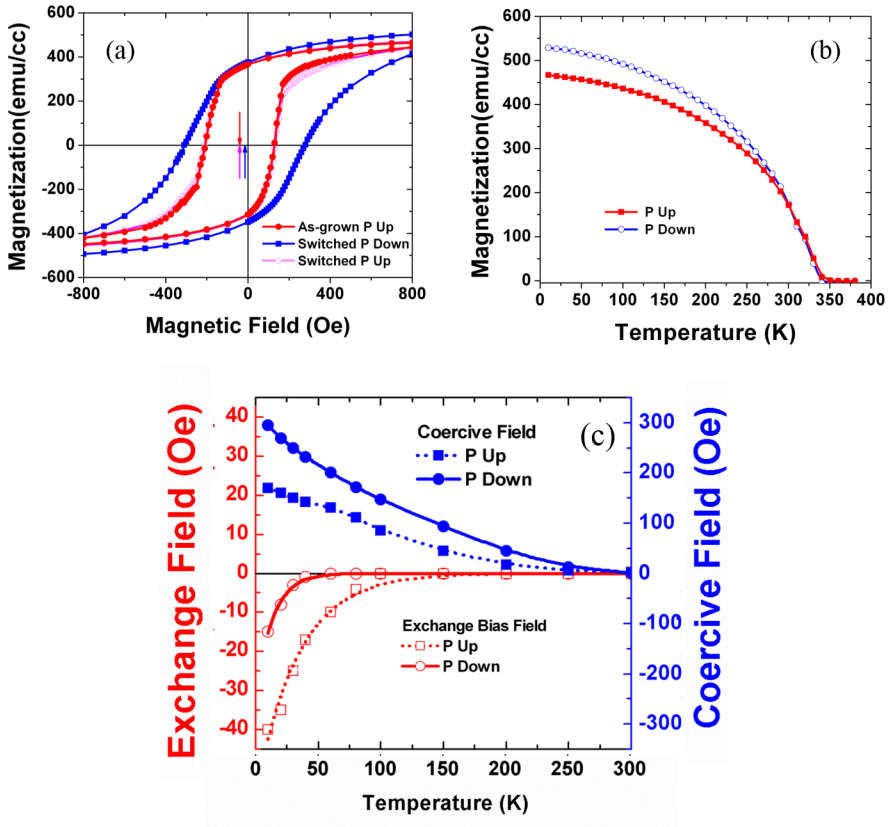

Figure 3.10: Magnetoelectric coupling of interface A. (a) Magnetic hysteresis of BFO/LSMO with interface A in different polarization states. (b) Magnetization versus temperature of the different polarization states. (c) Temperature dependance of exchange bias and coercive field of interface A.

For BFO/LSMO heterostructures with interface A, three notable changes can be clearly observed from the measurements when the polarization state is switched from upwards to downwards: (1) enhancement of the saturation magnetization from 470

emu/cc to 530 emu/cc, which is further confirmed by the temperature dependence of magnetization as shown in Figure 3.10 (b); (2) suppression of the exchange bias from 45 Oe to 20 Oe; (3) change of in-plane anisotropy with the enhancement of coercive field from 170 Oe to 300 Oe. Note that such a control is fully reversible by the application of an electric-field: when the ferroelectric polarization is switched back to the original upward state, the magnetic properties of the heterostructures are indeed switched back to the initial state. The detailed analysis of the temperature dependence of the observed magnetization, coercive field, as well as exchange bias field (Figure 3.10 (b) and (c)), provides further physical insight into this magnetoelectric coupling. The measurements reveal a clear tunability of both the magnetization and coercive field (blue curves in 3.10 (c)) at temperatures up to about 300 K. Similarly, the study of the exchange bias field (red curves in 3.10 (c)) reveals a reduction in both exchange bias field and transition temperature (blocking temperature) as the ferroelectric polarization is switched from upward to downward.

On the other hand, the BFO/LSMO heterostructure with interface B shows a different magnetoelectric coupling effect as compared with interface A, which is revealed by figure 3.11. First of all, the saturation magnetization reduces from 480 emu/cc to 390 emu/cc as the ferroelectric polarization is switched from downwards (as-grown) to upwards. The modulation is almost 20 percent of the saturation moments. secondly, both the exchange bias field and the coercive field increase during the switching process, unlike that of the interface A. Thirdly, although the exchange bias field increases from 65 Oe to 140 Oe, the blocking temperature significantly decreases. The temperature dependance of the exchange bias and coercive field in two polarization states are summarized in figure 3.11 (c), which unambiguously reveal the different electric control behavior.

3.4 Mechanism and summary

The dramatically different magnetoelectric coupling effects can be understood in two steps. First of all let's take a look at the different magnetization modulation ratio, which is roughly 10 percent for interface A and much larger ($\sim$20 %) for interface B. Furthermore the two interfaces show similar dependance on the polarization direction, i.e. downwards polarization favors larger magnetization. The magnetization of LSMO strongly depends on the carrier density, which is the key concept in LSMO/FE devices [67]. The modulation of magnetization in BFO/LSMO observed in this work can also be explained in the same context if we include another degree of freedom, which is the charge transfer due to the different interface polar structure.

In the previous work of oxides FET devices, the charge carrier density of the electrode is usually assumed to be the nominal value in bulk. However it has also been shown that the charge transfer cannot be neglected in the heterostructure [108]. Therefore the interface carrier density might be very different from the bulk value.

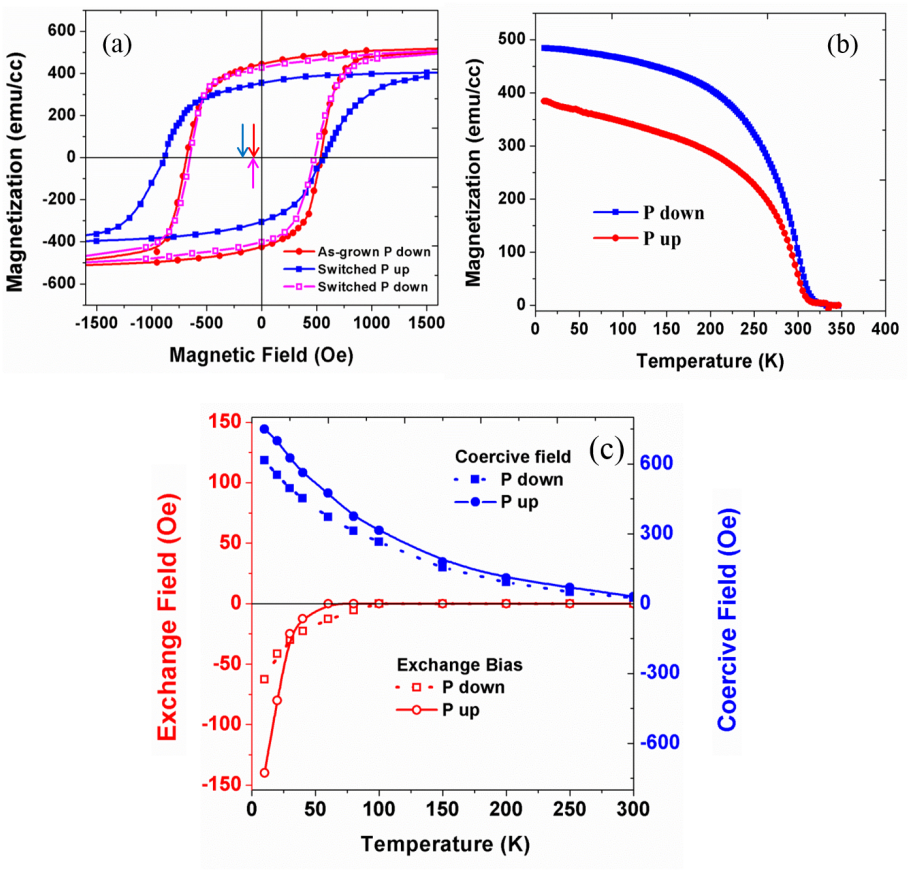

Figure 3.11: Magnetoelectric coupling of interface B. (a) Magnetic hysteresis of BFO/LSMO with interface B in different polarization states. (b) Magnetization versus temperatures of the different polarization states. (c) Temperature dependance of exchange bias and coercive field of interface B.

In BFO/LSMO, the two interfaces actually have opposite polar discontinuity and therefore the different charge transfer mechanism. Thus the carrier density would be different even without considering the polarization modulation. This effect is very important by considering the short screening length of LSMO in the field effects devices [115], which is just 1-2 unit cell. For BFO and LSMO, the nominal charge state of different sub-layers are as following: BiO (+1), FeO_2 (-1), $La_{0.7}Sr_{0.3}O$ (+0.7) and MnO_2 (-0.7). Therefore within the framework of the polar discontinuity model, the sheet charge density at the interface A (Figure 3.12 (a)) is assigned to be +0.7e/0.7e/+1e/-1e, which results in a nominal positive charge of +0.15e. On the other hand, the other interface has the nominal negative charge of -0.15e. The different polar structure possibly leads to two effects: the preferred polarization direction in as-grown state and the charge redistribution, both of which compensate the

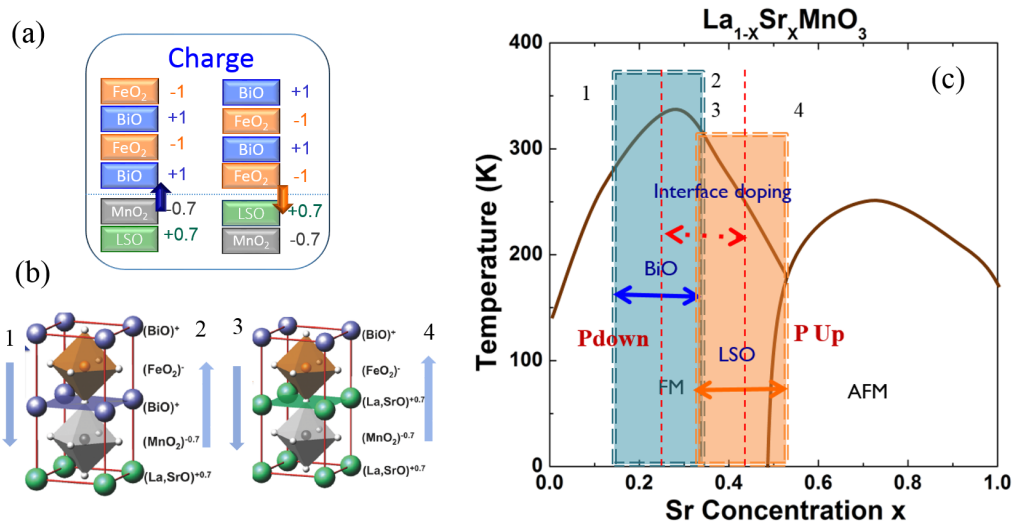

Figure 3.12: Schematic of charge modulation at the two BFO/LSMO interfaces. (a) Charge transfer at the BFO/LSMO interface due to the interface polar discontinuity. (b) Schematic of four states: two polarization states plus two interface states. (c) Schematic of charge modulation region by the combined effects of interface polar structure and ferroelectric polarization.

extra interface charge. The charge redistribution, or we can call it interface doping, is schematically shown in figure 3.12 (c) by the two dash red line. The magnitude is $\sim$ 0.3e, comparable to the modulation range caused by the ferroelectric polarization. Polar structure of interface A leads to a electron doped state and that of interface B leads to a hole doped state as shown in the figure 3.12 (c).

The combination of the interface polar structure and ferroelectric polarization leads to total 4 different states as shown in figure 3.12 (b): interface A plus upwards polarization (state 1), interface A plus downwards polarization (state 2), interface B plus upwards polarization (state 3) and interface B plus downwards polarization (state 4). The state 2 and 3 are the as-grown states. Due to the interface polar effects discussed above, the charge modulation region is actually different for the two interfaces (blue for interface A and red for interface B). In state 1 and 4, the two effects act constructively while in state 2 and 3 they cancel with each other. This model is consistent with the observation of magnetization modulation: (a), the modulation region of interface A is in inside the ferromagnetic phase while that of interface B moves towards the ferromagnetic/antiferromagnetic (FM/AF) phase boundary. Therefore the ratio of change is larger for the heterostructure with interface B. (b) the effective doping ratio of state 2 and 3 are the same due to the cancellation and therefore the suturation magnetization is similar.

Next we discuss the modulation of exchange bias coupling. The behavior of exchange bias coupling in the two interfaces are quite different. A close analysis of the temperature dependance provides more insights to understand the mechanism. Lots of experimental and theoretical works have been done to understand the phenomena, which is of great technical importance [72, 104, 105]. Based these previous works, a simplified heisenberg model can be used to cover the basic mechanism in the FM/AF bilayer system:

$$H_{ex} = \eta \frac{E_{eff}}{a^2 M_{LSMO} t_{LSMO}} \exp\left(\frac{-k_b T}{E_{eff}}\right) \tag{3.1}$$

η is the fraction of pin sites, E_{eff} is the effective coupling strength between the ferromagnetic and antiferromagnetic spins across the interface, a is the lattice parameter and M and t are the magnetization and thickness of ferromagnetic LSMO layer. In this equation, two terms determine the magnitude of exchange bias. The first one is the number of pin sites, which can be related to the uncompensated spins at the magnetic domain walls or surface terrace in BFO. The second one is the intrinsic exchange coupling strength across the interface. The last term in the equation describes the influence of thermal fluctuations. In this model, the antiferromagnetic moments are assumed unchanged due to the large anisotropy energy. The fitting parameters are shown in the 3.1 for the four states.

The number of pin sites η shows a similar value for state 1-3 and drastically increases in state 4, which accounts for the significant increase of exchange bias field but not the blocking temperature in state 4. Actually it remains an puzzle to fully understand the location of pin sites of BFO, which is a G-type AF with a compensated spin structure at the surface. Previous work pointed out the important role of domain walls of BFO [26]. Also the surface height terrace could contribute to the pin sites. However the roughness can be ruled out in this case since the identical samples are used and the difference is simply due to ferroelectric switch. Furthermore the reversible modulation rules out the damage of interface during the switching process. Despite of the important role of domain walls proved before, it cannot entirely explain the modulation effects in the state 4 because all of the four states show similar four variants 71 degree domain structures.

Actually the modulation of pin sites show a similar behavior as the magnetization of LSMO discussed above. The state 4, which shows the largest depression of magnetization, has the largest number of pin sites. The important role of antiferromagnetically coupled Mn moments have been discussed previously [101]. Therefore it is likely that the AF coupled Mn spins at the interface serves as a bridge to pin the FM LSMO moments and the number of the AF coupled Mn spins, determined by the charge carrier density, scales to the number of pin sites. In terms of the coupling strength, both state 2 and 3 show similar coupling strength, which reduces in both state 1 and 4. The effective coupling strength is determined by the coupling mechanism between the Fe-O-Mn and first Mn-O-Mn [101]. Therefore the reduction of effective coupling strength in state 1 and 4 could be caused by different mechanisms.

	η	E_{eff}
State 1	0.6 %	1.5 meV
State 2	0.7 %	2.6 meV
State 3	0.65 %	2.7 meV
State 4	3 %	1.3 meV

Table 3.1: Fitting parameters of exchange bias coupling of BFO/LSMO. The temperature dependance of exchange bias field is fitted by the simplified heisenberg model. η is the number fraction of pin sites in the system and E_{eff} is the effective coupling strength.

In state 1 the interface is heavily electron doped as shown in figure 3.3 and therefore the proposed orbital reconstruction [101] becomes weaker, which could effectively reduce the coupling strength. On the other hand in states 4, the interface is heavily hole doped and more Mn-O-Mn coupling becomes antiferromagnetic, which could thus reduce the effective strength by taking into account the low ordering temperature of AF manganite.

In summary, interface polar structure (the atomic stacking sequence) is an important factor to determine the exchange bias coupling and the magnetoelectric effects in oxides heterostructures. The key concept of this interface engineering is the extra charge transfer caused by the polar discontinuity, which should be taken into accounts as another degree of freedom to design novel magnetoelectric devices.

Chapter 4

Tuning the competition between ferromagnetism and antiferromagnetism in a half-doped manganite

4.1 Motivation: competition of magnetic orderings at the phase boundary

The results presented in last chapter demonstrate that the extra charge transfer at the interface, which is controlled by the atomic stacking sequence, significantly affects the magnetoelectric coupling. The largest modulation ratio ($\sim$20%) of magnetization is found in the heterostructure with interface B (MnO_2-LaSrO-FeO_2). Inspired by the results, an interesting question can be put forward naturally: What is the upper limit of the modulation ratio? Or in other words, can one reversibly switch an antiferromagnet (with no macroscopic magnetic moment) to a ferromagnet (with a macroscopically sensible moment) as shown in figure 4.1 (a)?

There are some logical criteria that can be used as design rules to accomplish the goal. First of all, it is desirable in these materials that ferromagnetism (FM) strongly competes with antiferromagnetic (AF) ordering. Moreover, the competition should depend on external fields, such as electric/magnetic field, chemical potential or strain [37, 44, 116]. One ideal candidate is the half-doped manganite, exemplified by $La_{0.5}Ca_{0.5}MnO_3$ (LCMO) or $La_{0.5}Sr_{0.5}MnO_3$ (abbreviated as LSMO0.5 to differentiate from $La_{0.7}Sr_{0.3}MnO_3$). According to the typical phase diagram of manganite [44] (see figure 3.3), 50 % doping is usually the phase boundary between the FM and AF magnetic ordering. However there are different kinds of half-doped manganite systems such as the wide bandwidth $La_{0.5}Sr_{0.5}MnO_3$ (LSMO), the medium bandwidth $La_{0.5}Ca_{0.5}MnO_3$ (LCMO) and the narrow bandwidth $Pr_{0.5}Ca_{0.5}MnO_3$ (PCMO) [117].

Then the next question is to choose the right candidates. The wide bandwidth LSMO0.5 can only be synthesized under stringent and well-controlled growth conditions. In bulk, the coexistence of a FM phase and an A-type orbitally ordered AF phase is stabilized over a wide temperature range below 200K [118, 119]. The medium bandwidth LCMO, on the other hand, can be easily synthesized under ambient conditions. Charge ordering, FM and AF phases have all been reported at different temperatures below 300K [120, 121] (see figure 4.1 (b)). Finally the narrow bandwidth PCMO doesn't show ferromagnetism during the whole temperature range due to the small transfer integer. Therefore both LSMO0.5 and LCMO meet the criteria of phase competition. LCMO is used in this work due to the relatively easy fabrication of high quality thin film.

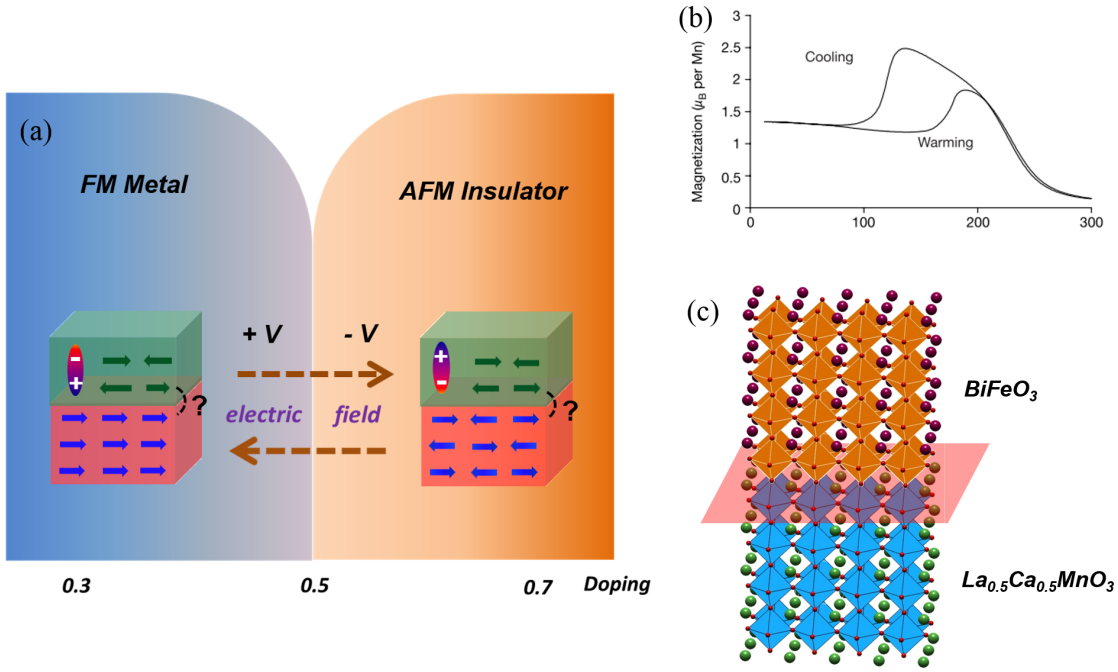

Figure 4.1: Schematic of electrical control of FM/AF transition and the model system LCMO. (a) Schematic of electrical control of FM/AF transition: the half-doped manganite at the magnetic phase boundary is a promising candidate. Multiferroic materials such of BFO provide an additional freedom due to the interface coupling effect. (b) FM/AF transition of LCMO. (c) Schematic of the model system BFO/LCMO used in this chapter. (b) is adapted from [120]

Bulk LCMO undergoes two successive transitions: paramagnetic to FM transition (T_c=270K) followed by FM to AF transition (T_N=160K) as shown in figure 4.1 (b). Moreover, the transition is controllable by the magnetic field. These facts clearly characterize the strong competition between FM and AF order in LCMO. The model

system we study in this chapter is BFO/LCMO heterostructure as shown in figure 4.1 (c). The first question to explore is how large the magnetization modulation ratio is. Moreover since the multiferroic BFO is used instead of regular ferroelectric, it is equally intriguing to study the change of AF ordering of BFO at the interface. The majority of results shown in this chapter has been published as [122].

4.2 Heterostructure deposition and ferroelectric characterization

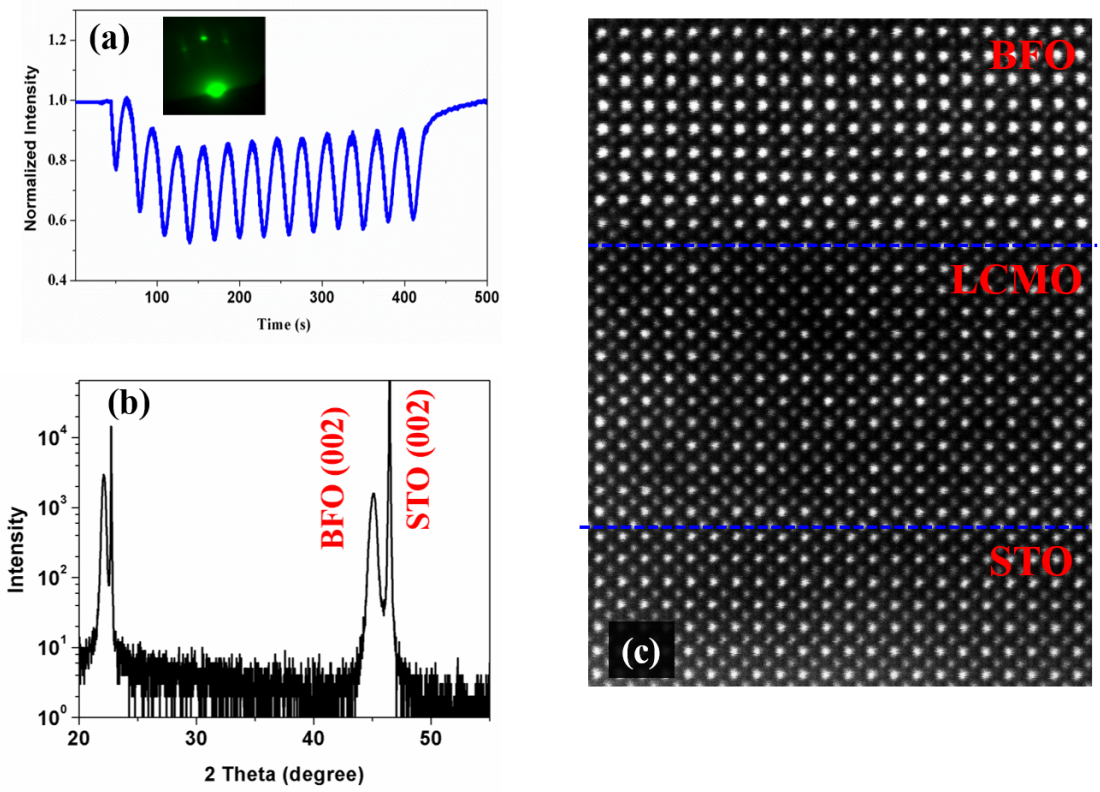

Figure 4.2: Structure characterization of BFO/LCMO heterostructure. (a) RHEED oscillations demonstrate the layer-by-layer growth mode of LCMO on STO (001) substrate. (b) X-ray diffraction of a BFO(100nm)/LCMO(5nm)/STO heterostructure. (c) STEM images of BFO/LCMO heterostructure.

Single crystal low-miscut $SrTiO_3$ is chosen as the substrate due to small lattice mismatch to both BFO and LCMO. Before growth, the substrate is wet-etched by buffered HF acid, followed by a thermal annealing process, which forms the TiO_2 terminated atomically flat surface. LCMO and BFO were grown epitaxially on STO

substrate from the chemical stoichiometric ceramic target at the laser density of 1.5J/cm^2. The repetition rate is 1Hz and 3Hz for LCMO and BFO respectively. During the growth, RHEED was used to monitor the growth layer by layer (Figure 4.2 (a)), which yields an atomically flat interface (see figure 4.3 (a)). After growth, the sample was cooled down to room temperature at 760 mTorr oxygen ambient at the rate of 5^{0}C/min.

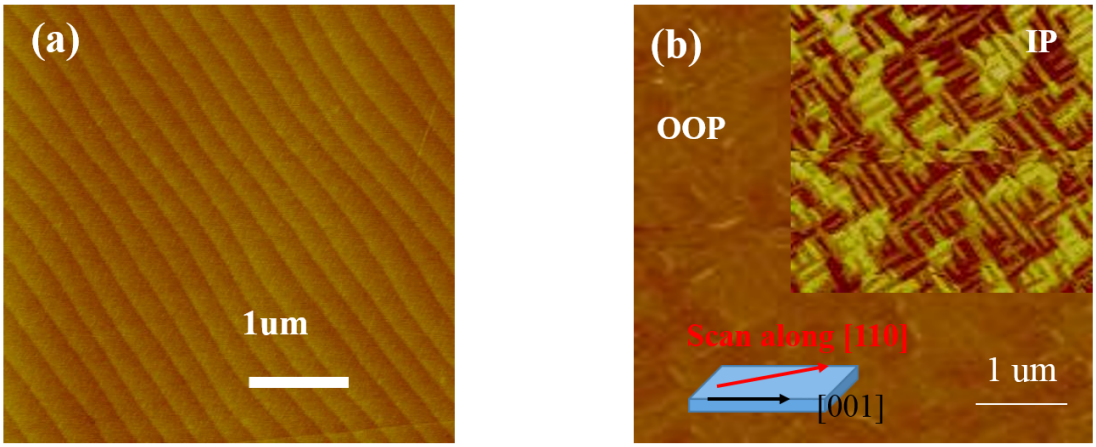

Figure 4.3: Topology and ferroelectric domains of BFO/LCMO heterostructure. (a) AFM image of the LCMO thin film, which shows the similar surface topology as the substrate. (b) OOP and IP PFM of BFO/LCMO heterostructure scanned along the crystal [110] direction.

Structural characterization with x-ray diffraction (Figure 4.2 (b)) reveals the single phase, fully epitaxial layers of BFO and LCMO, which were in-plane strained to the STO substrates. The atomic configuration at the interface was studied with high angle annular dark field (HAADF) imaging in scanning transmission electron microscopy (STEM) mode. Figure 4.2 (c) shows a typical HAADF image of such a LCMO/BFO heterostructure. The clear contrast indicates an atomically sharp interface between the LCMO and BFO. The ferroelectric domain structures were studied by piezoelectric force microscopy (PFM) and the scanning direction is along [110] of substrate (4.3 (b)). Figure 4.3 (b) shows the out-of-plane (OOP) and in-plane (IP, inset) PFM images of a typical BFO/LCMO heterostructure. The IP polarization shows the presence of nice stripe-like domains (71^0 domains), consistent with previous studies.

The heterostructure above (called as structure H1) consists of LCMO on STO and then deposited with 100nm BFO, which shows the stable ferroelectricity with minimum leakage problem. Therefore it can be used to check the modulation of magnetization by using the same method as BFO/LSMO discussed in last chapter. As pointed out in the third section of chapter 2, synchrotron based X-ray absorption

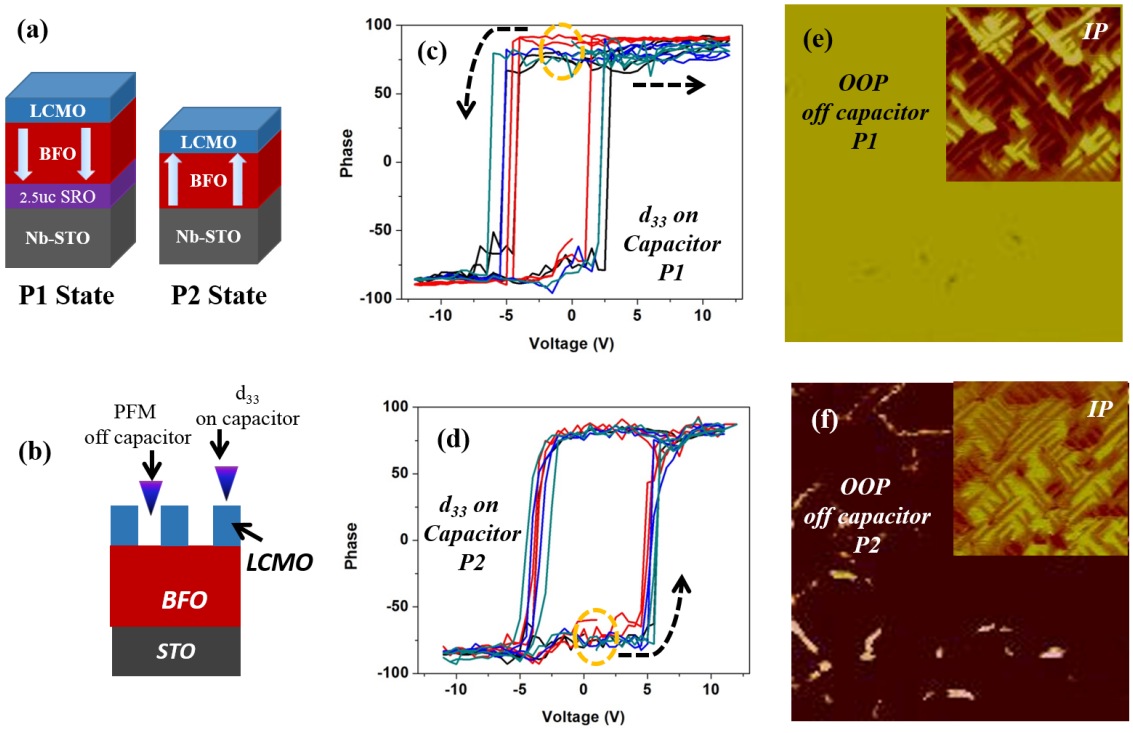

Figure 4.4: Ferroelectric characterization of the reversed structure. (a) Schematic of two polarization states in the reversed structure (H2) controlled by interface. (b) Capacitor structure for PFM and piezoresponse hysteresis study of the reversed structure (H2). (c), (d) Piezoresponse hysteresis (d_{33} loop) of P1 and P2 state on capacitor. (e), (f) PFM image of P1 and P2 state off capacitors.

technique (XAS,XMCD and XLD) is a very powerful tool to study the electronic and magnetic structure of the heterointerface. However due to the limited probing depth ($\sim$ 5-10 nm) of the surface sensitive TEY mode [123, 124], the H1 heterostructure is not suitable to study the interface. Therefore, the reversed heterostructure (called as heterostructure H2) of the BFO (100nm, bottom) and LCMO (5nm/2nm, top) were fabricated. In H2 structure, the TEY signal comes from the entire LCMO layer and the interfacial BFO.

The key point to use the reversed H2 structure for X-ray based absorption technique is to stabilize the two ferroelectric polarization states in the as-grown state. Previous study has demonstrated that the FE polarization can be controlled through the electrostatic boundary condition in the as-grown state [111] and therefore we can fabricate the H2 structure with different ferroelectric polarization state as shown in figure 4.4 (a). When BFO is deposited on Nb-STO directly, OOP polarization is upwards. On the other hand, OOP polarization is downwards if two unit cells of SrRuO3 are deposited first. In order to be consistent in H1 and H2 structures,

the out-of-plane (OOP) polarization points away from the BFO/LCMO interface is defined as P1 state and the opposite case is defined as P2 state.

The validity of P1 and P2 state in H2 structure was also confirmed by d_{33} hysteresis loop and PFM. To study the ferroelectric polarization, capacitor structure was made by ion milling etch of LCMO top layer as shown schematically in figure 4.4 (b). The piezoresponse hysteresis (d_{33}) was measured by using the LCMO top electrode and confirms the polarization state. The initial phase (positive for P1, figure 4.4 (c), negative for P2, figure 4.4 (d), marked by the yellow circle) confirms the out-of-plane (OOP) polarization direction in the as-grown state. The shift of hysteresis (negative for P1, positive for P2) is also consistent with the model of interfacial electrostatic boundary. Furthermore PFM taken directly on BFO (the region where LCMO is etched) also confirms the results. The light contrast in figure 4.4 (e) suggests the polarization is downwards (P1 state, away from LCMO/BFO interface) while the dark contrast in figure 4.4 (f) suggests upwards polarization (P2 state, towards LCMO/BFO interface).

4.3 Electric control of AF/FM phase transition

First we studied the electric field control of AF/FM transition in the H1 structure by using the similar method discussed in last chapter. A metal-probe set up with a 50 μm tip was used to switch the polarization of the whole sample. The dark contrast of the out-of-plane (OOP) image indicates that polarization points away from the interface (P1 state, Figure 4.5 (a)) and the light contrast corresponds to the polarization towards the interface (P2 state, Figure 4.5 (b)). PFM taken at multiple randomly selected regions confirms a nearly 100% polarization control.

By virtue of the well-controlled FE polarization, we measured the resulting change of the macroscopic magnetization. In Figure 4.6, the black, red and blue curve shows the magnetization of the heterostructure (H1,figure 4.5 (a)) in the as-grown state (P1), switched to the opposite state (P2) by positive voltage and switched back to the original state (P1) by negative voltage. Reference data from a sample with 100 nm BFO on STO, which accounts for the diamagnetic signal of substrate and the small bulk canted moments of BFO [125, 126], is subtracted from the raw data. The temperature dependence of magnetization in P1 state shows a negligibly small moment. On the other hand, magnetization of P2 state shows a macroscopically sensible moment. The saturation-like behavior between 100K and 200K suggests the FM clusters or canted AF ordering [127, 128]. Furthermore, the data clearly shows that the modulation effect is reversible through FE switch.

In order to identify the contribution from LCMO and BFO respectively, we utilized the element-specific XAS and XMCD to study Fe and Mn *L*-edge in H2 structure. Figure 4.7 (b)-(e) display the XAS and XMCD at the Mn and Fe *L*-edge at 20K with an applied field of 0.5T. The XMCD of $\sim$ 2.6 % at Mn *L*-edge is clearly observed

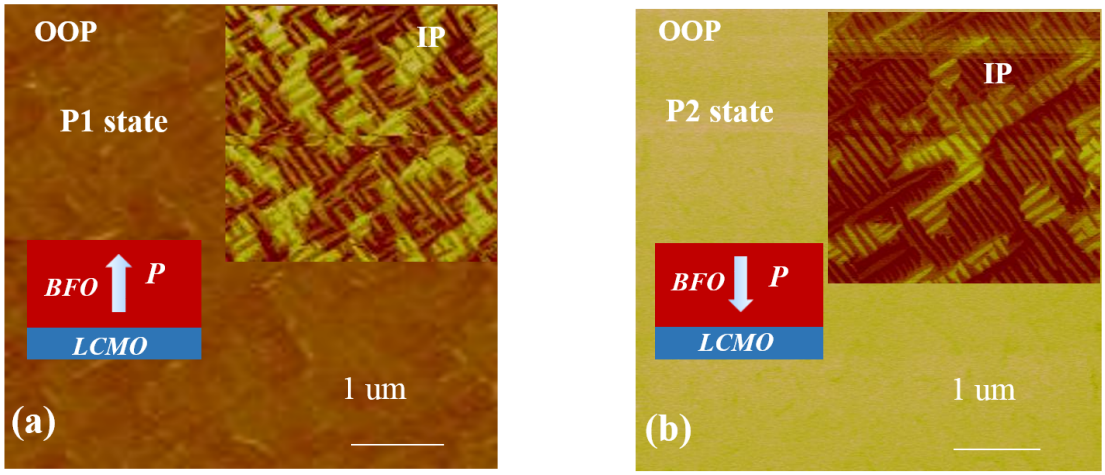

Figure 4.5: PFM image of BFO/LCMO after macroscopic switch. (a), (b) PFM of P1, P2 state in structure H1. The polarization is switched macroscopically by the probe set-up. The OOP confirms a nearly 100% switch. The IP shows similar four variants domains.

in P2 state (figure 4.7 (b)), which is confirmed in multiple samples (figure 4.7 (c)). However, no clear XMCD is observed in the P1 state. In addition, XMCD of Fe L-edge also reveals a significant change($\sim$ 1 %) in P2 state and negligible in P1 state, figure 4.7(d) and (e). The opposite sign of XMCD signifies an AF coupling between Fe and Mn across the interface. The temperature dependence of XMCD is summarized in Figure 4.6 along with magnetization measured by SQUID.

The magnitude of the magnetization can be quantitatively estimated by the XMCD spin sum-rule [129] to obtain both spin (4.1) and orbital momentum (4.2). Here m_{spin} and m_{orb} are spin and orbital magnetic moments in unit of μ_B/atom, respectively, and n_{3d} is the 3d electron occupation number of the specific transition metal atom. The L_3 and L_2 denote the integration range. $< T_z >$ is the expectation value of the magnetic dipole operator and $< S_z >$ is equal to half of m_{spin} in Hartree atomic units. Since the $\frac{7<T_z>}{2<S_z>}$ is very small in manganite and ferrite system [129], it could be neglected in the calculation. μ_+ and μ_- are the X-ray absorption with the left and right circular polarized light.

$$m_{spin} = -\frac{6\int_{L_3}(\mu_+ - \mu_-)d\omega - 4\int_{L_3+L_2}(\mu_+ - \mu_-)d\omega}{\int_{L_3+L_2}(\mu_+ + \mu_-)d\omega}(10 - n_{3d})(1 + \frac{7 < T_z >}{2 < S_z >}) \quad (4.1)$$

$$m_{orb} = -\frac{4\int_{L_3+L_2}(\mu_+ - \mu_-)d\omega}{3\int_{L_3+L_2}(\mu_+ + \mu_-)d\omega} \quad (4.2)$$

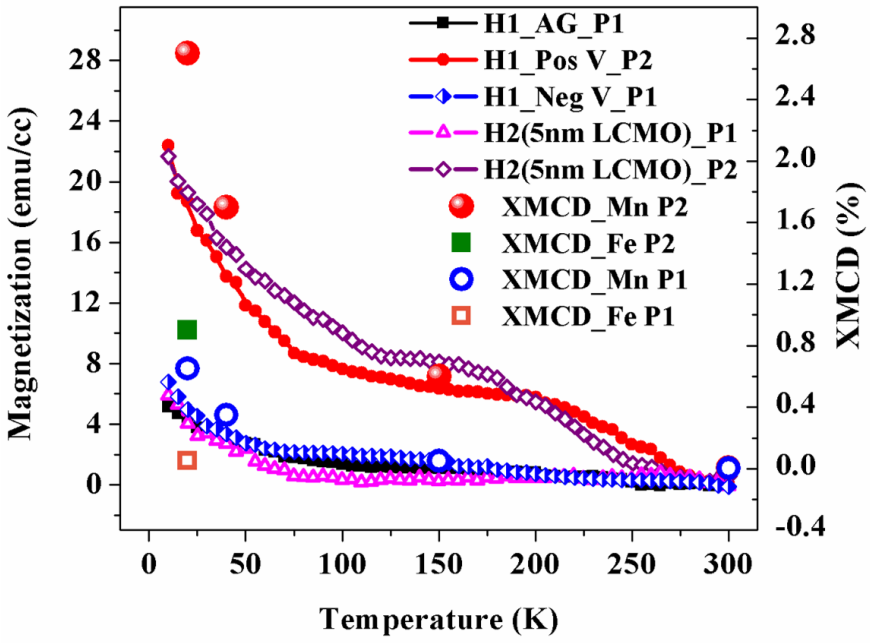

Figure 4.6: Temperature dependence of magnetization of P1 and P2 states. The curves show the data taken with magnetometer and the dots are calculated with spin sum-rule of XMCD.

The photon incident angle (30^0) and the degree of circular polarization (90%) are considered. Taking the integration and putting the numbers into the equation, the spin and orbital moment of Mn are estimated to be 0.24 b/Mn and 0.015 b/Mn. The calculated spin and orbital moment of Fe are roughly 0.1 b/Fe and 0.018 b/Fe at 20K. Since the TEY mode is a surface sensitive technique and the intensity decays exponentially from the surface, the magnetic moments at the interface could be larger than the average value. Furthermore, the XMCD of H2 structure with 2nm LCMO ($\sim$4%, see figure 4.7 (c)) is larger than that of H2 structure with 5nm LCMO (figure 4.7 (b) and (c)), which again reveals that the enhanced moments are mainly from interface. The temperature dependance of magnetization calculated from XMCD spectra is summarized in figure 4.6 (c) along with the magnetization measured from SQUID. Considering the AF coupling of Fe and Mn across interface, the calculated value is in reasonable agreement with the SQUID magnetometry. Therefore the the measurements on both structure H1 and H2 consistently reveals the modulation of AF/FM phase transition in LCMO, which is controlled by electric field. Additionally the canting moment of BFO is significantly changed.

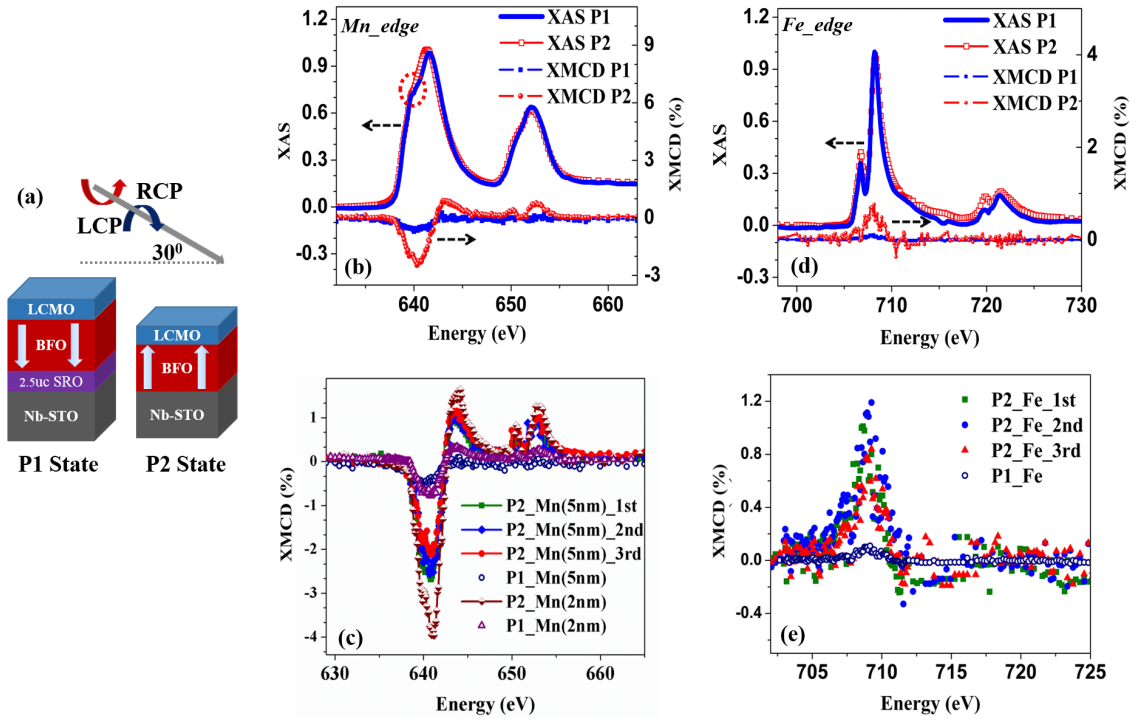

Figure 4.7: XMCD of Mn and Fe L-edge of P1 and P2 states. (a) Schematic of XMCD experiment configuration. (b), (d) The XAS and XMCD spectra of Mn, Fe $L_{2,3}$ edge in P1 and P2 states. (c), (e) Multiple repeats of XMCD of Mn, Fe $L_{2,3}$ edge.

4.4 Mechanism of AF/FM transition tuned by electric field

In order to gain further insight, we studied the microscopic magnetic coupling across the Fe-O-Mn bond. Figure 4.8 (a) shows the XAS of the oxygen K edge for the LCMO/BFO heterostructure. In contrast with the higher energy region (Bi-La-Ca s, p characters/Fe-Mn s, p characters), the lower energy spectrum reveals the information of d orbital of LCMO and interfacial BFO. The feature F1 corresponds to the mixture of Fe (t_{2g} orbital) and Mn (t_{2g} and e_g orbital) states, while the F2 is related to only the e_g orbital of BFO. Figure 4.8 (b) shows the XAS of oxygen K edge by using linear polarized x-ray at different temperatures (similar for P1 and P2). Previous study [101] observed that F2 peak shifts to lower energy as the temperature decreases in LSMO/BFO when the x-ray polarization is out-of-plane, which is explained as the hybridization of Mn and Fe $3z^2$-r^2 orbital at the interface. However this shift is absent in Figure 4.8 (b). In contrast to LSMO, LCMO is under stronger tensile strain from the substrate, resulting in the stabilization of x^2-y^2 orbital compared with $3z^2$-r^2, which is supported by the negative sign of XLD (I(a)-I(c)) at Mn L-edge [130] (Figure

4.8 (c)). Therefore, the orbital reconstruction proposed for BFO/LSMO interface is not expected here. Instead, we speculate that the main magnetic coupling is derived from the AF SE between Fe and Mn t_{2g} spins.

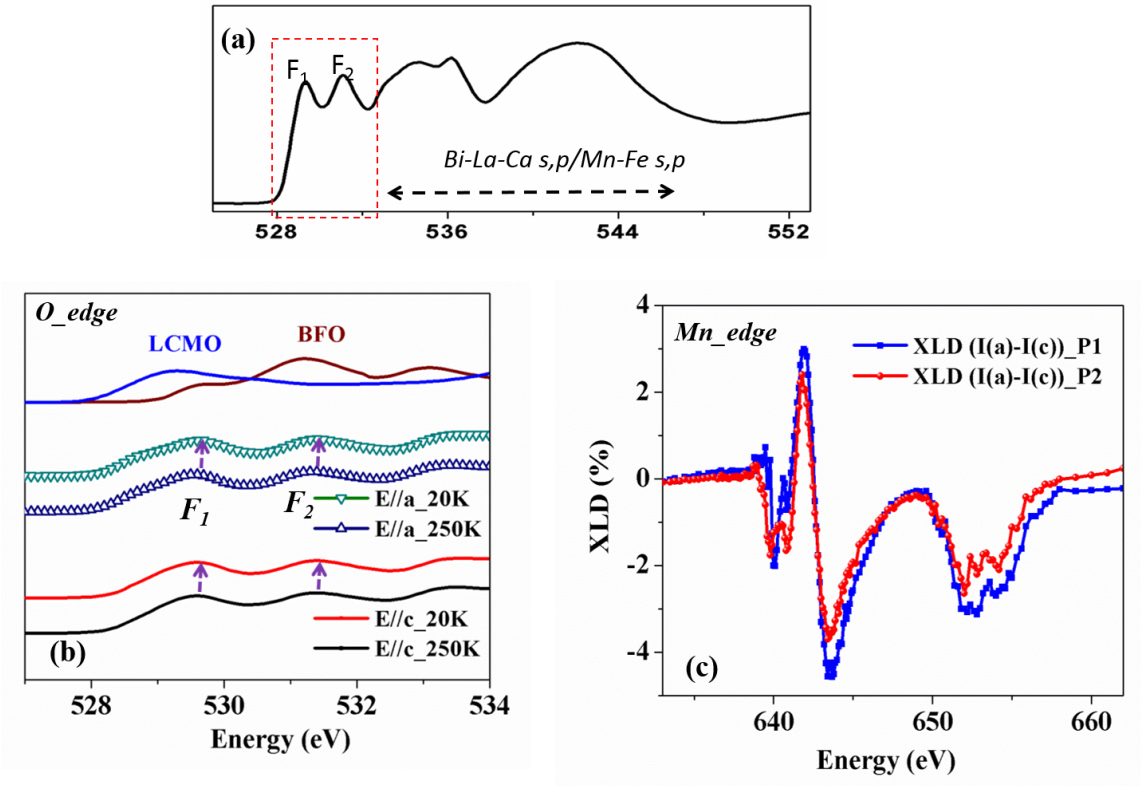

Figure 4.8: XLD of Mn and O edge of P1 and P2 states. (a) XAS of oxygen K-edge in LCMO/BFO heterostructure. (b) XAS of oxygen K-edge (similar in P1 and P2 state) by using the linear polarized x-ray with polarization in-plane and out-of-plane. (c) XLD of Mn $L_{2,3}$ edge in P1 and P2 states.

Based on the element-specific technique above, we found that the modulation effect is derived from both LCMO and BFO. We speculate that the FE polarization is likely to favor the FM (AF) coupling in LCMO in P2 (P1) state due to the change of d-electron density. The varied magnetic coupling in LCMO then leads to the change of canted moments in the interfacial BFO due to the magnetic coupling. Besides the carrier modulation, strain effect should also be considered. The strain controlled nonvolatile magnetoelectric coupling requires the change of FE domain and thus the in-plane lattice constant [69]. However both P1 and P2 states in this study show similar four variants domains, which suggests that strain is not likely the main reason for the observed nonvolatile magnetization modulation.

To test the electronic origin, we performe a close examination on the XAS spectra

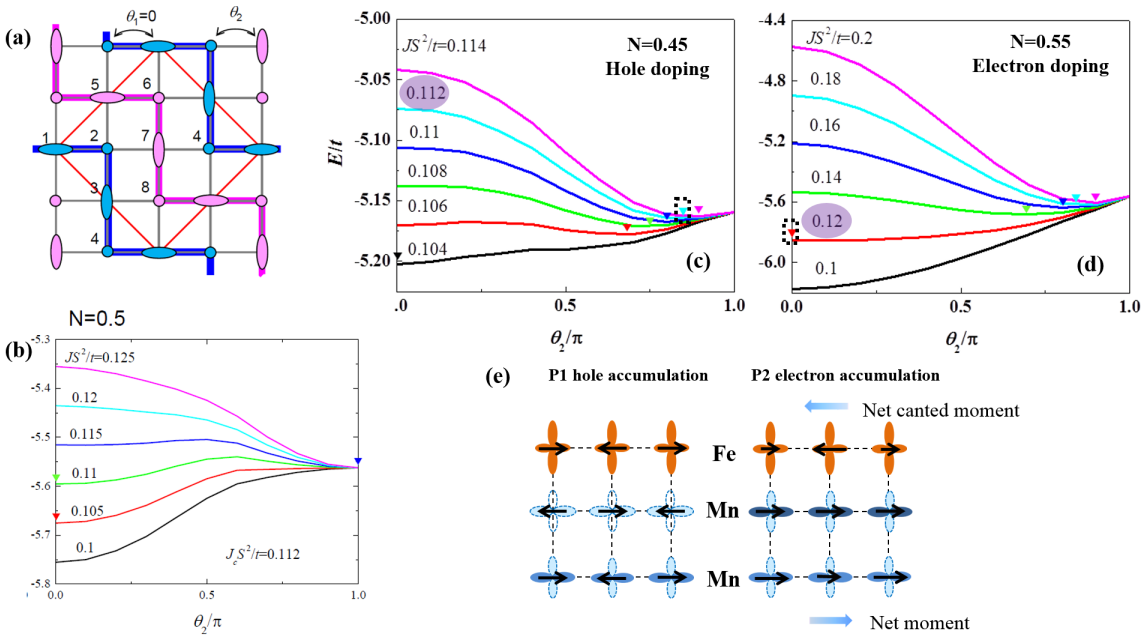

Figure 4.9: Mean-field theory calculations on the electron density dependance of magnetic ordering in LCMO. (a) The two-dimensional model of mean-field theory: the model considers DE (t) and SE (JS2) coupling; 1 is fixed as 0 and 2 is a variable; the single parameter 2 can reproduce both the FM and CE-AF. (b),(c), (d) The energy profile at different JS2/t when N=0.5, 0.45, 0.55. (e) Schematic of the electron density and spin structure at the heterointerfaces (The dark/light contrast suggests the electron accumulation/depletion).

of Mn L-edge in the two polarization states (Figure 4.7 (b)). Although the XAS of Mn L edge is similar to a +3/+4 mixed valence in both cases, there are a few clear differences between the two states. In particular, the XAS spectrum of P1 state (blue line) shows an enhanced shoulder-like feature on the low-energy side of the main peak of the L_3 edge, which is distinctly absent in the spectrum of P2 state (red line with square symbol). Besides, the main absorption peak shifts to the higher energy level in P1 state comparing with the P2 state by roughly 0.2 eV. Previous studies on manganite revealed that both the peak position and the line shape of Mn L edge XAS are highly sensitive to the Mn valence state [131]. It has been demonstrated that the peak energy increases for higher oxidation state of Mn, and the shoulder-like multiplet structure of the L_3 edge is the fingerprint of Mn^{4+} state. Moreover, the change of L_3/L_2 ratio follows the trend demonstrated in previous studies [132], which suggests higher oxidation state in P1 state. Therefore, by taking all these observations into account, we can reach a conclusion that the valence state of Mn changes due to the carrier modulation by the FE polarization. The valence state of

P1 is closer to the Mn^{4+}, while the valence state of P2 is driven toward the Mn^{3+}. Based on the energy shift [133], we estimate an average change of Mn valence to be ∼0.1/Mn, consistent with the calculated average change of charge of $0.11e$/Mn, assuming $2P_s$=130 μC/cm^2 [134].

To quantify the relationship between the densities of e_g electrons and the magnetic interactions in LCMO, we perform mean-field theory calculations. Here we consider a 2-dimensional model. In the 2-dimensional model, double-exchange (DE) interaction with e_g orbitals and superexchange (SE) interaction between neighboring t_{2g} spins are considered. For simplicity, electron-lattice distortion is not considered. Figure 4.9 (a) shows the spin configuration in our model. θ_1 is fixed as 0, which represents the ferromagnetic interaction in the zigzag chain in CE-type antiferromagnetic ordering (CE-AF) [44]. θ_2 is the relative angle between neighboring spins across the zigzag chain. It is a variable in our model and the single parameter can cover both the FM state and CE-AF. The relative strength between SE coupling (JS2) and DE (t) is represented by the parameter JS2/t. For different JS2/t, the local minimum of energy determines the relative angle between the neighboring spins across the chain (2). 2=0/ corresponds to the FM/CE-AF spins arrangement.vWe estimate the critical value of JS^2/t to be slightly larger than 0.112 (figure 4.9 (b)), which reproduces the CE-AF ground state with orbital ordering for N=0.5 [121], consistent with previous studies [135–137].

Figure figure 4.9 (c) and figure 4.9 (d) present the results for hole doping (N=0.45) and electron doping (N=0.55) respectively. The results show that canting of antiferromagnetically coupled neighboring moments is possible for both electron and hole doping. However the canting is stronger in the electron-doping than the hole-doping side. The results suggest that a FM ordering is energetically more favorable at the critical value of JS^2/t when electrons are accumulated in LCMO, which is in accordance with the macroscopic moments observed by both the magnetometry and XMCD in P2 state. On the other hand, the AF coupling is energetically more favorable in the hole-doping side. Based on these considerations, we propose a mechanism for the electrical control of magnetic coupling at BFO/LCMO heterointerface as shown schematically in figure 4.9 (e). The FM interaction in LCMO is enhanced by electron doping. The magnetic coupling across the heterointerface then leads to the larger canted moments in BFO. Oppositely both LCMO and BFO remain AF in the hole-doping side. Our microscopic mechanism consistently explains the modulated competition between FM and AF instability by switching FE polarization.

4.5 Further discussion and implication

Although the electric field control of AF/FM phase transition is clearly demonstrated by the results above, a few more implications are worthy of further discussions. Bulk LCMO shows a significant change of magnetization between FM (∼2.6 μ_B/Mn)

and AF (less than ∼1 μ_B/Mn) [120]. It is accompanied by a metal-insulator transition with several orders of magnitude modulation of resistance [138,139]. However in the LCMO/BFO macrostructure, magnetization (∼0.2 μ_B/Mn on average) is far less than the saturation value of bulk. Furthermore no clear metal-insulator transition is observed in this system in both polarization states. Figure 4.10 shows the modulation of LCMO resistance in the field-effect-transistor (FET) geometry, which is shown schematically in figure 4.10 (a). Figure 4.10 (b) is the ferroelectric hysteresis of BFO in the FET device, which is reversible with minimal leakage current. LCMO channel shows a clear resistance modulation controlled by ferroelectric polarization. The inset of figure 4.10 (c) shows the resistance of LCMO at 170K under a successive polarization switch sequence. However the temperature dependance reveals similar semiconducting behavior in both states with no clear sign of metal-insulator transition.

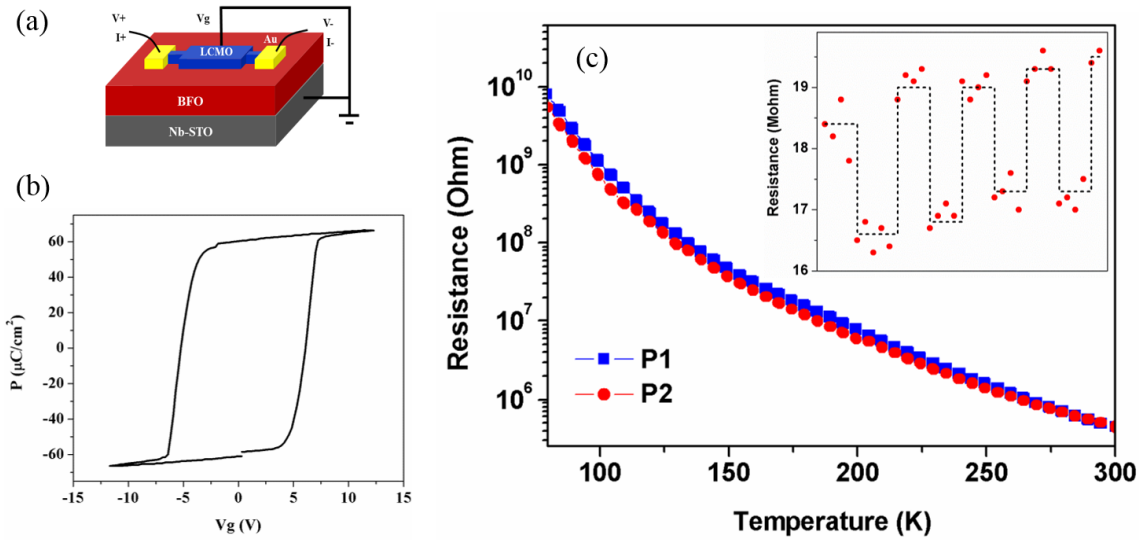

Figure 4.10: Field effect of BFO/LCMO heterostrucure. (a) Schematic of the field-effect-transistor (FET) devices. (b) Ferroelectric hysteresis of BFO in the FET device. (c) Temperature dependance of LCMO channel resistance in two polarizations states, the inset shows the resistance modulation by successive ferroelectric polarization switch sequence.

So one question can be raised: What is the limitation of the AF/FM phase transition in this heterostructure geometry? One natural answer is the screening length of manganite in the FET device geometry, which is determined by the Thomas-Fermi screening and inversely propositional to the density of states at fermi level for metal and semiconductors. As for insulator, other mechanisms would play a role, such the defects [63]. Screening length determines the thickness of the active region of LCMO. And thickness can unambiguously control the magnetic properties. For example the

critical thickness for stable FM ordering in LSMO is found to be 4 unit cells [140]. For most wide bandwidth manganites such as metallic LSMO, the screening length is about 1-2 unit cells [141]. However the resistance of LCMO is several order magnitude higher than LSMO and shows a semiconducting temperature dependance. Therefore a much larger screening length would be expected and defects might also play a role here. Therefore the screening mechanism of the half-doped system, especially those with high resistance, definitely needs further careful investigations.

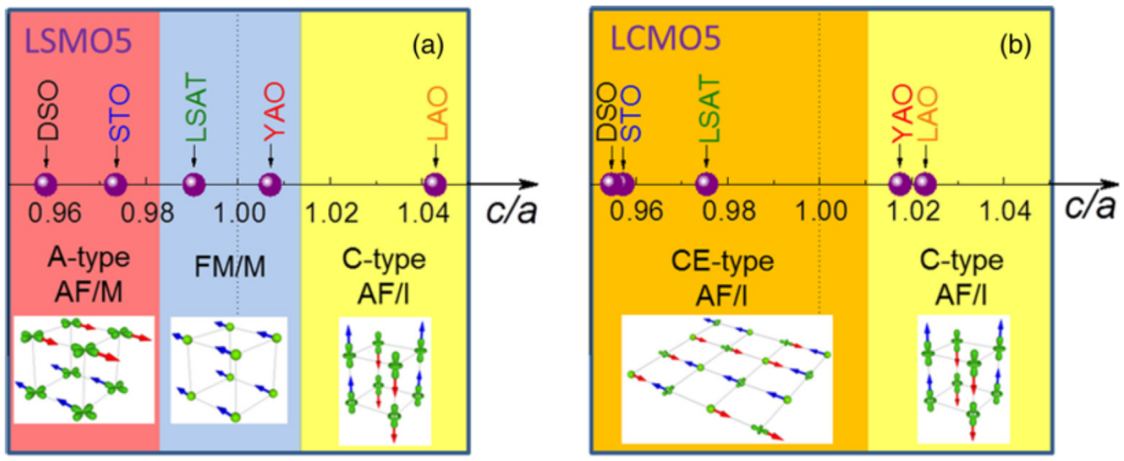

Figure 4.11: Experimentally obtained slice of the phase diagram of $La_{0.5}Sr_{0.5}MnO_3$ (a) and $La_{0.5}Ca_{0.5}MnO_3$ (b) in the plane of c/a. Adapted from [142].

Furthermore the role of epitaxial strain shouldn't be neglected. According to the design rule we propose at the beginning of this chapter, a material that is at the phase boundary of different magnetic orderings is the promising candidate. However the search of the best candidate is based on the bulk phase diagram, which might not be very accurate for thin film because the epitaxial strain is definitely another important parameter. Actually another work published later on revealed the strain effects on the magnetic phase boundary [142]. Figure 4.11 shows the phase diagram of half doped manganite as a function of epitaxial strain. It is clearly shown that strain determines the magnetic ground state even though the chemical composition is the same. As for LCMO shown in Figure 4.11 (b), the ground state is AF for the whole spectra of strain. Therefore the phase diagram that includes strain is needed to search for the best candidate.

The discussion above points out the important role of strain and thickness. Despite of that, the modulation effect of LCMO on STO substrate is still applicable by clever structure design. Ferroelectric tunneling junction has been widely studied as the possible pure ferroelectric memory device [143]. In 2013 Yin et al. presented the results of a significantly enhanced electroresistance in a carefully designed ferroelectric tunneling junction device as shown in figure 4.12 (a). In the device a very

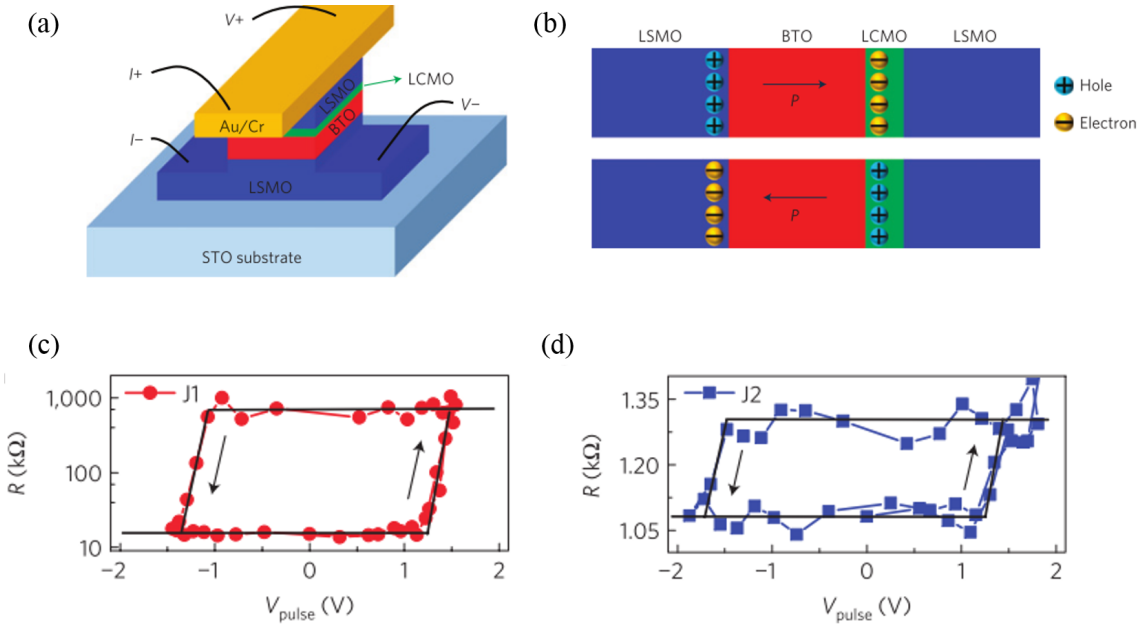

Figure 4.12: Large ferroelectric tunneling electroresistance with half-doped manganite modified interface. (a) Device schematic of the ferroelectric tunneling junctions. (b) Schematic of the working mechanism. (c) The large electroresistance of the LCMO modified tunneling junction. (d) Reference normal tunneling effect without LCMO. Adapted from [144].

thin layer of LCMO is inserted between the interface of $BaTiO_3$ and LSMO. Due to the phase transition of LCMO controlled by ferroelectric polarization switch, the electroresistance is several orders of magnitude higher than common tunneling device without LCMO [144].

So far the approaches of magnetoelectric coupling we study still focus on the charge degree of freedom. The main message from the work in chapter 3 is that the charge at the interface could be different from the region far away from the interface. Therefore it is not trivial to assume that the charge profile will be the same as it is designed to be based on bulk doping ratio. This is particularly important for interface effects. The work in chapter 4 focuses on perusing the limitation of charge modulation effect by studying the exact composition at the phase boundary, which indeed shows a very large effect. However the work also reminds us to redesign the ME heterostructure by using modified phase diagram which includes the influence from the substrate strain. In other words, the actual phase boundary should be reconsidered as a multiple dimensional space such as charge, strain, size effect, etc.

This two works, together with many other works in the framework of charge modulation, provide more and more information to improve the design rules that should be followed. Nevertheless, another route, which uses the orbital degree of

freedom, hasn't been fully explored yet and therefore offers many new possibilities. Chapter 5 and 6 present the two different approaches to use the orbital degree of freedom.

Chapter 5

Magnetoelectric effects in charge/orbital ordered $Nd_{0.5}Sr_{0.5}MnO_3$

5.1 Motivation: simultaneous charge/orbital ordering and magnetic transition

As pointed out in the first chapter, the orbital degree of freedom, instead of its counterparts such as charge, hasn't been fully studied in the context of magnetoelectric coupling. The strong coupling between lattice and orbital degree of freedom has been well established, which makes it a promising route to pursue. However in order to search for the magnetoelectric coupling, one needs to think one step further, which is to establish the strong coupling between orbital and spin degree of freedom. In single atom or ion, the coupling is actually determined by the spin-orbit coupling strength, which is generally weak in 3d transition metal oxides since it is propositional to the Z^4 whereas Z is the atomic number. Therefore one could expect it to be much larger in the 5d transition metal elements, which will be discussed later in the next chapter. Nevertheless, there are still other possibilities in the 3d transition metal oxides. In some systems, the orbital and spin develop some kinds of ordering simultaneously. Although it remains a debate that which one is the primary driving force, the simultaneous occurrence of two orderings suggests the possible strong entanglement between them. Therefore despite of the weak spin-orbit coupling in atomic limit of 3d elements the coupling of orbital and spin ordering could potentially be strong.

Manganite system is one good example. As discussed before, the bandwidth of manganite can be tuned by A-site atom size, which determines the Mn-O-Mn bond angle. For large A site atom, the bandwidth is relatively large, usually leading to a disordered orbital state which is usually a ferromagnetic metal as shown in figure 5.1 (a). When A site atom is small, the bandwidth becomes so narrow that it usually

develops charge/orbital ordered insulating phase with high transition temperature. Moreover the antiferromagnetic ordering is more favorable with a relatively low Neel temperature [44]. However the medium bandwidth manganite turns out to be very intriguing. The medium bandwidth manganite, with the right composition (usually half A-site doped), usually exhibits a transition between orbital disordered state and ordered state. More importantly, magnetic ordering transition occurs simultaneously along with it. Actually there are several materials in this group. Figure 5.1 (a) shows the orbital phase diagram as a function of bandwidth and doping level, which could actually be tuned systematically by choosing different combinations of A site cations. The red shadow region is the area that shows this interesting behavior.

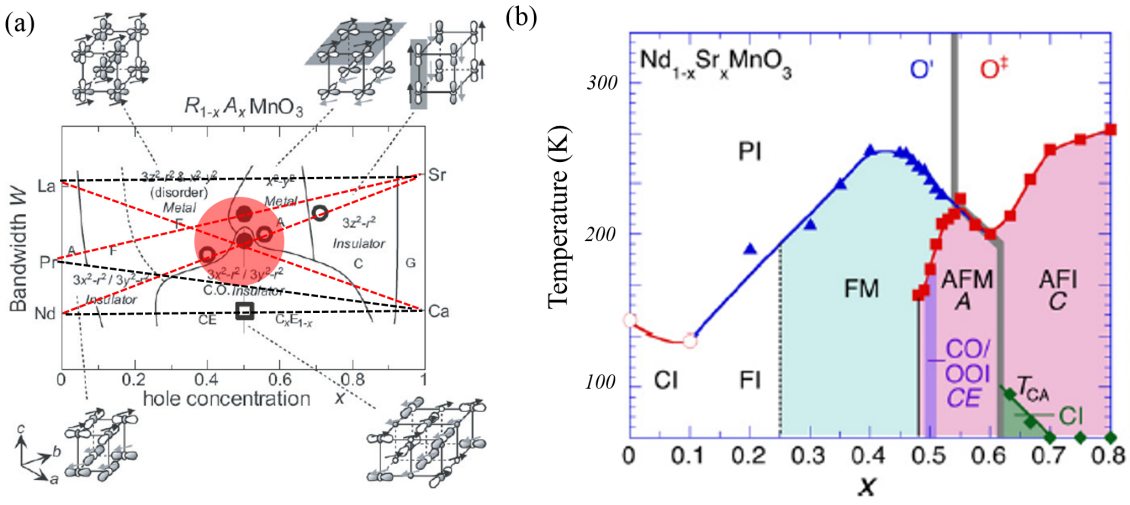

Figure 5.1: Phase diagram of manganite with intermediate bandwidth. (a) Orbital phase diagram of manganite with intermediate bandwidth as a function of doping ratio and A-site cation size. Compounds in the red shadow region shows simultaneous orbital and magnetic orderings. (b) Phase diagram of $Nd_{1-x}Sr_xMnO_3$ as a function of doping level and temperature. Adapted from [44].

Figure 5.1 (b) is the phase diagram of one such system $Nd_{1-x}Sr_xMnO_3$. At the half doped level $Nd_{0.5}Sr_{0.5}MnO_3$ (abbreviated as NSMO), a ferromagnetic transition occurs at T_c around 220K. Then an orbital ordering (OO), together with charge ordering (CO), develops at around 160K. Simultaneously, the ferromagnetic ordering transits into antiferromagnetic ordering (AF), which reveals the close connection between the AF ordering and CO/OO ordering. Since the transition happens between AF and FM orderings, it is reasonable to expect a large change of magnetization if one could use the lattice strain to suppress and CO/OO and thus AF ordering. Actually several other systems, such as $La_{1-x}Ca_xMnO_3$ and $Pr_{1-x}Sr_xMnO_3$, show the very similar behavior.

As discussed in the last section of chapter 4, substrate strain could significantly

change the magnetic ground state compared with bulk. Therefore the bulk phase diagram might not apply to thin film. Actually the result has been demonstrated. Figure 5.2 (a) shows the temperature dependance of magnetization and resistivity of NSMO on STO substrate with different orientations, only the NSMO thin film deposited on (011) oriented substrate shows the bulk like transition behavior. FM transition is observed at 220K, which is followed by another AF transition at 160K. The resistivity changes about 4 orders of magnitude, consistent with the CO/OO at low temperature. However thin films on STO (001) and (111) don't show this kind of behavior. [145]

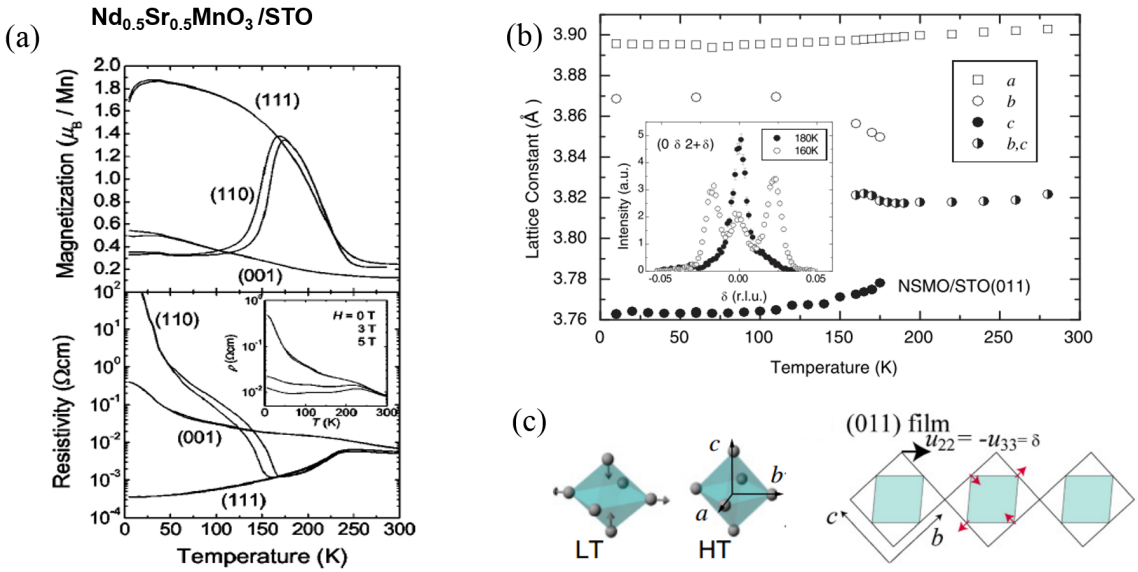

Figure 5.2: Magnetic, electronic and structure transition of NSMO thin film. (a) Temperature dependence of magnetization and resistivity of NSMO thin film on STO substrate with different orientations. (b) Structure change of NSMO thin film on STO (011), crystal axis a,b,c is defined as the pseudo-cubic unit cell. (c) Schematic of the lattice distortion across the phase transition. Adapted from [145, 146].

The reason is closely linked to the structure transition that happens at the CO/OO ordering temperature as shown in figure 5.2 (b) [146]. The high temperature phase of NSMO shows a structure with the almost same b and c lattice constant. Below the phase transition temperature, the crystal structure changes into a more orthorhombic-like form with b≠c, which manifests itself as the splitting of (002) diffraction peak. This structure change is consistent with the transition in bulk [147]. Actually the structure change is one kind of Jahn-teller distortion which favors the low temperature ordering phase. As for film epitaxially deposited on STO (001) both a and b lattice constant are locked by the substrate, which therefore forbid this structure transition.

On the other hand, this structure change is allowed on (011) oriented substrate since only a axis is locked by the substrate while b, c have the freedom to change in the form of shear distortion. The lattice distortion is shown schematically in figure 5.2 (c).

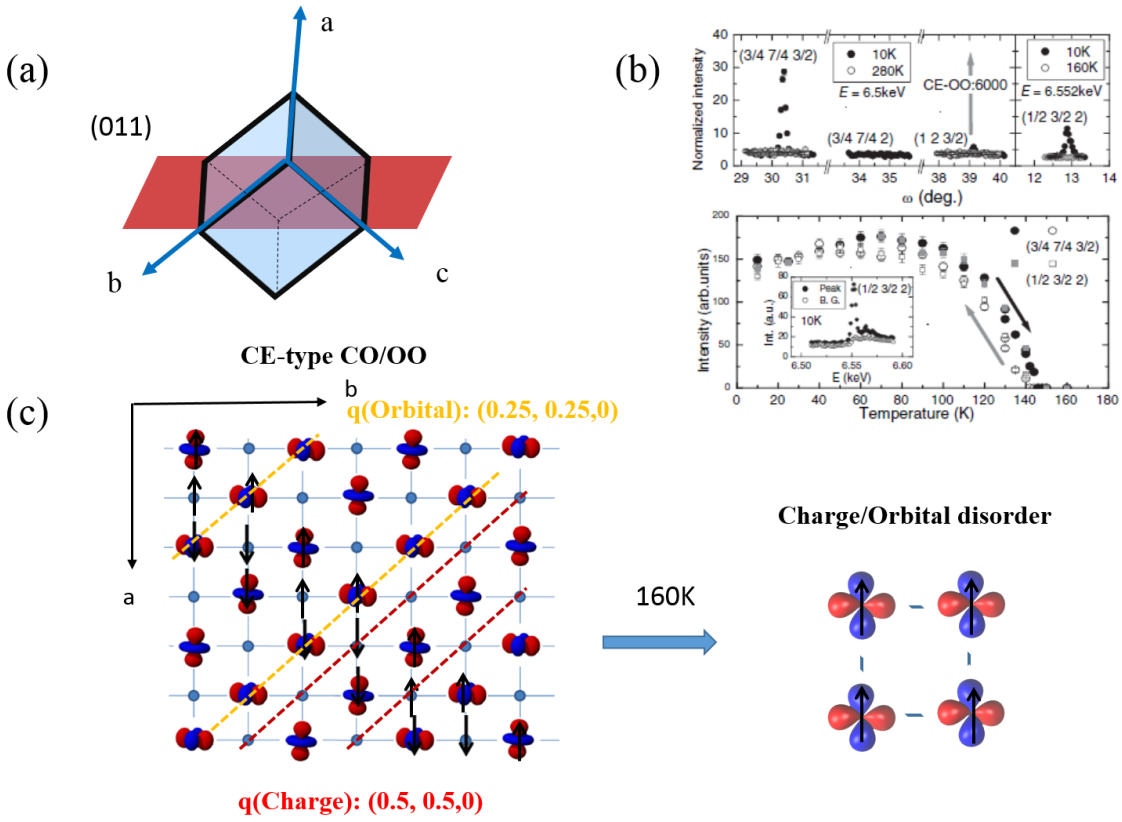

Figure 5.3: CO/OO characterization by X-ray diffraction in NSMO. (a) Definition of a,b and c crystal axis in the pseudo-cubic lattice of NSMO/STO (011). (b) CO and OO diffraction peak with the q vector characterized by (1/2, 1/2, 0) and (1/4, 1/4, 0) for CO and OO respectively along with the temperature dependance. (c) Schematic of the charge and orbital distribution of the CO/OO (CE type). Adapted from [146].

Actually the CO/OO has been directly observed by synchrotron X-ray diffraction [146, 148–150]. To clarify the definition of a,b,c crystal axis, the definition is shown schematically in figure 5.3 (a) in the pseudo-cubic form. The out of plane direction is defined as [011]. The charge and orbital develop the orderings in ab plane (In the definition, b>c after splitting. Of course domains with different b and c orientation coexist). Figure 5.3 (c) shows the schematic of charge and orbital distribution in the ordering phase of NSMO. In NSMO, there are 50% d^3 Mn^{4+} and 50% d^4 Mn^{3+}. Therefore half of the Mn cations have one electron in e_g orbital while the other half is

empty. In the ordering phase in ab plane, this one e_g electron occupies the alternative Mn site and therefore forms the ordering with the character q vector as (1/2, 1/2, 0), which is shown by the red dash line. For the Mn^{3+} site with one e_g electron. The electron will occupy the $3x^2$-r^2 or $3y^2$-r^2 due to the Jahn-Teller distortion. In reality the alternative $3x^2$-r^2 and $3y^2$-r^2 chains develop as shown in the figure 5.3 (c) (yellow dash line) with the q vector (1/4, 1/4, 0). In the CO/OO phase, spin also develops an interesting ordering pattern. The spins order parallel in the chain of Mn^{3+} and antiparallel between Mn^{3+} chains. In addition, spins order antiparallel in the Mn^{4+} chain. Therefore the overall ordering is antiferromagntic. The type of charge/orbital and spin ordering is often referred as CE type CO/OO/SO. These diffraction peaks corresponding to different ordering parameter have been successfully observed as shown in figure 5.3 (b) [146]. The temperature dependance reveals the transition between orbital ordered and disordered states around 160K.

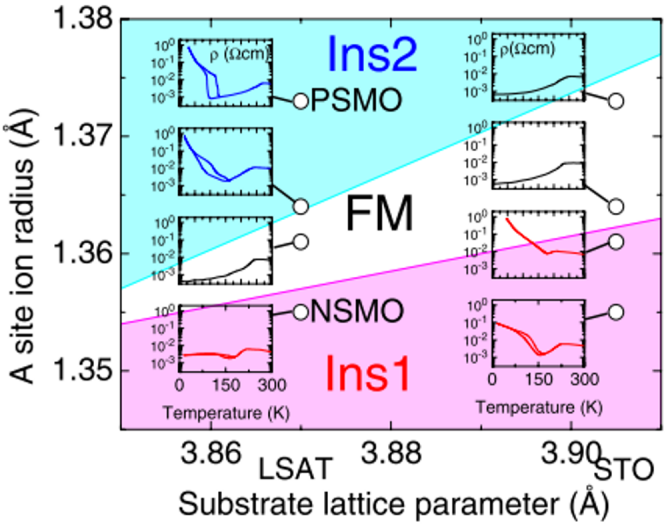

Figure 5.4: Ground state phase diagram of half-doped manganite thin films on (011) substrates. A site atom size is tuned by the mixing ratio of Nd and Pr atoms. Two substrates with different lattice constant LSAT and STO are used. Adapted from [148].

More intriguingly, strain effect definitely has a great effect on the magnetic ground state. Figure 5.8 shows the ground state of phase diagram of the half-doped manganite system. The internal chemical pressure is changed by the ratio between Nd and Pr at A-site. Different epitaxial strain is applied by using two different substrates. It is clearly shown that the certain combination of chemical pressure and epitaxial strain can stabilize the CO/OO states in thin films [148]. The dramatic change of ground state with small variation of chemical potential and strain also points out the fact that the ground state is very sensitive to the strain. Besides the strain engineering

in the as-grown states, several results also demonstrate the sensitivity of the ordering ground state to the external field such as pressure [151, 152], magnetic field [147] or light [153]. For example, the isotropic pressure in the order of GPa, or the magnetic field up to a few T can actually lead to the collapse of CO/OO state.

5.2 Growth of NSMO thin film and characterization

In this chapter the model system we study is NSMO/STO (011), which has been already well-studied by different experiment methods and therefore a good candidate to start with. Thin film NSMO was grown epitaxially on STO (011) substrate from the chemical stoichiometric ceramic target at the laser density of 2.5J/cm^2 and 1Hz repetition rate. The ground state of NSMO is quite sensitive to the doping ratio of Nd and Sr as verified by previous work [145]. In our study we find that the Nd and Sr ratio is very sensitive to the laser energy density and 2.5J/cm^2 is the optimized value based on magnetic and electronic characterization. All films were deposited at 800 ^{0}C and 150 mTorr, followed by the thermal anneal process at 5 ^{0}C/min in 760 Torr oxygen atmosphere. The thickness of NSMO is about 60nm, which shows the stable CO/OO.

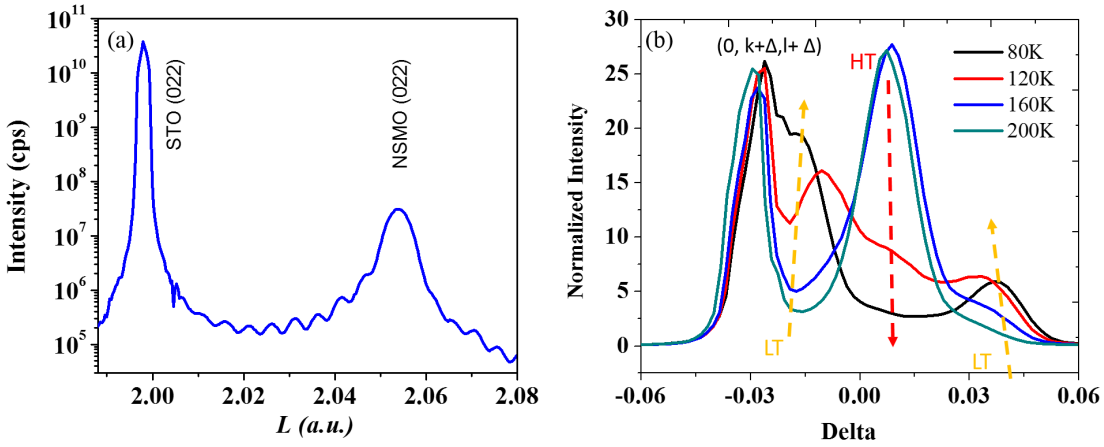

Figure 5.5: X-ray diffraction characterizations of NSMO thin film. (a) X-ray diffraction θ-2θ scan of NSMO/STO (011) thin film. (b) Temperature dependance of the (020) diffraction peak.

Figure 5.5 (a) shows the θ-2θ measurement of NSMO/STO (011) thin film, which reveals the epitaxial growth. The thin film is under tensile strain from the STO substrate. The thickness fringes demonstrate the high crystal quality of the thin film. Figure 5.5 (b) shows the temperature dependance of (020) peak of the NSMO thin

film. As discussed in last section, an orthorhombic phase transition occurs at the CO/OO, which splits the high temperature (HT,red) (020) peak into two low temperature (LT, yellow) peaks. The scan of 5.5 (b) is measured around (020) by keeping K=L. It is clearly shown that the (020) peak splits at the ordering temperature around 160K, consistent with the previous results.

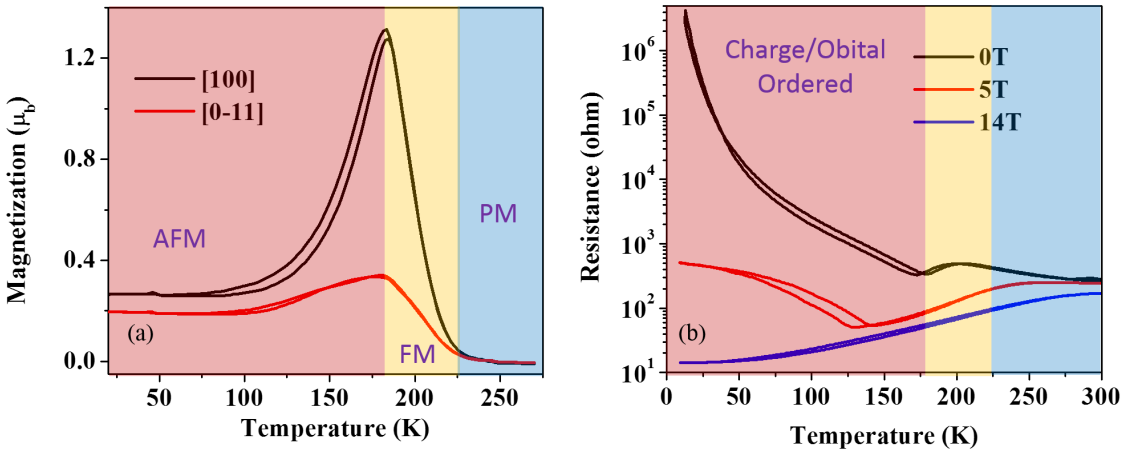

Figure 5.6: Magnetization and transport measurements of NSMO thin film. (a) Temperature dependance of magnetization of NSMO thin film with 200 Oe field applied in-plane. (b) Temperature dependance of resistance at different magnetic fields (current along [100] direction).

The films are also characterized by transport and magnetization measurements to check the ground state and phase transitions. Figure 5.6 (a) shows the temperature dependance of the magnetization measured with the 200 Oe magnetic field in-plane. The curve can be divided into three regions: paramagnetic (blue), ferromagnetic (yellow) and antiferromagnetic (blue). The temperature hysteresis observed in the M vs T curve suggests the FM/AF transition is a first order transition. Furthermore, measurements along two normal in-plane direction ([100] and [0-11]) reveals that the magnetic easy axis is in the crystal axis [100]. It is worth mentioning that a small quantity of magnetization is still observed even well below the transition temperature, suggesting the phase septation in this system all over the whole temperature range [154, 155]. Transport measurements also reveal similar behavior as shown in figure 5.6 (b), which can be also divided into three regions. The black curve is the temperature dependance of resistance measured at zero field. Two successive metal-insulator transitions have been observed in NSMO thin film, which corresponds to the PM/FM and FM/AF transition respectively. Resistance increases by roughly 4 orders of magnitude, which demonstrates the stabilization of CO/OO below the transition temperature.

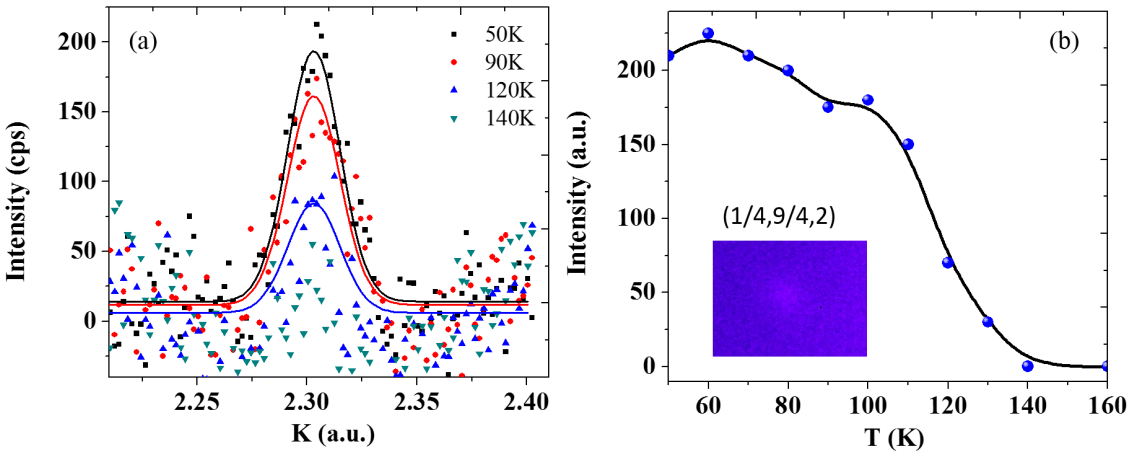

Figure 5.7: Temperature dependance of CO peak measured by X-ray diffraction. (a) K-scan of OO peak (1/4,9/4,2) of the NSMO thin film at different temperatures. (b) temperature dependance of OO peak intensity, inset shows the OO diffraction peak on the 2D detector screen.

Actually the OO diffraction peak is also observed directly on the NSMO/STO (011) film as shown in figure 5.3. The q vector of the peak we use is (1/4, 9/4, 2) with the character (1/4, 1/4, 0) as discussed in the first section. The appearance of a weak but detectable peak can be directly observed on the 2D detector as shown in the inset of figure 5.3 (b). Figure 5.3 (a) shows the K-scan across the diffraction peak (1/4, 9/4, 2) at different temperatures. The solid curve is the gauss fit of the data. The temperature dependance is summarized in the figure 5.3 (b), which is also consistent with previous studies. Therefore all these characterizations demonstrate the high quality of NSMO thin film, which exhibits successive magnetic phase transition and CO/OO in the low temperature antiferromagnetic phase.

5.3 Device fabrication and in-situ strain study

Although strain effects have been demonstrated through the epitaxial growth and bulk isotropic compression experiments, the in-situ strain study hasn't been fully explored on the CO/OO system to figure out the dynamics of charge/strain/spin evolvements. As pointed out in the two former sections, these ordered states can only be stabilized with specific crystal orientation and strain state. Therefore instead of fabricating a heterostructure consisted of NSMO and piezoelectric materials, we use a different approach to study the dynamics, which has been successfully used in studying the single crystals [156–158].

A tunable in-plane uniaxial strain is applied to the thin film samples by using a

commercially available piezostack. By gluing the sample on the side wall of a piezo stack as shown in figure 5.8 (a), strains can be applied by the deformation of the stack, which is controlled by an applied voltage. Figure 5.8 (b) is the schematic diagram of the piezostack. With negative voltage applied, the stack shrinks (dot lines) and the strain also transfers to the sample on top of it. In order to increase the strain transfer from the piezostack to the NSMO thin film, STO substrate is thinned down to a thickness below 50 μm to reduce the clamping effect from the single crystal substrate. The current is applied along the pseudo cubic [100] direction (magnetic easy axis).

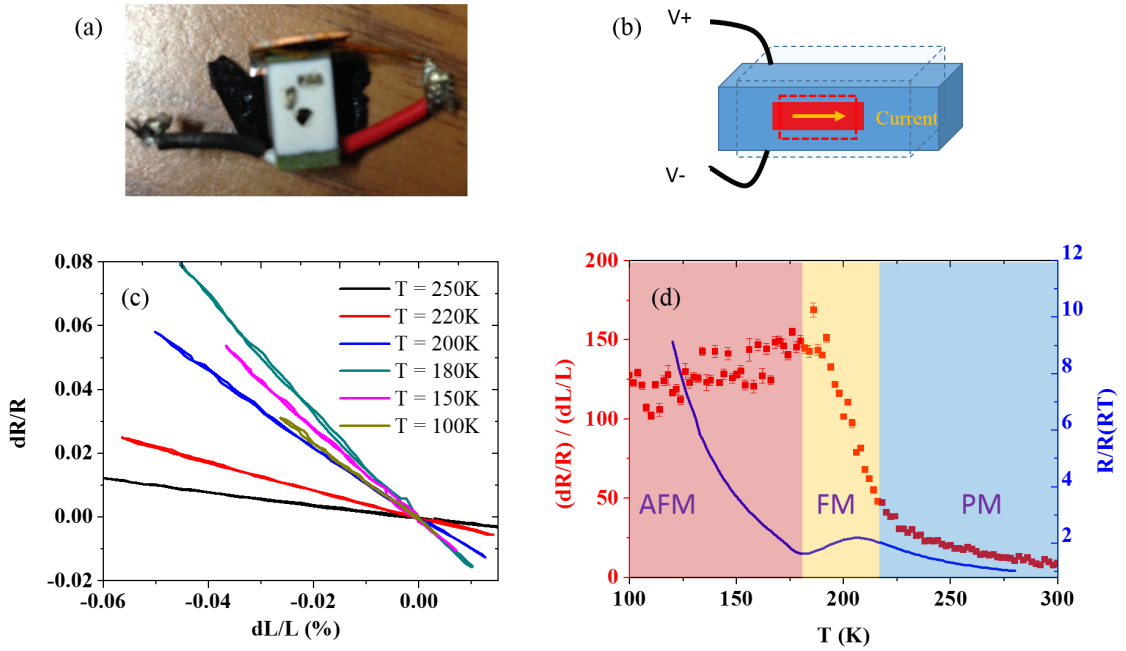

Figure 5.8: Schematic diagram of the piezoresistance measurements and the results. (a), (b) Real image and schematic diagram of the piezoresistance measurements set up. (c) Piezoresistance measured along [100] pseudo cubic direction at different temperatures. (d) Temperature dependance of the piezoresistance in the three magnetic phases.

Figure 5.8 (b) shows the piezoresistance measured at different temperatures. The strain (i.e., the fractional change of length along the current direction, $\varepsilon = \Delta L/L$) is monitored via a strain gauge glued on the back side of the piezostack. In this study, the negative ε refers to the elongation of the current direction [100]. Piezoresistance of the NSMO samples is shown in figure 5.8 (c) at different temperatures. The maximum of strain reduces as the temperature decreases. Nevertheless, the slop of the curve $((\Delta R/R_0)/(\Delta L/L_0))$ reveals the response of resistance to the strain. Since the sharp

change of resistance is related to the CO/OO, the slope also reveals information about the ordering states. It is clearly seen that the slope approaches the maximum around the FM/AF phase transition temperature and reduces a little bit below the phase transition point. Figure 5.8 (d) shows the temperature dependance of the response $((\Delta R/R_0/(\Delta L/L_0))$ as summarized in the three different phases. The results suggest a large charge and orbital modulation around the phase transition critical point.

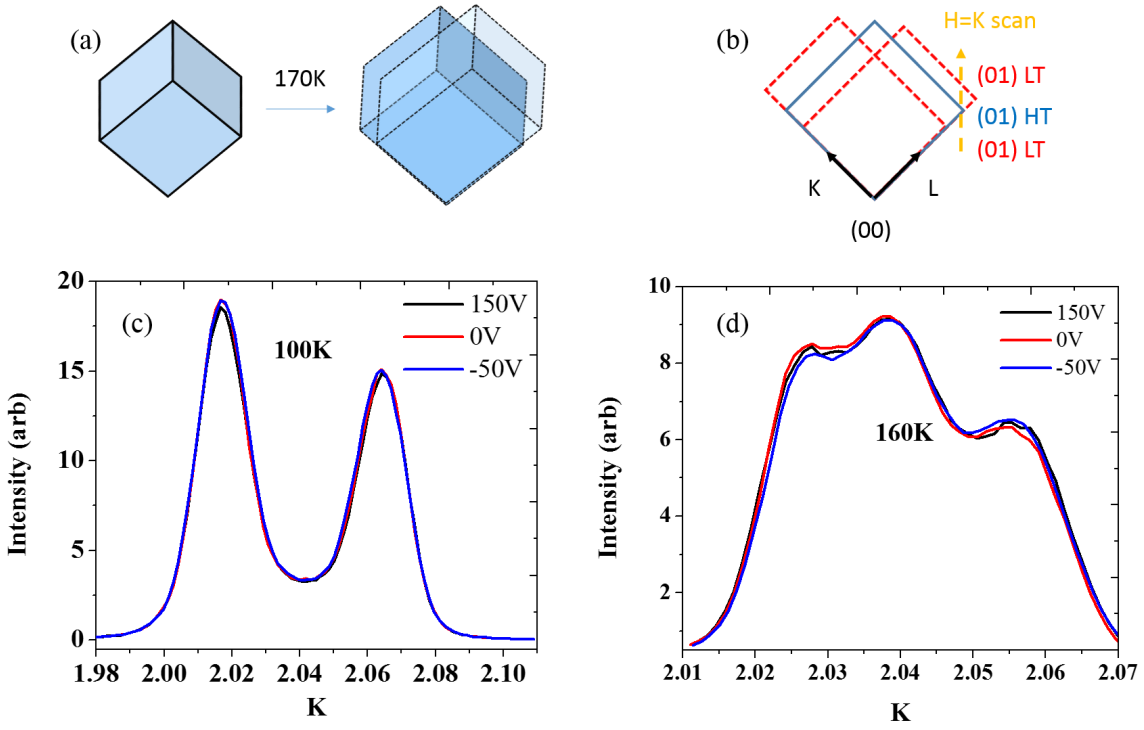

Figure 5.9: In-situ strain effect on the structural phase changes. (a), (b) Schematic of the structural change around the phase transition and the split of (020) diffraction peak. (c), (d) In-situ strain effects on the (020) diffraction peak at 100K and 160K.

Since the ordering is associated with the structural phase change, the in-situ strain effects on structural transition have also been studied. As discussed earlier, the split of (020) Bragg peak indicates the orthorhombic phase transition as shown in figure 5.9 (a) and (b). The strain effect on this (020) peak was carried out at the phase transition temperature (160K) and also well below the transition (100K) by a K=L scan at different voltages applied to the stack. Figure 5.9 (c) shows the result at 100K and the (020) peak fully splits into two. No clear structure change can be observed at this temperature. Figure 5.9 (d) shows the result at 160K, which is the phase transition point and reveals the largest piezoresistance modulation. However no clear structural change (the proportion of HT and LT phases) can be observed despite of

the almost 10% change of resistance.

Next the strain effect on the spin ordering was studied. XMCD was used to directly probe the change of magnetization with in-situ strain applied. The schematic diagram is shown in figure 5.10 (a), similar to the common geometry used in previous studies. However the high voltage (150V) applied across the stack could lead to a leakage current, which thus greatly increases the noise to signal ratio. Several pieces of high quality single crystal $LaAlO_3$ are inserted between the stack and the XMCD probe rod, which then greatly reduce the leakage problem. Temperature dependance of XMCD reveals a maximum at 160K as shown in figure 5.10 (b), consistent with the magnetic phase transition observed by SQUID. The strain effect is also studied at the phase transition point by applying different voltages. Figure 5.10 (c) doesn't show a significant modulation of XMCD signal by applying the voltages. Therefore the results suggest that strain has a minor effect on the magnetic ordering despite of the large modulation of resistivity.

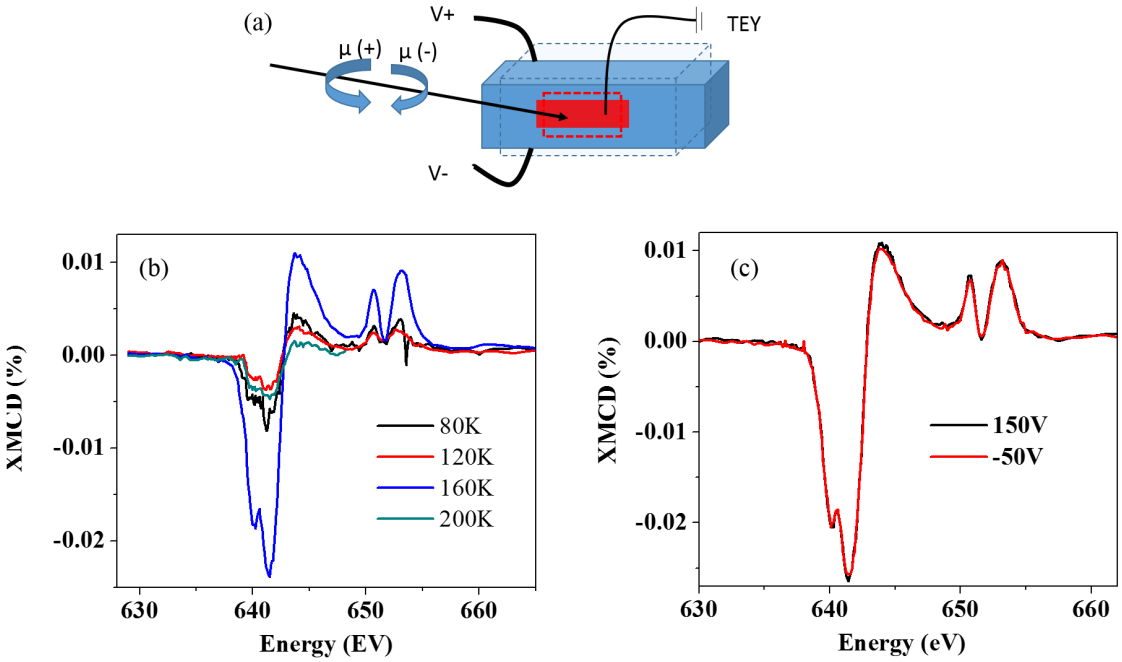

Figure 5.10: In-situ strain effect on the magnetization of NSMO. (a) Schematic of the magnetization change probed by XMCD technique. (b) Temperature dependance of the XMCD signal, consistent with magnetic transition measured by SQUID. (c) Strain effect on the magnetization at 160K.

5.4 Conclusion and further discussion

In this chapter we studied the in-situ strain effects on the charge, spin and orbital ordering in the half-doped manganite NSMO. The key results are as following: the piezoresistance shows a large modulation effect with the maximum at the phase transition temperature. However the structure and magnetic ordering reveal a minimal change.

First let's discuss the piezoresistance modulation. It is worth mentioning that the strain applied by the piezostack is around 0.1% at room temperature and reduces as the temperature decreases, which is at least one order smaller than the strain that is sufficient to fully suppress the ordering [151,152]. Therefore the strain can be treated as a perturbation, similar to the AC voltage in the dielectric measurements or AC field in the magnetic susceptibility measurements. Resistivity is closely related to the CO/OO parameter, which would definitely open a gap in the ordering phase. Therefore the response of resistance reflects the charge and orbital ordering information. As an analogy to magnetic susceptibility, the term $(\Delta R/R_0)/(\Delta L/L_0)$ could also be treated as orbital susceptibility. The results suggest a maximum of orbital susceptibility around the transition temperature, which is similar to the counterpart at the magnetic transition where the fluctuation is maximum. This hypothesis needs further in-situ X-ray scattering experiment to support. However it is likely to be a demonstration of a new and much easier approach to probe the orbital states.

Secondly, the minimal change of magnetization at the phase transition temperature despite of the large piezoresistance suggests that the dynamics of spin, orbital and charge are not identical. In other words, spin ordering is less sensitive to the strain compared with charge and orbital. This could be due to the lack of strong intrinsic coupling between spin and orbital degree of freedom. Therefore the results strongly suggest an urgent need to study the materials with strong intrinsic spin-orbit coupling.

Chapter 6

Tailoring the magnetic anisotropy by using strong spin-orbital coupling $SrIrO_3$

6.1 Motivation: strong spin-orbit coupling 5d transition metal oxides

As discussed in chapter 1, the route 4, which utilizes the orbital degree of freedom, hasn't been intensively explored yet. It is well known that the orbital degree of freedom is very closely tied to the lattice degree of freedom. Therefore in terms of magnetoelectric coupling effect, a close connection between spin and orbital degree of freedom has to be established. The intrinsic physical mechanism is the spin-orbit coupling (SOC), which is a relativistic effect rooted in quantum mechanics. The magnitude of SOC is proportional to Z^4 (Z is the atomic number). Therefore the energy of SOC is much smaller than other energy terms, such as columbic energy or kinetic energy, in 3d transition metal oxides (TMO) and is generally neglected. However 5d transition metal oxides host the SOC with the magnitude comparable with other energy terms, which therefore turn out to be best candidates in this scenario.

Among all the 5d transition metal elements, the most well-studied one is Ir, which has been successfully synthesized in different compounds. One of the intriguing materials is Sr_2IrO_4, a layered perovskite with low-spin d^5 configuration, in which five electrons are accommodated in almost triply degenerate t_{2g} orbitals. Although metallic ground states are expected in 5d TMOs because of their characteristic wide bands and small coulomb interactions, it turns out to be an magnetic insulator [160]. A recent study has shown that the strong SOC inherent to 5d TMOs can induce a Mott instability even in such a weakly correlated electron system, resulting in a localized state very different from the well-known spin S = 1/2 state. It is proposed to be an effective total angular momentum J_{eff}=1/2 state [49], which is schematically shown

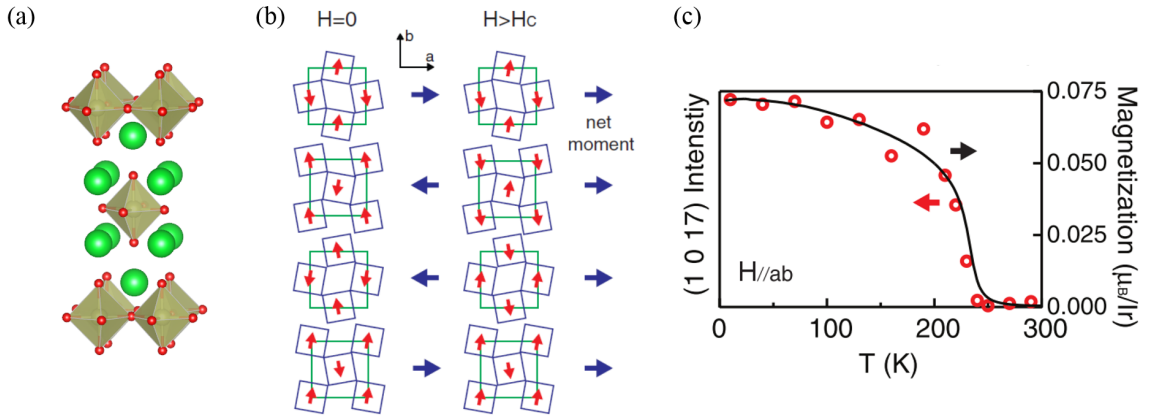

Figure 6.1: Magnetic ordering of strong SOC Sr_2IrO_4. (a) Crystal structure of layered perovskite Sr_2IrO_4. (b) Antiferromagnetic ordering revealed by the magnetic resonant x-ray diffraction. (c) Temperature dependance of the canting moments. Adapted from [159].

in figure 1.6. More interestingly, Sr_2IrO_4 develops an antiferromagnetic ordering below 270K with this novel strong SOC J_{eff}=1/2 state. The novel magnetic ordering has been studied by resonant magnetic scattering as shown in figure 6.1 (b) [159]. It shows a canted antiferromagnetic ordering pattern of J_{eff}=1/2 moments (arrows) within IrO_2 planes. The stacking pattern along the c axis in zero field is anti-parallel, which would become parallel by applying magnetic field. The magnitude of canting moment is $\sim$0.08 μ_B, much lager than the 3d counterpart such as $BiFeO_3$.

Sr_2IrO_4 is one member of the layered perovskite Ir-TMOs as shown in figure 6.2. Previous study revealed interesting spin-flop driven by the dimensionality effect. In layered perovskite $Sr_3Ir_2O_7$, easy c-axis collinear antiferromagnetic structure was observed, significantly different from the single layer Sr_2IrO_4 with in-plane canted moments [161]. Furthermore the dimensionality control of metal-insulator transition was also studied theoretically and observed experimentally [162]. In terms of coupling across the heterointerface, the Ir-O-A bonding (A is a 3d transition metal cation) determines the physical properties as discussed in chapter 1. Therefore one can expect the best candidate would be the perovskite $SrIrO_3$, which hosts the direct Ir-O-A bond without any SrO extra layer (figure 6.2 (a)).

$SrIrO_3$, which is abbreviated as SIO in the rest of this chapter, has been successfully synthesized in 1970s. However the crystal structure of the bulk SIO is hexagonal with a monoclinic distortion instead of the perovskite structure [163]. Single crystal SIO shows a non-Fermi-liquid metallic behavior and is proposed to be close to the ferromagnetic instability [164]. Perovskite phase of SIO has also been successfully stabilized in thin film form with the help of epitaxial strain from substrate, which is also revealed to be a paramagnetic metal [165]. Analogy to the dimensionality con-

trol observed in the layered perovskite series $Sr_{n+1}Ir_nO_{3n+1}$, one could expect novel ground state of SIO in heterostructure and superlattice due to the dimensionality reduced bandwidth. Actually the J_{eff}=1/2 state of Sr_2IrO_4 has been observed experimentally [166] and explained theoretically in the SIO/$SrTiO_3$ superlattice [167].

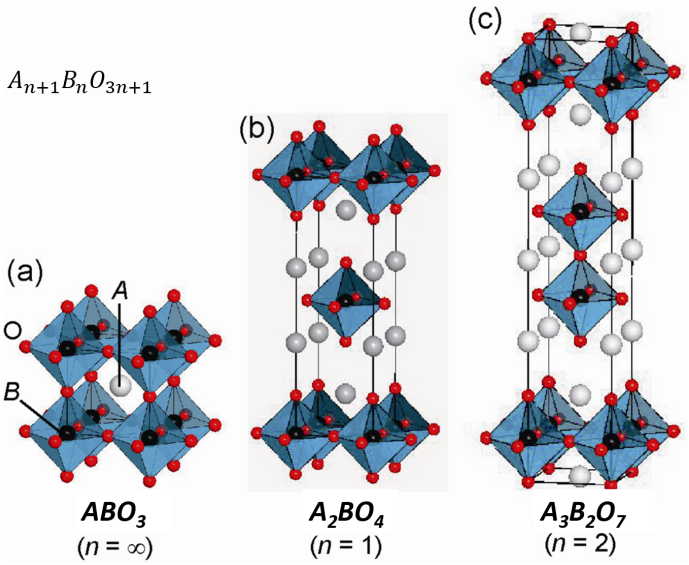

Figure 6.2: Crystal structure of the layered perovskite family of Ir TMO with the formula $Sr_{n+1}Ir_nO_{3n+1}$.

Inspired by these previous works, SIO might be a good candidate to explore the magnetoelectric coupling in the strong SOC limit. However the first step is to explore the ground state of SIO when the dimensionality is reduced and also the coupling to other 3d TMOs, especially those with magnetic orderings. Therefore the work in this chapter focuses on the LSMO/SIO superlattice (LSMO refers to $La_{2/3}Sr_{1/3}MnO_3$). With a combination of different experimental methods, two major questions should be answered: 1. what is the ground state of SIO in the superlattice due to reduced dimensionality and Ir-O-Mn bond? 2. How does SIO changes the ferromagnetic properties of LSMO?

6.2 Previous work: Sr_2IO_4/LSMO heterostructure

Since the magnetic structure has been well studied in the Sr_2IrO_4 (abbreviated as S2IO4 in the following) as shown in the last section, the heterostructure consists of LSMO and S2IO4 was studied [168]. The central motivation is to explore the coupling between the 3d and 5d magnetic cations, which would serve as the foundation for further study of paramagnetic SIO. S2IO4 is the antiferromagnetic semiconductor

and the Mott gap opens as a consequence of electron correlations, AF order and strong spin-orbit coupling.

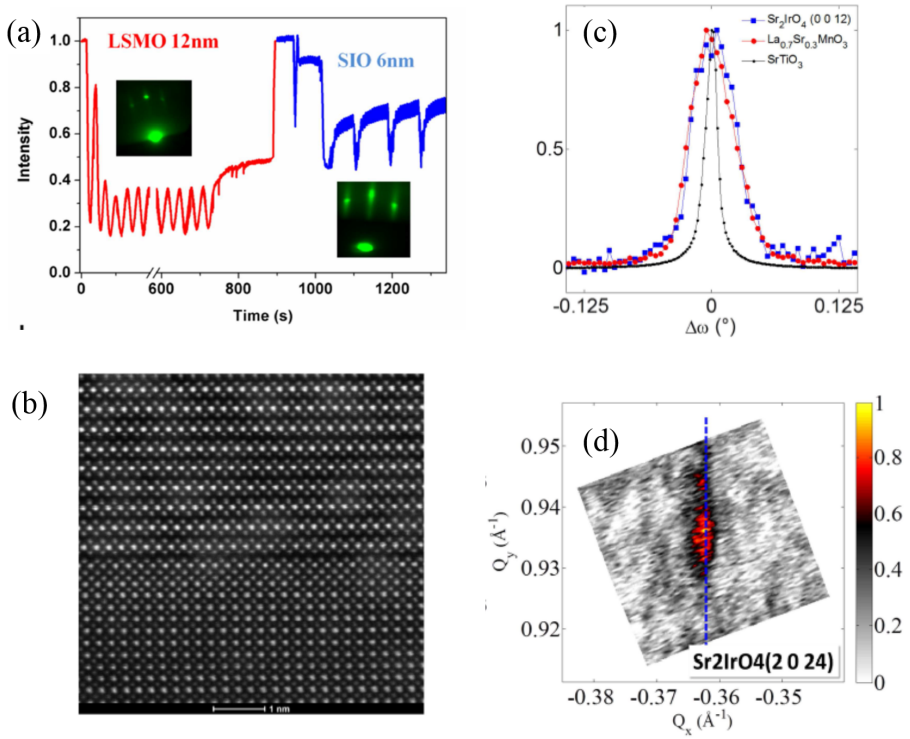

Figure 6.3: Growth and structure characterization of S2IO4/LSMO heterostructure. (a) RHEED pattern and typical RHEED oscillations used to control the growth. (b) Scanning transmission electron microscopy image of the S2IO4/LSMO bilayer. (c) X-ray diffraction rocking curves around the STO(002), LSMO(002) and S2IO4(00 12) reflections. (d) Reciprocal space mapping (RSM) of S2IO4/LSMO bilayer. Adapted from [168]

The heterostructure was deposited by pulsed laser deposition (PLD) assisted by reflection high-energy electron diffraction (RHEED). Before the growth, the STO substrate was wet-etched with buffered HF acid, followed with a thermal annealing process, which forms a TiO_2 terminated atomic flat top surface. LSMO (12nm) and S2IO4 (6nm) were grown epitaxially on the STO substrates from the stoichiometric targets at a laser energy density of 1.5 J/cm^2 and a repetition rate of 1 Hz. LSMO was grown at 700 C and 150 mTorr partial oxygen pressure while SIO was grown at 800 C and 1mTorr. During the deposition, the RHEED intensity oscillations were collected and are shown in figure 6.3 (a). The data indicates a layer by layer growth for each material in both samples. After the growth, the samples were cooled to room temperature in 760 Torr oxygen ambient at a rate of 5C/min.

Figure 6.3 (b) shows the cross-section TEM image of the heterostructure, which indicates an atomically sharp interface between the LSMO and S2IO4. Xray-diffraction rocking curves for LSMO and SIO, measured at the peak positions in data shown in figure 6.3 (c), present a full width at half maximum of 0.05 degree. Reciprocal space maps (RSM) demonstrate a fully epitaxial growth of S2IO4 and LSMO (figure 6.3 (d)), which is strained to the substrate of STO.

In order to explore the magnetic coupling between LSMO and SIO, magnetization hysteresis loops were measured at different temperatures as shown in figure 6.4 (a). The coercivity of the bilayer is much larger than that of LSMO single layer, which indicates the magnetic coupling between LSMO and S2IO4. In order to further prove that, another comparison sample was measured, in which 4nm of LNO is inserted between LSMO and S2IO4. The coercivity reduces in this sample, which again confirms the coupling between LSMO and the antiferromagnetic ordering of S2IO4.

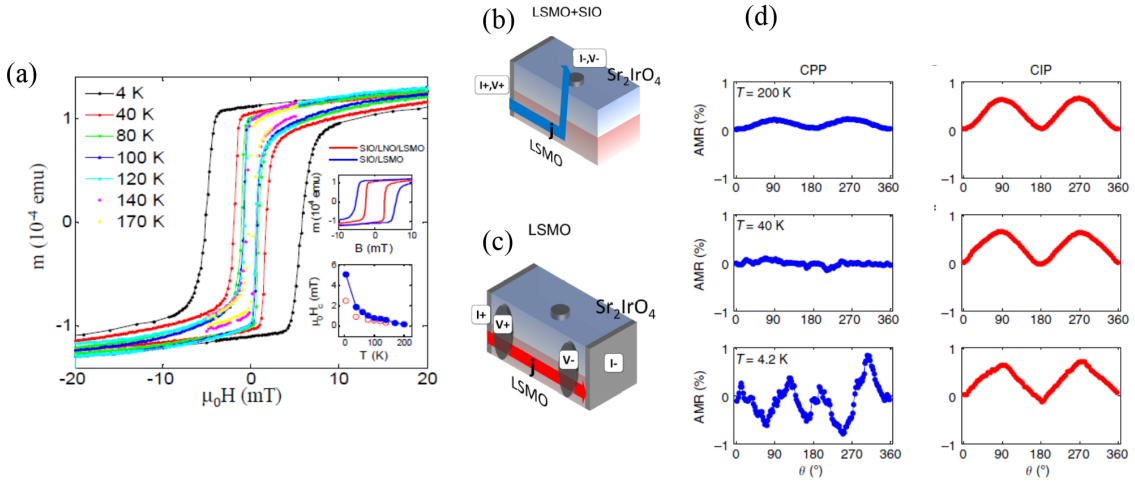

Figure 6.4: Magnetization and anisotropy magntoresistance of the LSMO/S2IO4. (a) Magnetization of the SIO/LSMO bilayers at various temperatures vs magnetic field applied along the [100] axis. (b),(c) Schematic for the anisotropy magntoresistance (AMR) measurements with OOP (b) and IP (c) current direction. (d) AMR of the S2IO4/LSMO bilayer with current perpendicular to (CPP) and in the film plane (CIP) with magnetic field of 100 mT.

The strong spin-orbit coupling makes S2IO4 a favourable semiconductor AF for observing the relativistic anisotropic magnetotransport (AMR) phenomena, which in turn reveals the information of magnetic ordering. Figure 6.4 (b) and (c) show the schematic of the device geometry for the AMR measurements. In the vertical-lateral geometry (6.4 (b)), one electrode is attached on the free top surface of S2IO4 and electrical current is driven vertically through S2IO4 and then laterally through LSMO. A 4-points measurement has been used to measure the LSMO resistance in the

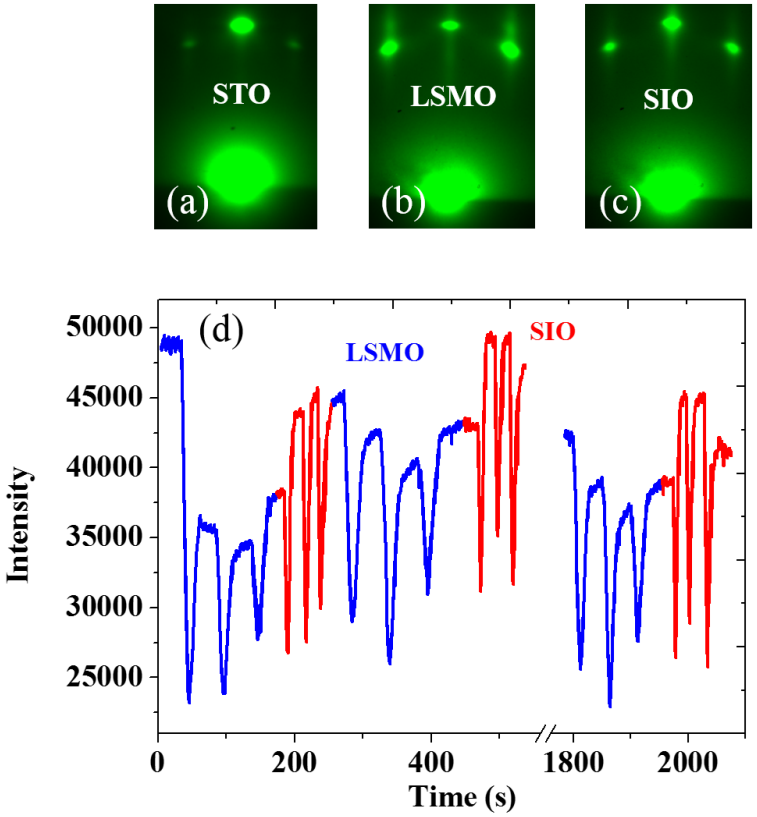

Figure 6.5: RHEED Patterns and oscillations of the superlattice. RHEED pattern of STO substrate (a), LSMO sublayer (b) and SIO sublayer (c). (d) RHEED oscillations show the layer-by-layer growth of both SIO and LSMO.

lateral geometry as shown in the sketch of 6.4 (c). The in-plane channel (right panel of figure 6.4 (d)) is dominated by the metallic LSMO and shows the 2-fold angular dependance, typical for ferromagnetic metal [169]. On the other hand, the vertical channel, which is dominated by the semiconducting S2IO4, shows the 4-fold angular dependance, which is demonstrated to be related to the rotation of antiferromagnetic axis [168]. Therefore the results clearly reveal the rotation of antiferromagnetic axis of S2IO4 in the bilayer by using a relatively small field, which would otherwise need a much higher field as a single layer. Therefore the results also strongly suggest the exchange-coupling between S2IO4 and LSMO. The temperature dependance indicates that the coupling disappears at a relatively low temperature (below 40K), which is consistent with our analysis above and possible due to the extra SrO layer at the interface.

In summary, we demonstrates the existence of magnetic coupling between LSMO and S2IO4 in the bilayer structure, which could be used to switch the antiferromag-

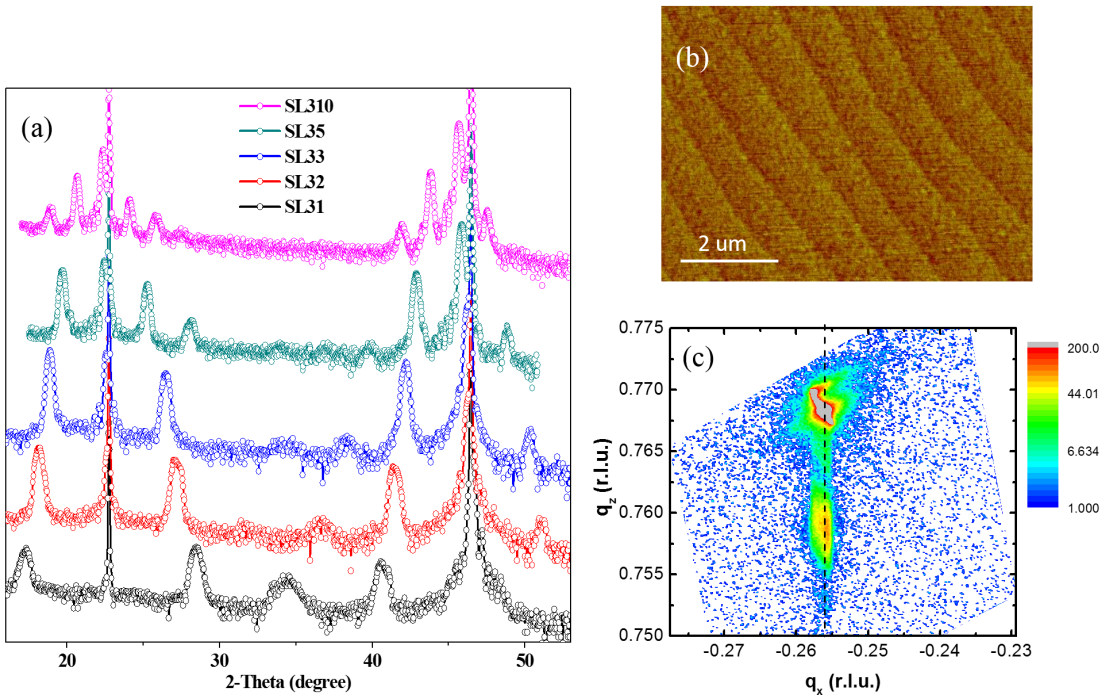

Figure 6.6: Structure characterization of superlattice by X-ray and AFM. (a) θ-2θ scan of a serial of superlattices with different SIO thickness. (b) AFM image of surface morphology of superlattice. (c) Reciprocal space mapping (RSM) of $[LSMO]_3[SIO]_5$ superlattice.

netic axis of S2IO4 with a relatively small field. The microscopic mechanism of the exchange coupling is still an open question. Furthermore, the relatively low blocking temperature in the bilayer highlights the potential advantages to use the perovskite $SrIO_3$, which would provide a direct Ir-O-Mn bond as discussed in the first section. The following of this chapter focuses on the SIO/LSMO superlattice.

6.3 Fabrication of LSMO/SIO superlattice

Epitaxial superlattices were grown by reflection high-energy electron diffraction (RHEED) assisted pulsed-laser deposition and comprised specifically designed thickness of $La_{2/3}Sr_{1/3}MnO_3$ (LSMO) and $SrIrO_3$ (SIO) on TiO_2 terminated $SrTiO_3$ (STO, (001) oriented) substrate. RHEED intensity oscillations were observed for both LSMO and SIO throughout the growth, which were used to precisely control the thickness to the scale of one unit cell as shown in figure 6.5 (a). During the whole growth process, both SIO and LSMO layers show a good 2D pattern, which reveals the high

quality of the interface. The surface morphology of the superlattice was also checked by AFM as shown in figure 6.2 (b). The surface terrace structure with atomic step height, which is identical to the surface of substrate, again confirms the high quality of the samples.

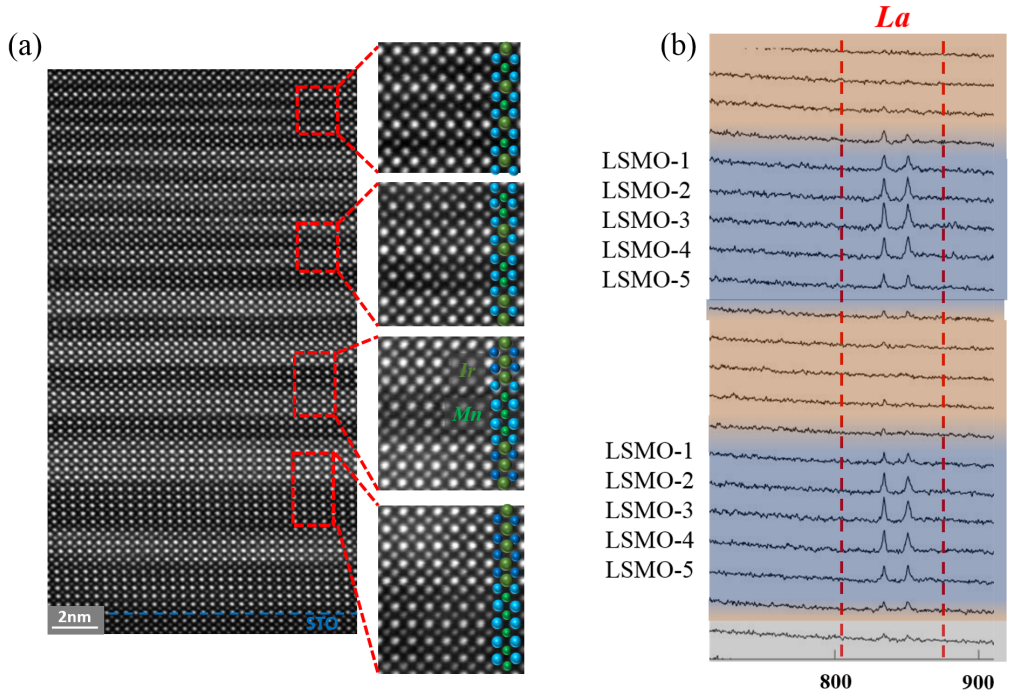

Figure 6.7: STEM images of LSMO/SIO superlattice. (a) High-angle annular dark-field (HAADF) STEM images of LSMO/SIO superlattice with intentionally designed series of periodicity in one sample. The four zoom-in images show the regions of $[LSMO]_1[SIO]_1$, $[LSMO]_2[SIO]_2$, $[LSMO]_3[SIO]_3$ and $[LSMO]_5[SIO]_5$ from top to bottom. (b) EELS mapping of La edge of the superlattice.

In order to study the dimensionality effect of SIO, superlattices with varied SIO thickness are fabricated as $[LSMO]_3[SIO]_n$ (one periodicity consists of 3 unit cells of LSMO and n unit cells of SIO, each superlattice is consisted of several repeated periodicity). Figure 6.6 (a) shows the θ-2θ X-ray diffraction scan of the $[LSMO]_3[SIO]_n$ with n=1, 2, 3, 5, 10. The satellite peaks corresponding to the superlattice structure and the finite size oscillations arising from the thickness are well pronounced in the series, suggesting the high degree of interface abruptness and good agreement with the designed periodicity. Figure 6.6 (c) is the reciprocal space mapping (RSM) of $[LSMO]_3[SIO]_5$, the identical value of Q_x vector of both the thin film and substrate reveals that epitaxial strain is coherent in the superlattice.

Furthermore the cross-section scanning TEM provides direct information of the interface. Figure 6.7 (a) shows the STEM image of one superlattice sample with

differing periodicities in repeated patterns (The zoom-in images correspond to the sequence of $[LSMO]_1[SIO]_1$, $[LSMO]_2[SIO]_2$, $[LSMO]_3[SIO]_3$ and $[LSMO]_5[SIO]_5$ from the top, the number refers to the thickness in unit cell). The extremely sharp Z-contrast change of B site species across the interface suggests the minimal inter-diffusion of Mn and Ir atoms. Since the STEM contrast is dominated by the large difference of atomic number (Z) between Mn and Ir, the A site Z-contrast is not obvious. However the line profile of the electron energy loss spectroscopy (EELS) of La edge across the interface also confirms the atomically flat interface as shown in figure 6.7 (b) in the region of $[LSMO]_5[SIO]_5$. The diffusion of La into SIO layer is within one unit cell.

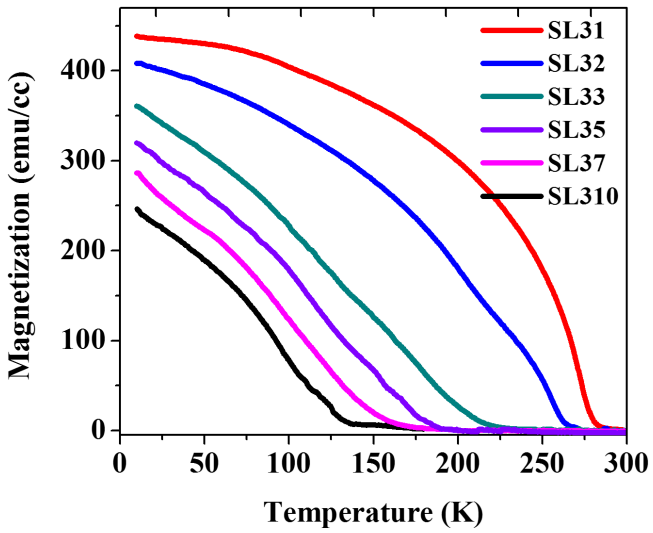

Figure 6.8: Temperature dependance of magnetization of the superlattice $[LSMO]_3[SIO]_n$. The superlattice $[LSMO]_3[SIO]_n$ is abbreviated as SL3n in the images (n= 1, 2, 3, 5, 7, 10). The temperature dependance is measured with 100Oe after a 1T field cooling.

6.4 Tailoring the magnetic anisotropy in superlattice

With the well-characterized high quality superlattices, we then studied the change of magnetic properties. As shown previously, LSMO is a good ferromagnetic materials with T_c around 340K in thin film. In the series of superlattice $[LSMO]_3[SIO]_n$, the curie temperature and magnetization reduces as the thickness of SIO increases, which is clearly shown in figure 6.8. For simplicity, $[LSMO]_3[SIO]_n$ is abbreviated as

SL 3n (n is the thickness of SIO) in the rest of this chapter. The trend is similar with the previous work on LSMO/STO superlattice [170, 171]. However both the magnetization and curie temperature is higher in the LSMO/SIO superlattice, probably related to the metallic nature of SIO thin film.

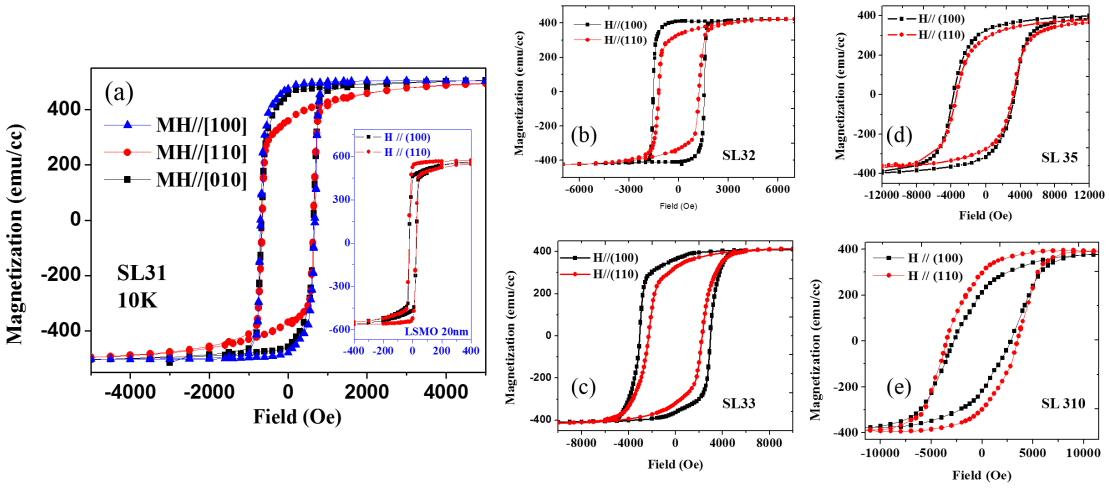

Figure 6.9: In-plane magnetic anisotropy of superlattice $[LSMO]_3[SIO]_n$ at 10K. (a) Magnetic hysteresis of SL31 along pseudo cubic direction [100], [110] and [010], inset shows the magnetic hysteresis of 20nm LSMO thin film. (b)-(e) Magnetic hysteresis along two direction [100] and [110] for SL3n with n=2, 3, 5, 10.

Another important aspect of magnetic properties is the magnetic anisotropy. In order to check the magnetic anisotropy of the superlattice, magnetization hysteresis was measured by Quantum Design SQUID along different crystal directions. Figure 6.9 (a) shows the magnetic hysteresis of the superlattice SL31 measured along [100], [110] and [010] at 10K. The crystal direction is defined in the notion of pseudo cubic structure. It is clearly shown that the magnetic easy axis is along [100] direction. However for a LSMO thin film, the magnetic easy axis is along [110] as shown in the figure 6.9 (a) inset, which is also consistent with many previous works [172, 173]. Therefore the insert of 1 unit cell of SIO seems to change the in-plane magnetic anisotropy in the SIO/LSMO superlattice. In order to correlate the dependance to the thickness of SIO, similar experiments were carried out in the rest of superlattice with 2, 3, 5 and 10 unit cells of SIO as shown in figure 6.9 (b)-(e). The magnitude of the anisotropy could be defined as the difference of remanent magnetization between [100] and [110] direction normalized by the saturation moments. It is clearly demonstrated that the magnitude of the new anisotropy (easy axis along [100]) reduces as the thickness of SIO increases from 2 to 5. Further increase of SIO (to 10 unit cells) recovers the magnetic anisotropy of LSMO thin film, which is along [110] direction.

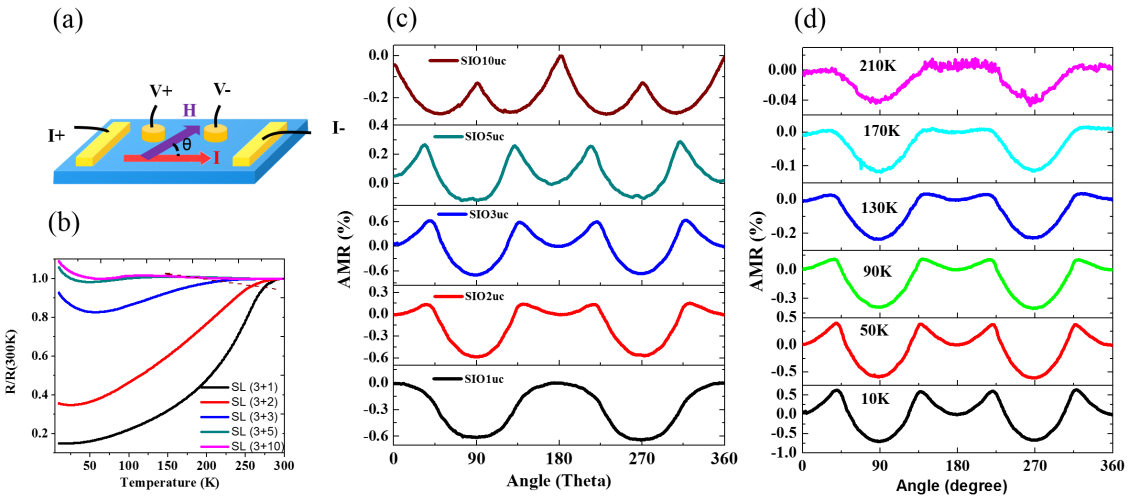

Figure 6.10: Anisotropy magnetoresistance (AMR) of LSMO/SIO superlattices. (a) Schematic of the device geometry for AMR measurement, current is applied along [100] crystal axis and magnetic field is rotated in-plane. (b) Temperature dependance of the superlattics. (c) AMR of superlattices at 10K with 1T field applied. (d) Temperature dependance of AMR for SL33.

Magnetic anisotropy was further explored through transport measurement. The typical anisotropic magnetoresistance (AMR) can be expressed as $\rho(\theta) = \rho_\perp + (\rho_\perp - \rho_\parallel)\cos 2\theta$, where $\rho_\perp$ and $\rho_\parallel$ are resistivity for current perpendicular and parallel to the magnetization. This two fold oscillation of AMR is related to spin scattering process and the phase is determined by the current [169]. Nevertheless, the four-fold AMR has also been observed in several systems such as high T_c cuprates [174] and manganite [175]. It has been demonstrated that the four-fold AMR is related to the crystal symmetry. More precisely, it reflects the magnetocrystalline anisotropy [176]. The AMR was measured by using the geometry shown in figure 6.10 (a) with current along crystal axis [100] and magnetic field 1T applied in the film plane. Temperature dependance of resistance is shown in figure 6.10 (b) for the serial of superlattices. When the thickness of SIO is within 1-2 unit cell, the RT curves are similar to that of LSMO, which shows a metallic behavior. As the thickness of SIO increases, the resistance increases and the RT curves reveal the bad metallic behavior similar to SIO. A metal-insulator transition can be observed at low temperature. This temperature dependance of resistance is correlated with the dependance of magnetization as shown in figure 6.8, considering the ferromagnetic metallic nature of LSMO.

Figure 6.10 (c) shows the AMR of the superlattices at 10K with magnetic field 1T. For LSMO3/SIO1, the transport behavior is dominated by LSMO and therefore shows the two-fold dependance, which is mainly due to the spin scattering effects.

For $[LSMO]_3[SIO]_n$ (n=2, 3, 5), four-fold AMR is clearly observed with maximum at 45 degree from the current ([110] crystal axis). On the other hand, LSMO3/SIO10 shows the four-fold AMR with maximum at 90 degree ([100] crystal axis). This 45 degree shift of AMR maximum is consistent with the shift of magnetic anisotropy as shown in the figure 4.6, which again confirms the tailoring of magnetic anisotropy in the superlattice as a response to SIO thickness.

So the key question should be raised: what is the fundamental driving force for the 45 degree switch of magnetic anisotropy of LSMO? To answer that, we should first review the possible change of magnetic anisotropy of LSMO in the epitaxial thin film. First of all, epitaxial strain could change the anisotropy. LSMO grown on the orthorhombic substrate such as $NaGaO_3$ reveals an uniaxial (2-fold) anisotropy, as pointed out before [177]. The driving force is the change of crystal symmetry imposed by the substrate. Furthermore, it has been demonstrated that the substrate steps also lead to uniaxial anisotropy [178]. However these can not be the reason since what we observe in the superlattice is 45 degree shift of 4-fold anisotropy. Besides, the substrate is cubic STO (low-miscut angle) with very large terrace width.

It has also been proposed that the oxygen octahedral pattern of manganite would determine the in-plane anisotropy. It was observed that the 4-fold magnetic anisotropy shifts 45 degrees in $La_{0.7}Ca_{0.3}MnO_3$ comparing with $La_{0.7}Sr_{0.3}MnO_3$ and $La_{0.7}Ba_{0.3}MnO_3$, which is likely due to the orthorhombic crystal structure of LCMO. It has been shown that the octahedral rotation pattern could be altered at the interface [179–181]. SIO thin film is orthorhombic and therefore provides one possibility. However if the the structure of LSMO is changed at the interface by SIO, one would expect large effect with increasing thickness of SIO, which would then stabilize the octahedral rotation pattern of SIO. However the thickness dependance we observe is exactly opposite, which thus rules out this possibility. Actually the most significant effect is observed at thin limit of SIO thickness, which implicates some emergent magnetic ordering in SIO as suggested in the first section.

6.5 XMCD of SIO: novel magnetic state

To check the magnetism in LSMO and SIO layer in the superlattice and the possible coupling, X-ray absorption (XAS) and X-ray magnetic dichroism (XMCD) measurement were carried out, which are elemental selective due to the fingerprint nature of the resonant excitation. The XAS and XMCD of Mn L-edge (around 640 eV, soft X-ray) was measured at the beamline 4.0.2 of Advanced Light Source in Lawrence Berkeley National Lab and that of the Ir L-edge (around 11-12 keV, hard X-ray) was measured at the beamline 4-ID-D of Advanced Photo Source at Argonne National Lab. The inset of figure 6.11 shows the schematic of measurement geometry for the XMCD experiment. The spectra of Mn was collected by the total yield electron (TEY) mode at the 30 degree incident angle. The spectra of Ir edge was recorded

by the fluoresce detector and the incident angle is a few degree due to the large penetration depth of the hard X-ray. The magnetic field is applied within the film plane along [100] direction.

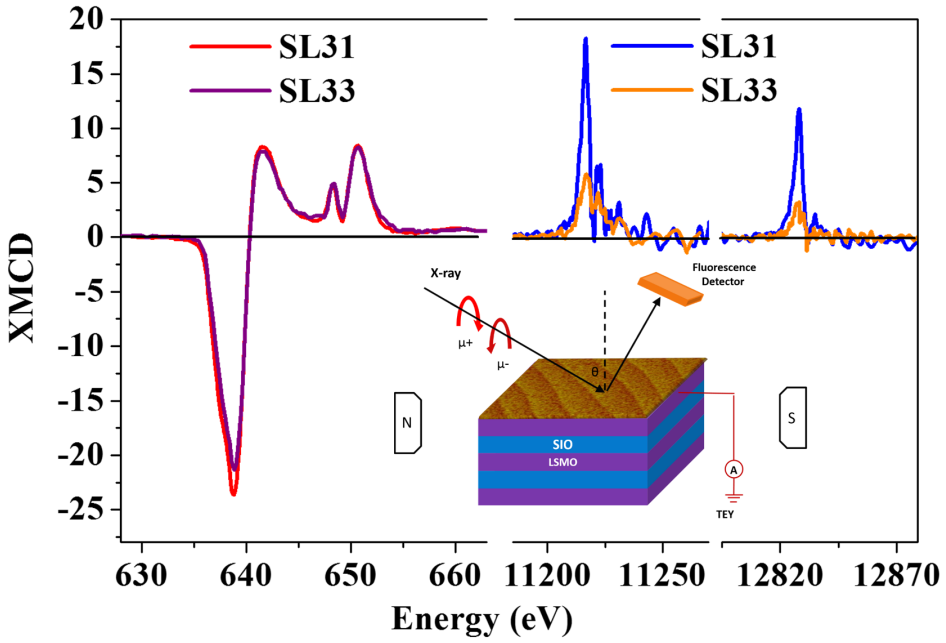

Figure 6.11: XMCD spectra of the LSMO/SIO superlattices. XMCD spectra of Mn (red) and Ir (blue) of the superlattice SL31 and Ir (yellow) of SL33. The magnitude of the XMCD signal is normalized by the magnitude of L_3 XAS respectively. Inset shows the geometry for the XMCD measurement.

Figure 6.11 shows the XMCD spectra of LSMO/SIO superlattices: Mn (red) and Ir (blue) of the superlattice SL31 and Ir (yellow) of SL33. The magnitude of the XMCD signal is normalized by the magnitude of L_3 XAS respectively. For comparison, the magnitude of XMCD signal of Ir (blue) is multiplied by a factor of 25. Magnetic dichroism is clearly present at both the Mn and Ir edge. The large dichroism of Mn is expected for the high spin-polarized ferromagnetic LSMO. However the presence of XMCD at the Ir edge is very intriguing and unambiguously shows the onset of a net magnetization in the SIO, which is otherwise a paramagnetic metal in bulk. Experimental artifacts were ruled out by changing both the photon helicity and the magnetic field direction. More importantly, the opposite sign of dichroism (the same photon helicity and field direction) demonstrates the antiparallel orientation of Mn and Ir moments, which clearly reveals the nontrivial nature of the magnetic coupling.

The XMCD of Ir edge can be flipped by magnetic field as show in figure 6.12. The red dot shows the sign of XMCD measured at the peak of L_2 edge XMCD

in figure 6.11 for SL31. The reversal of XMCD signal (flip) shows a quite similar behavior comparing with the magnetization hysteresis of the superlattice with the almost same coercivity field, which again confirms the strong coupling between Mn and Ir. Furthermore, spin sum rules analysis was applied to the Ir edge XMCD, which yields another unexpected striking result. Figure 6.13 shows the schematic on how we apply the spin-sum rule based on the equation 4.1 and 4.2. The orbital moment (M_l=0.036 ub/Ir) is much larger than the spin component (M_s+$< T_z >$=0.002 ub/Ir), which can be qualitatively deduced from the unique feature of the dichroism spectra, i.e. the same sign and similar amplitude of L_2 and L_3 edge. Since the real value of $< T_z >$ is unknown, we cannot extrapolate the ratio of spin and orbital momentum directly. If the ratio $< T_z >/< S_z >$ of 0.18 is applied, which is calculated from the configuration interaction calculations [182], then the orbital to spin momentum ratio would be more than 10, significantly larger than the theoretical value for the J_{eff}=1/2 state [49].

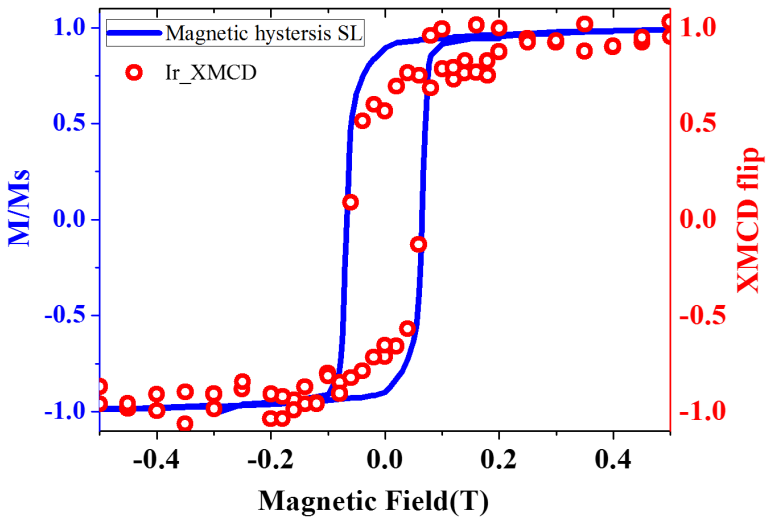

Figure 6.12: Magnetization hysteresis loop and the magnetic field flip of XMCD sign of SL31. The blue curve is the magnetization hysteresis loop measured at 10K. The red dots represent the ratio of XMCD signal at each H field normalized by the saturation value. Energy for XMCD is kept at the peak of L_2 XMCD.

Therefore the close connection between the novel magnetic ordering in SIO and the change of magnetic anisotropy of the superlattice has been established. It is worth discussing a little more about the Ir layer. First of all, the Ir atom is not in the J_{eff}=1/2 state anymore. The typical feature of J_{eff}=1/2 state in S2IO4 is the absence of L2 XMCD signal, the reason of which has been elaborated in the reference [159]. However in the superlattice, almost equal magnitude of XMCD signal for L_3 and L_2 edge is observed. Therefore an interesting question is the driving force for it.

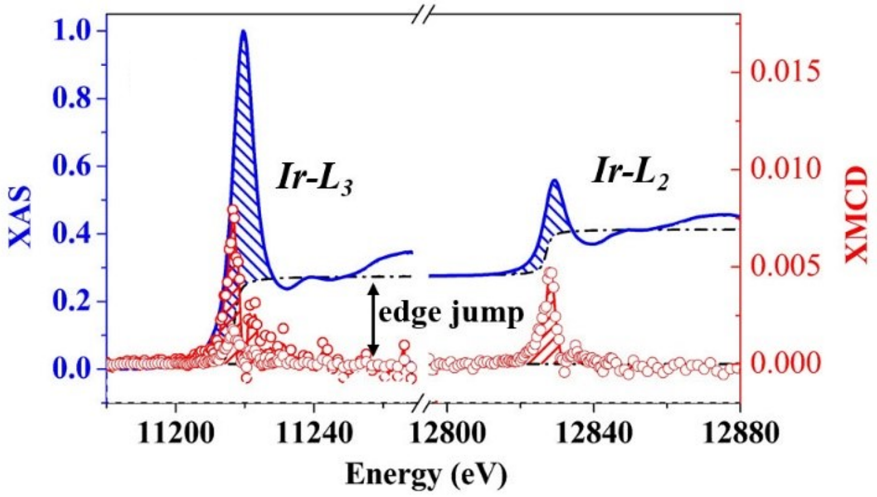

Figure 6.13: Spin sum rule applied to the superlattice SL31. (a) Comparison between the field flip sign of XMCD of Ir edge (red dot) and the magnetic hysteresis of SL31 (blue curve). (b) Schematic of the spin sum rule applied to the XMCD spectra of SL31.

First of all, charge transfer might be a possible reason, which would change the valence state of Mn and Ir. To probe that, we compared the core-level XAS spectra of the Mn and Ir edge of the superlattice to that of the single layer reference. Figure 6.14 (a) and (b) show the XAS spectra of Mn (red curve) and Ir (blue curve) of the SL31 superlattice taken at the resonant L_2 and L_3 edges at 10K. As a comparison, XAS spectra of LSMO (purple curve, figure 6.14 (a)) and SIO (purple curve, figure 6.14 (b)) thin films were taken simultaneously. It has been extensively studied that the XAS peak positon and multiplet fine structures are sensitive to the Mn valence state [131]. The similar results have also been observed in Ir compounds [183]. The absence of peak position shift and the identical multiplet features between the superlattice and the single layers suggest the minimal effect of charge transfer between Mn and Ir atoms. Therefore it rules out the charge transfer between Mn and Ir across the interface. Another possible reason is the magnetic coupling between Ir and Mn, which is actually hinted by the configuration interaction calculations [182], although the magnitude is still far less than what we observe in the superlattice. However it is likely to be the possible reason since LSMO is a high spin-polarized ferromagnet and therefore the coupling strength could be much stronger.

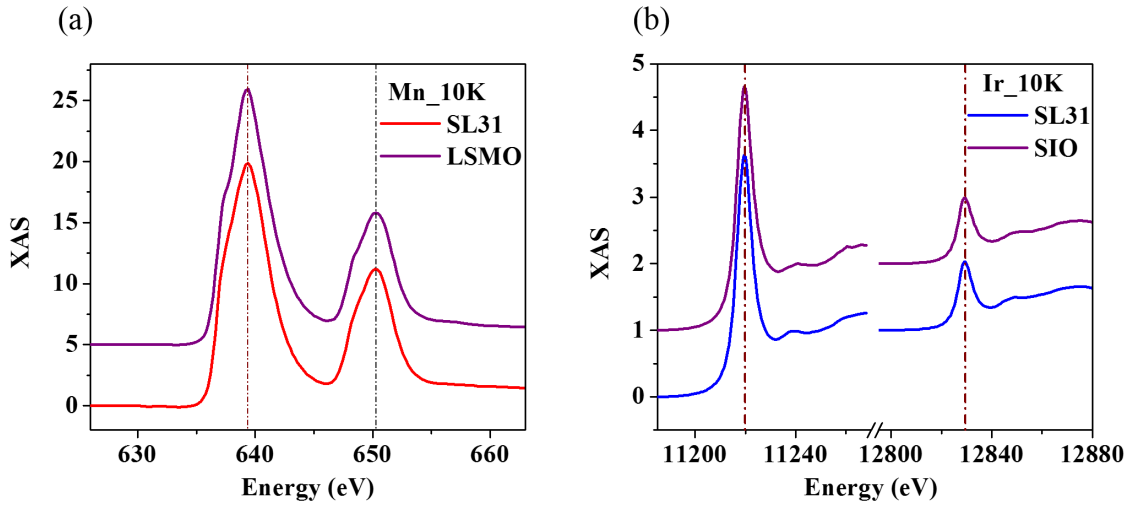

Figure 6.14: XAS of Mn and Ir edge of SL31 compared with reference. Core-level absorption spectra of Mn (a) and Ir (b) of the superlattice SL31 are shown along with the spectra of LSMO and SIO thin film (purple curve). Peak positions of the XAS spectra of the superlattice remain the same as the thin film in both Mn and Ir edge within the experimental limit, which suggest the minimal effect of charge transfer in the superlattice.

6.6 Summary and implication

In this chapter, the work on LSMO/SIO superlattice is presented. The key findings are as following:

1. In the superlattice, SIO develops a novel magnetic structure. It is not J_{eff}=1/2 as the magnetic mott insulator S2IO4 anymore and presents a very large orbital/spin moment ratio. It is likely that the new state is due to both the thickness effect and magnetic coupling to the ferromagnetic LSMO.

2. The magnetic anisotropy of the superlattices (magnetization mainly from LSMO) could be manipulated by this novel ordering in SIO, which manifests as the 45 degree shift of four-fold in-plane magnetic anisotropy.

The true magnetic ground state of SIO in the superlattice still remains an open question. Based on the small net moments and the theoretical prediction discussed in the first section with analogue to S2IO4, it is fair to guess that the magnetic ground state is canted antiferromagntic. However since it is not J_{eff}=1/2 any more, the prediction and analogy might not work. XMCD spectra could not provide the information about ordering and further diffraction studies are needed to clarify the ordering state.

Since the novel magnetic ordering is observed as the SIO layer thickness is reduced

to a few unit cells. It is a very good candidate for the interface engineering. For example, extra SIO layer can be inserted into the FE(multiferroic)/FM heterostructure such as PZT/LSMO, BFO/LSMO, etc. Firstly, SIO hosts a large orbital momentum, which is likely to be closely correlated to the lattice degree of freedom. Secondly, since the functional thickness of SIO is only a few unit cells, which is within the screening length of FET geometry. It is also very suitable to study the carrier modulation as shown in chapter 3 and 4. Moreover, SIO is strongly coupled to 3d transition metal oxides with exotic properties as shown in this chapter and therefore quite suitable as the tunable bridge materials at the interface. The physics of coupling mechanism between 3d-5d transition metal oxides are less well studied and requires further more research into other systems.

Chapter 7

Conclusions and future prospects

Multiferroic materials have returned to the forefront of materials research driven by the desire to achieve new functionalities as well as to deepen the understanding of fundamental physics. Researchers have undertaken a concerted effort to identify and understand the complexities of multiferroic materials. Although the ability to create high quality thin films leads to the flurry of research activities on the single component multiferroics, the scarcity of possible candidates, as well as the weak intrinsic magnetoelectric coupling, inspires researchers to explore this topic in a more engineering route, i.e. to design the multiferroic heterostructure. These artificially created materials exhibit intriguing phenomena more than just integrating the properties of each components. The high quality heterointerfaces, owing to the recent technical advances in the atomic-scale synthesis of oxide heterostructures, provide a fertile ground to achieve the coupling between different degree of freedoms, i.e. lattice, charge, orbital and spin. The entanglement between all these different degrees of freedom points out various routes to achieve the electric control of magnetism. Among them two have been intensively explored, i.e. coupling between lattice and spin (magnetostriction) and coupling between charge and spin (carrier doping). In this dissertation, we first presented a study focusing on how to optimize the performance within the framework of charge/spin coupling. By using the atomic-scale synthesis, some new design rules have been demonstrated, which are usually neglected in the previous studies. Furthermore, we explored the route that utilizes the orbital/spin coupling in two different approaches, which shed light on a novel design paradigm.

We first investigated the BFO/LSMO heterostructure in chapter 3, which serves as one of the model systems in the previous studies. However few attention has been paid to the atomical stacking sequence at the interface, which has been demonstrated to play an important role in other systems. By using the RHEED-assisted PLD, heterostructures with different interface stacking sequences (polar structure) have been successfully fabricated, which show dramatically different magnetoelectric coupling behavior. The key concept to understand the interface engineering effect is the extra charge transfer induced by the polar discontinuity, which could be extended to many

other systems as an additional design route.

Inspired by the results from chapter 3, we explored the modulation limit in the framework of charge/spin coupling by using the materials near the FM/AF phase boundary in chapter 4. In the model system BFO/LCMO, we successfully demonstrated the electric control of FM/AF transition based on a combination studies of magnetometery, XMCD and first principal calculations, which manifests as the large ratio of magnetization modulation. Also the results intrigue further implications of two topics in this design paradigm: length scale and substrate effect. The screening length in the typical FET device geometry is within a few unit cells, which points out the urgent need of a material with small dead-layer thickness. Moreover substrate effect (such as stain effect or charge transfer), could significantly change the phase diagram of a film in ultra-thin limit compared with the bulk. Therefore the design should base on the revised phase diagram for the optimal performance instead of the bulk phase diagram.

Another interesting aspect of the study is to use orbital/spin coupling. The strong lattice/orbital coupling has been well established. Therefore the central problem to use orbital degree of freedom in achieving magnetoelectric coupling is to establish the coupling between orbital and spin. Two approaches have been studied in the dissertation. In chapter 5, a model material (NSMO) with simultaneous spin/orbital ordering is used. The concurrence of two orderings with respect to external stimulus such as temperature or magnetic field suggests the existence of a possible artificial coupling between spin and orbital. The in-situ stain experiment reveals a sensitive response of orbital ordering to the lattice. Despite of that the spin ordering doesn't show the same magnitude of change. Inspired by the results, we turned to study the materials with intrinsic strong spin-orbit coupling, which is the 5d transition metal oxides. However the magnetic ordering of 5d transition metal oxides, as well as the coupling to 3d counterparts, haven't been well understood yet. Chapter 6 presents a systematic study of LSMO/SIO superlattices. The magnetic anisotropy of the superlattice shows a significant change due to the existence of SIO ultrathin layer. The novel magnetic ordering has been observed in the SIO layer by XMCD of the Ir L-edge, which is strongly coupled to the 3d Mn cation.

With these studies setting the stage, there are several interesting research issues that can be pursued with regard to design the multiferroic heterostructure. Such endeavors are enlisted here for the possible future directions.

1. Establishing the phase diagram of manganite thin film in ultrathin limit: As discussed in chapter 4, the optimal performance in the framework of charge/spin coupling strongly depends on the magnetic layer (usually manganite) in the ultrathin thickness. The bulk phase diagram, which is usually referred as the design rule, turns out to be incorrect at this limit. Besides the common variables such as the carrier concentration or temperatures for bulk, the new phase diagram should be built with additional dimensions, such as the strain from substrate and the charge transfer at the interface. The core question is to find a material at the phase boundary in the

ultrathin thin film limit. The necessity to obtain the revised phase diagram has already attracted attentions recently in some systems. However a systematic study, especially for the wide bandwidth manganite, still remains unsolved.

2. Size effect and single domain switching: All the magnetoelectric coupling effects demonstrated in chapter 3 and 4 in the FET device geometry originate from the average over many domains of BFO. The proposed model is based on an oversimplified picture which treats the multiferroic BFO uniformly at the interface. However some puzzles remain unclear, such as the location of the pinned sites. From the structure point of view, domain walls may function quite differently from the domains by considering the different symmetry. Therefore the study of single domain is very useful to differentiate the contribution from the two components, which would have two fold influence. First, it reveals the right direction to optimize the magnetoelectric coupling effect since the domain engineering has been well established in BFO and other ferroelectrics. Secondly, it serves as the guideline to shrink the device size as required in the modern memory devices.

3. Tuning the spin-orbit coupling in $BiFeO_3$: In BFO, the Dzyaloshinskii-Moriya interation links the microscopic charge order (ferroelectric dipole) to the microscopic spin order (canting moments). The latter is the key component to achieve the magnetic coupling with other materials. Therefore attempts have been made to alter the magnetic ordering as well as the degree of spin canting in $BiFeO_3$, mainly through chemical doping or strain engineering. However the fundamental cause of Dzyaloshinskii-Moriya interation is the spin-orbit coupling. So far there have been no attempts to strengthen the spin-orbit coupling in this room temperature multiferroic reported. If it could be successfully achieved, it is likely to lead to a significantly enhanced effect with much better reliability. Therefore it is worth perusing to dope the B site atoms with 5d heavy elements such as Ir or to design superlattice to explore the ideal.

4. Interface engineering using 5d transition metal oxides: As demonstrated in chapter 6, the novel magnetic ordering with large orbital momentum is observed in the SIO layer as the thickness decreases to a few unit cells. Furthermore this ordering is strongly coupled to 3d transition metal oxides such as FM LSMO. Therefore it is a very good candidate for the interface engineering, considering the compatible thickness of screening length. Therefore it is worth exploring the influence of extra SIO layers in the multiferroic(FE)/FM heterostructure. Besides, a more systematic study of interface coupling between 3d/5d transition metal cation is urgently needed as a solid foundation.

The presented issues above are just a few of the unexplored questions with respect to design the magnetoelectric heterostructure. Definitely there are much more besides the ones answered or raised in this dissertation. I believe that answering such questions is relevant to both a fundamental understanding of magnetoelectric multiferroics as well as to accomplish the more comprehensive rules to design the heterostructures.

Bibliography

[1] M. Fiebig. Revival of the magnetoelectric effect. *Journal of Physics D: Applied Physics*, 38:R123–R152, (2005).

[2] I. E. Dzyaloshinski. On the magneto-electrical effect in antiferromagnets. *Sov. Phys. JETP*, 7(8):628–629, (1961).

[3] V. J. Folen, G. T. Rado, and E. W. Stalder. Anisotropy of the magnetoelectric effect in Cr_2O_3. *Physical Review Letters*, 6(11):607–608, (1961).

[4] G. T. Rado and V. J. Folen. Observation of the magnetically induced magnetoelectric effect and evidence for antiferromagnetic domains. *Physical Review Letters*, 10(3):310–311, (1960).

[5] P. Borisov, A. Hochstrat, X. Chen, W. Kleemann, and Cl. Binek. Magnetoelectric switching of exchange bias. *Physical Review Letters*, 94(117203), (2005).

[6] X. He, Y. Wang, N. Wu, A. N. Caruso, E. Vescovo, K. D. Belashchenko, P. A. Dowben, and C. Binek. Robust isothermal electric control of exchange bias at room temperature. *Nature Materials*, 9(7):579–585, (2010).

[7] W. F. Brown, Hornreic.Rm, and S. Shtrikman. Upper bound on the magnetoelectric susceptibility. *Physical Review*, 168(574), (1968).

[8] H. Bea, M. Gajek, M. Bibes, and A. Barthelemy. Spintronics with multiferroics. *Journal of Physics-Condensed Matterr*, 20(434221), (2008).

[9] W. Eerenstein, N. D. Mathur, and J. F. Scott. Multiferroic and magnetoelectric materials. *Nature*, 442(7104):759–765, (2006).

[10] D. Khomskii. Classifying multiferroics: Mechanisms and effects. *Physics*, 2(20), (2009).

[11] J. M. D. Coey. *Magnetism and Magnetic Materials*. Cambridge University Press, Combridge, UK, 2010.

[12] Zener C. Interaction between the d-shell in the transitionmetals. ferromagnetic compounds of manganese with perovskite structure. *Physics Review*, 82(3):403–405, (1951).

[13] N. A. Hill. Why are there so few magnetic ferroelectrics? *Journal of Physical Chemistry B*, 104:6694–6709, (2000).

[14] R. Ramesh and N. A. Spaldin. Multiferroics: progress and prospects in thin films. *Nature Materials.*, 6(1):21–29, (2007).

[15] E. Bousquet, M. Dawber, N. Stucki, C. Lichtensteiger, P. Hermet, S. Gariglio, J. M. Triscone, and P. Ghosez. Improper ferroelectricity in perovskite oxide artificial superlattices. *Nature*, 452(7188):732–U4, (2008).

[16] A. P. Levanyuk and D. G. Sannikov. Improper ferroelectrics. *Sov. Phys.-Usp*, 17(2):199–214, (1974).

[17] A. M. dos Santos, S. Parashar, A. R. Raju, Y. S. Zhao, A. K. Cheetham, and C. N. R. Rao. Evidence for the likely occurence of magnetoferroelectricity in the simple perovskite $BiMnO_3$. *Solid State Communications*, 122:49–52, (2002).

[18] R. Seshadri and N. A. Hill. Visualizing the role of Bi 6s lone pairs in the off-center distortion in ferromagnetic $BiMnO_3$. *Chemistry of Materials*, 13(9):2892–2899, (2001).

[19] J. Wang, J. B. Neaton, H. Zheng, V. Nagarajan, S. B. Ogale, B. Liu, D. Viehland, V. Vaithyanathan, D. G. Schlom, U. V. Waghmare, N. A. Spaldin, K. M. Rabe, M. Wuttig, and R. Ramesh. Epitaxial $BiFeO_3$ multiferroic thin film heterostructures. *Science*, 299(5613):1719–1722, (2003).

[20] A. M. dos Santos, A. K. Cheetham, T. Atou, Y. Syono, Y. Yamaguchi, K. Ohoyama, H. Chiba, and C. N. R. Rao. Orbital ordering as the determinant for ferromagnetism in biferroic $BiMnO_3$. *Physical Review B*, 66(064425), (2002).

[21] C. H. Yang, J. Koo, C. Song, T. Y. Koo, K. B. Lee, and Y. H. Jeong. Resonant x-ray scattering study on multiferroic $BiMnO_3$. *Physical Review B*, 73(224112), (2006).

[22] M. Gajek, M. Bibes, S. Fusil, K. Bouzehouane, J. Fontcuberta, A. E. Barthelemy, and A. Fert. Tunnel junctions with multiferroic barriers. *Nature Materials*, 6(4):296–302, (2007).

[23] T. Zhao, A. Scholl, F. Zavaliche, K. Lee, M. Barry, A. Doran, M. P. Cruz, Y. H. Chu, C. Ederer, N. A. Spaldin, R. R. Das, D. M. Kim, S. H. Baek, C. B. Eom, and R. Ramesh. Electrical control of antiferromagnetic domains in multiferroic $BiFeO_3$ films at room temperature. *Nature Materials*, 5(10):823–829, (2006).

[24] D. Lebeugle, D. Colson, A. Forget, M. Viret, A. M. Bataille, and A. Gukasov. Electric-field-induced spin flop in BiFeO(3) single crystals at room temperature. *Physical Review Letters*, 100(227602), (2008).

[25] C. Ederer and C.J. Fennie. Electric-field switchable magnetization via the dzyaloshinskii-moriya interaction: $FeTiO_3$ versus $BiFeO_3$. *Journal of Physics-Condensed Matter*, 20(434219), (2008).

[26] L. W. Martin, Y. H. Chu, M. B. Holcomb, M. Huijben, P. Yu, S. J. Han, D. Lee, S. X. Wang, and R. Ramesh. Nanoscale control of exchange bias with $BiFeO_3$ thin films. *Nano Letters*, 8(7):2050–2055, (2008).

[27] S.W. Cheong and M. Mostovoy. Multiferroics: a magnetic twist for ferroelectricity. *Nature Materials*, 6(1):13–20, (2007).

[28] Y. Tokura and S. Seki. Multiferroics with spiral spin orders. *Advanced Materials*, 22(14):1554–1565, 2010.

[29] B. B. Van Aken, T. T. M. Palstra, A. Filippetti, and N. A. Spaldin. The origin of ferroelectricity in magnetoelectric $YMnO_3$. *Nature Materials*, 3(3):164–170, (2004).

[30] C.J. Fennie and K. M. Rabe. Ferroelectric transition in $YMnO_3$ from first principles. *Physical Review B*, 72(100103(R)), (2005).

[31] T. Katsufuji, S. Mori, M. Masaki, Y. Moritomo, N. Yamamoto, and H. Takagi. Dielectric and magnetic anomalies and spin frustration in hexagonal $RMnO_3$ (R = Y, Yb, and Lu). *Physical Review B*, 64(104419), (2001).

[32] D. V. Efremov, J. Van den Brink, and D. I. Khomskii. Bond-versus site-centred ordering and possible ferroelectricity in manganites. *Nature Materials*, 3(12):853–856, (2004).

[33] Y. Tokunaga, T. Lottermoser, Y. Lee, R. Kumai, M. Uchida, T. Arima, and Y. Tokura. Rotation of orbital stripes and the consequent charge-polarized state in bilayer manganites. *Nature Materials*, 5(12):937–941, (2006).

[34] N. Ikeda, H. Ohsumi, K. Ohwada, K. Ishii, T. Inami, K. Kakurai, Y. Murakami, K. Yoshii, S. Mori, Y. Horibe, and H. Kito. Ferroelectricity from iron valence ordering in the charge-frustrated system $LuFe_2O_4$. *Nature*, 436(7054):1136–1138, (2005).

[35] M. Kenzelmann, A. B. Harris, S. Jonas, C. Broholm, J. Schefer, S. B. Kim, C. L. Zhang, S. W. Cheong, O. P. Vajk, and J. W. Lynn. Magnetic inversion symmetry breaking and ferroelectricity in $TbMnO_3$ (R = Y, Yb, and Lu). *Physical Review Letters*, 95(087206), (2005).

[36] C. J. Fennie and K. M. Rabe. Magnetic and electric phase control in epitaxial $EuTiO_3$ from first principles. *Physical Review Letters*, 97(267602), (2006).

[37] P. J. Ryan, J. W. Kim, T. Birol, P. Thompson, J. H. Lee, X. Ke, P. S. Normile, E. Karapetrova, P. Schiffer, S. D. Brown, C. J. Fennie, and D. G. Schlom. Reversible control of magnetic interactions by electric field in a single-phase material. *Nature Communications*, 4(1334), (2013).

[38] J. M. Rondinelli, S. J. May, and J. W. Freeland. Control of octahedral connectivity in perovskite oxide heterostructures: An emerging route to multifunctional materials discovery. *MRS Bulletin*, 37:261–270, (2012).

[39] J.B. Goodenough. Electronic and ionic transport properties and other physical aspects of perovskites. *Reports on Progress in Physics*, 67:1915–1993, (2004).

[40] A.M. Glazer. The classification of tilted octahedral in perovskites. *Acta Crystallographica, Section B (Structural Crystallography and Crystal Chemistry)*, B28(3384):3384–3392, (1972).

[41] W. Zhong and D. Vanderbilt. Competing structural instabilities in cubic perovskites. *Physical Review Letters*, 74(13):2587–2590, (1995).

[42] P. Ghosez, E. Cockayne, U. V. Waghmare, and K. M. Rabe. Lattice dynamics of $BaTiO_3$, $PbTiO_3$and $PbZrO_3$: a comparative first-principle study. *Physical Review B*, 60(2):836–843, (1999).

[43] J.B. Goodenough. Jahn-teller phenomena in solids. *Annual Review of Materials Science*, 28:1–27, (1998).

[44] Y. Tokura. Critical features of colossal magnetoresistive manganites. *Reports on Progress in Physics*, 69:797–851, (2006).

[45] M.L. Medarde. Structural, magnetic and electronic properties of $RNiO_3$ perovskites (R equals rare earth). *J. phys. Condes. Mater.*, 6(1679), (1997).

[46] J. S. Zhou, J. B. Goodenough, B. Dabrowski, P. W. Klamut, and Z. Bukowski. Enhanced susceptibility in $LNiO_3$ perovskites (L=La, Pr,Nd, $Nd_{0.5}Sm_{0.5}$). *Physical Review Letters*, 84(526), (2000).

[47] S. Ramanathan. *Thin film metal-oxides*. Springer, 2010.

[48] A. J. Hatt and N. A. Spaldin. Structural phases of strained $LaAlO_3$ driven by octahedral tilt instabilities). *Physical Review B*, 82(195402), (2010).

[49] B. J. Kim, H. Jin, S. J. Moon, J. Y. Kim, B. G. Park, C. S. Leem, J. Yu, T. W. Noh, C. Kim, S. J. Oh, J. H. Park, V. Durairaj, G. Cao, and E. Rotenberg. Novel J_{eff}=1/2 Mott state induced by relativistic spin-orbit coupling in Sr_2IrO_4. *Physical Review Letters*, 101(076402), (2008).

[50] M. Imada, A. Fujimori, and Y. Tokura. Metal-insulator transitions. *Reviews of Modern Physics*, 70(4), (1998).

[51] M. A. Senarisrodriguez and J. B. Goodenough. $LaCoO_3$ revisited. *Journal of Solid State Chemistry*, 116(2):224–231, (1995).

[52] M. A. Korotin, S. Y. Ezhov, I. V. Solovyev, V. I. Anisimov, D. I. Khomskii, and G. A. Sawatzky. Intermediate-spin state and properties of $LaCoO_3$. *Physical Review B*, 54(8):5309–5316, (1996).

[53] D. Fuchs, E. Arac, C. Pinta, S. Schuppler, R. Schneider, and H. V. von Lohneysen. Tuning the magnetic properties of $LaCoO_3$ thin films by epitaxial strain. *Physical Review B*, 77(014434), (2008).

[54] P. W. Anderson. Antiferromagnetism - theory of superexchange interaction. *Physical Review*, 79(2):350–356, (1950).

[55] J. B. Goodenough. Theory of the role of covalence in the perovskite-type manganites LA,M(II) MnO_3. *Physical Review*, 100(2):564–573, (1955).

[56] J. B. Goodenough. An interpretation of the magnetic properties of the perovskite-type mixed crystals $La_{1-X}Sr_XCoO_{3-LAMBDA}$. *Journal of Physics and Chemistry of Solids*, 6(2-3):287–297, (1958).

[57] J. Kanamori. Superexchange interaction and symmetry properties of electron orbitals. *Journal of Physics and Chemistry of Solids*, 10(2-3):87–98, (1959).

[58] H. Y. Hwang, Y. Iwasa, M. Kawasaki, B. Keimer, N. Nagaosa, and Y. Tokura. Emergent phenomena at oxide interfaces. *Nature Materials*, 11(2):103–113, (2012).

[59] J. Chakhalian, A. J. Millis, and J. Rondinelli. Whither the oxide interface. *Nature Materials*, 11(2):92–94, (2012).

[60] Pavlo Zubko, Stefano Gariglio, Marc Gabay, Philippe Ghosez, and Jean-Marc Triscone. Interface physics in complex oxide heterostructures. *Annual Review of Condensed Matter Physics*, 2:141–165, (2011).

[61] K. Ueda, H. Tabata, and T. Kawai. Ferromagnetism in $LaFeO_3$-$LaCrO_3$ superlattices. *Science*, 280(5366):1064–1066, (1998).

[62] A. Ohtomo and H. Y. Hwang. A high-mobility electron gas at the $LaAlO_3/SrTiO_3$ heterointerface. *Nature*, 427(6973):423–426, (2004).

[63] N. Nakagawa, H. Y. Hwang, and D. A. Muller. Why some interfaces cannot be sharp. *Nature Materials*, 5(3):204–209, (2006).

[64] J. Chakhalian, J. W. Freeland, H. U. Habermeier, G. Cristiani, G. Khaliullin, M. van Veenendaal, and B. Keimer. Orbital reconstruction and covalent bonding at an oxide interface. *Science*, 318(5853):1114–1117, (2007).

[65] M. Dawber, K. M. Rabe, and J. F. Scott. Physics of thin-film ferroelectric oxides. *Reviews of Modern Physics*, 77(4):1083–1130, (2005).

[66] J. D. Burton and E. Y. Tsymbal. Prediction of electrically induced magnetic reconstruction at the manganite/ferroelectric interface. *Physical Review B*, 80(17):6, (2009).

[67] C. A. F. Vaz, J. Hoffman, Y. Segal, J. W. Reiner, R. D. Grober, Z. Zhang, C. H. Ahn, and F. J. Walker. Origin of the magnetoelectric coupling effect in $Pb(Zr_{0.2}Ti_{0.8})O_3/La_{0.8}Sr_{0.2}MnO_3$ multiferroic heterostructures. *Physical Review Letters*, 104(12):4, (2010).

[68] J. M. Rondinelli, M. Stengel, and N. A. Spaldin. Carrier-mediated magnetoelectricity in complex oxide heterostructures. *Nature Nanotechnology*, 3(1):46–50, (2008).

[69] S. Zhang, Y. G. Zhao, P. S. Li, J. J. Yang, S. Rizwan, J. X. Zhang, J. Seidel, T. L. Qu, Y. J. Yang, Z. L. Luo, Q. He, T. Zou, Q. P. Chen, J. W. Wang, L. F. Yang, Y. Sun, Y. Z. Wu, X. Xiao, X. F. Jin, J. Huang, C. Gao, X. F. Han, and R. Ramesh. Electric-field control of nonvolatile magnetization in $Co_{40}Fe_{40}B_{20}/Pb(Mg_{1/3}Nb_{2/3})_{0.7}Ti_{0.3}O_3$ structure at room temperature. *Physical Review Letters*, 108(137203), (2012).

[70] Ce-Wen Nan, M. I. Bichurin, Shuxiang Dong, D. Viehland, and G. Srinivasan. Multiferroic magnetoelectric composites: Historical perspective, status, and future directions. *Journal of Applied Physics*, 103(3), (2008).

[71] J. T. Heron, M. Trassin, K. Ashraf, M. Gajek, Q. He, S. Y. Yang, D. E. Nikonov, Y. H. Chu, S. Salahuddin, and R. Ramesh. Electric-field-induced magnetization reversal in a ferromagnet-multiferroic heterostructure. *Physical Review Letters*, 107(227201), (2011).

[72] J. Nogues and I. K. Schuller. Exchange bias. *Journal of Magnetism and Magnetic Materials*, 192(2):203–232, (1999).

[73] V. Laukhin, V. Skumryev, X. Marti, D. Hrabovsky, F. Sanchez, M. V. Garcia-Cuenca, C. Ferrater, M. Varela, U. Luders, J. F. Bobo, and J. Fontcuberta. Electric-field control of exchange bias in multiferroic epitaxial heterostructures. *Physical Review Letters*, 97(227201), (2006).

[74] Y. H. Chu, L. W. Martin, M. B. Holcomb, M. Gajek, S. J. Han, Q. He, N. Balke, C. H. Yang, D. Lee, W. Hu, Q. Zhan, P. L. Yang, A. Fraile-Rodriguez, A. Scholl, S. X. Wang, and R. Ramesh. Electric-field control of local ferromagnetism using a magnetoelectric multiferroic. *Nature Materials*, 7(6):478–482, (2008).

[75] Y. H. Chu, Q. Zhan, L. W. Martin, M. P. Cruz, P. L. Yang, G. W. Pabst, F. Zavaliche, S. Y. Yang, J. X. Zhang, L. Q. Chen, D. G. Schlom, I. N. Lin, T. B. Wu, and R. Ramesh. Nanoscale domain control in multiferroic $BiFeO_3$ thin films. *Advanced Materials*, 18(17), (2006).

[76] J. T. Heron, J. L. Bosse, Q. He, Y. Gao, M. Trassin, L. Ye, J. D. Clarkson, C. Wang, J. Liu, S. Salahuddin, D. C. Ralph, D. G. Schlom, J. Iniguez, B. D. Huey, and R. Ramesh. Deterministic switching of ferromagnetism at room temperature using an electric field. *Nature*, 516(7531):370–+, (2014).

[77] P. R. Willmott. Deposition of complex multielemental thin films. *Progress in Surface Science*, 76(6-8):163–217, (2004).

[78] H. M. Christen and G. Eres. Recent advances in pulsed-laser deposition of complex oxides. *Journal of Physics-Condensed Matter*, 20(26):16, (2008).

[79] L. W. Martin, Y. H. Chu, and R. Ramesh. Advances in the growth and characterization of magnetic, ferroelectric, and multiferroic oxide thin films. *Materials Science and Engineering R Reports*, 68(4-6):III–133, (2010).

[80] D. G. Schlom, L. Q. Chen, X. Q. Pan, A. Schmehl, and M. A. Zurbuchen. A thin film approach to engineering functionality into oxides. *Journal of the American Ceramic Society*, 91(8):2429–2454, (2008).

[81] A. Ichimiya and P. I. Cohen. *Reflection high energy electron diffraction*. Cambridge University Press, Combridge, UK, 2004.

[82] Yoshio Waseda, Eiichiro Matsubara, and Kozo Shinodar. *X-Ray Diffraction Crystallography*. Springer-Verlag Berlin Heidelberg, 2011.

[83] H. Seeck Oliver. *Overview of X-Ray Scattering and Diffraction Theory and Techniques*, pages 1–28. Pan Stanford, 2015. doi:10.1201/b15674-2.

[84] Helmut Kohl and Ludwig Reimer. *Transmission Electron Microscopy*. Springer-Verlag New York, 2008.

[85] S. V. Kalinin, A. N. Morozovska, L. Q. Chen, and B. J. Rodriguez. Local polarization dynamics in ferroelectric materials. *Reports on Progress in Physics*, 73(5):67, (2010).

[86] N. Balke, I. Bdikin, S. V. Kalinin, and A. L. Kholkin. Electromechanical imaging and spectroscopy of ferroelectric and piezoelectric materials: State of the art and prospects for the future. *Journal of the American Ceramic Society*, 92(8):1629–1647, (2009).

[87] F. Zavaliche, R. R. Das, D. M. Kim, C. B. Eom, S. Y. Yang, P. Shafer, and R. Ramesh. Ferroelectric domain structure in epitaxial $BiFeO_3$ films. *Applied Physics Letters*, 87(18):182912, (2005).

[88] SLAC Stanford. Magnetic dichroism spectroscopy and microscopy. `www-ssrl.slac.stanford.edu/stohr/xmcd.htm`.

[89] J. Stohr. Exploring the microscopic origin of magnetic anisotropies with x-ray magnetic circular dichroism (xmcd) spectroscopy. *Journal of Magnetism and Magnetic Materials*, 200(1-3):470–497, (1999).

[90] P. Fischer, M. Polomska, I. Sosnowska, and M. Szymanski. Temperature-dependence of the crystal and magnetic-structures of $BiFeO_3$. *Journal of Physics C-Solid State Physics*, 13(10):1931–1940, (1980).

[91] L. Martin, S. P. Crane, Y. H. Chu, M. B. Holcomb, M. Gajek, M. Huijben, C. H. Yang, N. Balke, and R. Ramesh. Multiferroics and magnetoelectrics: thin films and nanostructures. *Journal of Physics-Condensed Matter*, 20(43):13, (2008).

[92] J. R. Teague, R. Gerson, and W. J. James. Dielectric hysteresis in single crystal $BiFeO_3$. *Solid State Communications*, 8(13):1073, (1970).

[93] D. Lebeugle, D. Colson, A. Forget, M. Viret, P. Bonville, J. F. Marucco, and S. Fusil. Room-temperature coexistence of large electric polarization and magnetic order in $BiFeO_3$ single crystals. *Physical Review B*, 76(2):8, (2007).

[94] R. Haumont, J. Kreisel, P. Bouvier, and F. Hippert. Phonon anomalies and the ferroelectric phase transition in multiferroic $BiFeO_3$. *Physical Review B*, 73(13):4, (2006).

[95] I. Sosnowska, T. Peterlinneumaier, and E. Steichele. Spiral magnetic-ordering in bismuth ferrite. *Journal of Physics C-Solid State Physics*, 15(23):4835–4846, (1982).

[96] M. B. Holcomb, L. W. Martin, A. Scholl, Q. He, P. Yu, C. H. Yang, S. Y. Yang, P. A. Glans, M. Valvidares, M. Huijben, J. B. Kortright, J. Guo, Y. H. Chu,

and R. Ramesh. Probing the evolution of antiferromagnetism in multiferroics. *Physical Review B*, 81(13):6, (2010).

[97] D. Sando, A. Agbelele, D. Rahmedov, J. Liu, P. Rovillain, C. Toulouse, I. C. Infante, A. P. Pyatakov, S. Fusil, E. Jacquet, C. Carretero, C. Deranlot, S. Lisenkov, D. Wang, J. M. Le Breton, M. Cazayous, A. Sacuto, J. Juraszek, A. K. Zvezdin, L. Bellaiche, B. Dkhil, A. Barthelemy, and M. Bibes. Crafting the magnonic and spintronic response of $BiFeO_3$ films by epitaxial strain. *Nature Materials*, 12(7):641–646, (2013).

[98] S. Jin, T. H. Tiefel, M. McCormack, R. A. Fastnacht, R. Ramesh, and L. H. Chen. Thousandfold change in resistivity in magnetoresistive La-Ca-Mn-O films. *Science*, 264(5157):413–415, (1994).

[99] H. Fujishiro, T. Fukase, and M. Ikebe. Charge ordering and sound velocity anomaly in $La_{1-x}Sr_xMnO_3$ (X$\geq$0.5). *Journal of the Physical Society of Japan*, 67(8):2582–2585, (1998).

[100] B. Nadgorny, II Mazin, M. Osofsky, R. J. Soulen, P. Broussard, R. M. Stroud, D. J. Singh, V. G. Harris, A. Arsenov, and Y. Mukovskii. Origin of high transport spin polarization in $La_{0.7}Sr_{0.3}MnO_3$: Direct evidence for minority spin states. *Physical Review B*, 63(18):5, (2001).

[101] P. Yu, J. S. Lee, S. Okamoto, M. D. Rossell, M. Huijben, C. H. Yang, Q. He, J. X. Zhang, S. Y. Yang, M. J. Lee, Q. M. Ramasse, R. Erni, Y. H. Chu, D. A. Arena, C. C. Kao, L. W. Martin, and R. Ramesh. Interface ferromagnetism and orbital reconstruction in $BiFeO_3$-$La_{0.7}Sr_{0.3}MnO_3$ heterostructures. *Physical Review Letters*, 105(2):5, (2010).

[102] W. H. Meiklejohn and C. P. Bean. New magnetic anisotropy. *Physical Review*, 102(5):1413–1414, (1956).

[103] S. S. P. Parkin, K. P. Roche, M. G. Samant, P. M. Rice, R. B. Beyers, R. E. Scheuerlein, E. J. O'Sullivan, S. L. Brown, J. Bucchigano, D. W. Abraham, Y. Lu, M. Rooks, P. L. Trouilloud, R. A. Wanner, and W. J. Gallagher. Exchange-biased magnetic tunnel junctions and application to nonvolatile magnetic random access memory (invited). *Journal of Applied Physics*, 85(8):5828–5833, (1999).

[104] M. Kiwi. Exchange bias theory. *Journal of Magnetism and Magnetic Materials*, 234(3):584–595, (2001).

[105] R. L. Stamps. Mechanisms for exchange bias. *Journal of Physics D-Applied Physics*, 33(23):R247–R268, (2000).

[106] S. M. Wu, S. A. Cybart, P. Yu, M. D. Rossell, J. X. Zhang, R. Ramesh, and R. C. Dynes. Reversible electric control of exchange bias in a multiferroic field-effect device. *Nature Materials*, 9(9):756–761, (2010).

[107] S. M. Wu, S. A. Cybart, D. Yi, J. M. Parker, R. Ramesh, and R. C. Dynes. Full electric control of exchange bias. *Physical Review Letters*, 110(6):5, (2013).

[108] H. Yamada, Y. Ogawa, Y. Ishii, H. Sato, M. Kawasaki, H. Akoh, and Y. Tokura. Engineered interface of magnetic oxides. *Science*, 305(5684):646–648, (2004).

[109] B. H. Moeckly and K. Char. Properties of interface-engineered high T-c Josephson junctions. *Applied Physics Letters*, 71(17):2526–2528, (1997).

[110] M. Kawasaki, K. Takahashi, T. Maeda, R. Tsuchiya, M. Shinohara, O. Ishiyama, T. Yonezawa, M. Yoshimoto, and H. Koinuma. Atomic control of the $SrTiO_3$ crystal-surface. *Science*, 266(5190):1540–1542, (1994).

[111] P. Yu, W. Luo, D. Yi, J. X. Zhang, M. D. Rossell, C. H. Yang, L. You, G. Singh-Bhalla, S. Y. Yang, Q. He, Q. M. Ramasse, R. Erni, L. W. Martin, Y. H. Chu, S. T. Pantelides, S. J. Pennycook, and R. Ramesh. Interface control of bulk ferroelectric polarization. *Proceedings of the National Academy of Sciences of the United States of America*, 109(25):9710–9715, (2012).

[112] G. Rijnders, D. H. A. Blank, J. Choi, and C. B. Eom. Enhanced surface diffusion through termination conversion during epitaxial $SrRuO_3$ growth. *Applied Physics Letters*, 84(4):505–507, (2004).

[113] F. Zavaliche, S. Y. Yang, T. Zhao, Y. H. Chu, M. P. Cruz, C. B. Eom, and R. Ramesh. Multiferroic $BiFeO_3$ films: domain structure and polarization dynamics. *Phase Transitions*, 79(12):991–1017, (2006).

[114] Hajo J. A. Molegraaf, Jason Hoffman, Carlos A. F. Vaz, Stefano Gariglio, Dirk van der Marel, Charles H. Ahn, and Jean-Marc Triscone. Magnetoelectric effects in complex oxides with competing ground states. *Advanced Materials*, 21(34):3470–3474, (2009).

[115] X. Hong, A. Posadas, and C. H. Ahn. Examining the screening limit of field effect devices via the metal-insulator transition. *Applied Physics Letters*, 86(14):142501, (2005).

[116] V. H. Ahn, T. Lookman, and A. R. Bishop. Strain-induced metal-insulator phase coexistence in perovskite manganites. *Nature*, 428(6981):401–404, (2004).

[117] Z. Jirak, F. Damay, M. Hervieu, C. Martin, B. Raveau, G. Andre, and F. Bouree. Magnetism and charge ordering in $Pr_{0.5}Ca_xSr_{0.5-x}MnO_3$ (x=0.09 and 0.5). *Physical Review B*, 61(2):1181–1188, (2000).

[118] O. Chmaissem, B. Dabrowski, S. Kolesnik, J. Mais, J. D. Jorgensen, and S. Short. Structural and magnetic phase diagrams of $La_{1-x}Sr_xMnO_3$ and $Pr_{1-y}Sr_yMnO_3$. *Physical Review B*, 67(9):094431, (2003).

[119] O. Chmaissem, B. Dabrowski, S. Kolesnik, J. Mais, L. Suescun, and J. D. Jorgensen. Effects of internal structural parameters on the properties of ba-substituted $La_{0.5}Sr_{0.5}MnO_3$. *Physical Review B*, 74(14):10, (2006).

[120] J. C. Loudon, N. D. Mathur, and P. A. Midgley. Charge-ordered ferromagnetic phase in $La_{0.5}Ca_{0.5}MnO_3$. *Nature*, 420(6917):797–800, (2002).

[121] P. G. Radaelli, D. E. Cox, M. Marezio, and S. W. Cheong. Charge, orbital, and magnetic ordering in $La_{0.5}Ca_{0.5}MnO_3$. *Physical Review B*, 55(5):3015–3023, (1997).

[122] Di Yi, Jian Liu, Satoshi Okamoto, Suresha Jagannatha, Yi-Chun Chen, Pu Yu, Ying-Hao Chu, Elke Arenholz, and R. Ramesh. Tuning the competition between ferromagnetism and antiferromagnetism in a half-doped manganite through magnetoelectric coupling. *Physical Review Letters*, 111(12):127601, (2013).

[123] H. Ohldag, T. J. Regan, J. Sthr, A. Scholl, F. Nolting, J. Lning, C. Stamm, S. Anders, and R. L. White. Spectroscopic identification and direct imaging of interfacial magnetic spins. *Physical Review Letters*, 87(24):247201, (2001).

[124] J. Chakhalian, J. W. Freeland, G. Srajer, J. Strempfer, G. Khaliullin, J. C. Cezar, T. Charlton, R. Dalgliesh, C. Bernhard, G. Cristiani, H. U. Habermeier, and B. Keimer. Magnetism at the interface between ferromagnetic and superconducting oxides. *Nat Phys*, 2(4):244–248, (2006).

[125] H Bea, M Bibes, A Barthlmy, K Bouzehouane, E Jacquet, A Khodan, J-P Contour, S Fusil, F Wyczisk, and A Forget. Influence of parasitic phases on the properties of $BiFeO_3$ epitaxial thin films. *Applied Physics Letters*, 87(7):072508–072508–3, (2005).

[126] Claude Ederer and Nicola A. Spaldin. Weak ferromagnetism and magnetoelectric coupling in bismuth ferrite. *Physical Review B*, 71(6):060401, (2005).

[127] H. Kawano, R. Kajimoto, M. Kubota, and H. Yoshizawa. Canted antiferromagnetism in an insulating lightly doped $La_{1-x}Sr_xMnO_3$ with $x \leq 0.17$. *Physical Review B*, 53(5):2202–2205, (1996).

[128] I. V. Solovyev and K. Terakura. Spin canting in three-dimensional perovskite manganites. *Physical Review B*, 63(17):174425, (2001).

[129] C. T. Chen, Y. U. Idzerda, H. J. Lin, N. V. Smith, G. Meigs, E. Chaban, G. H. Ho, E. Pellegrin, and F. Sette. Experimental confirmation of the x-ray magnetic circular dichroism sum rules for iron and cobalt. *Physical Review Letters*, 75(1):152–155, (1995).

[130] D. Pesquera, G. Herranz, A. Barla, E. Pellegrin, F. Bondino, E. Magnano, F. Snchez, and J. Fontcuberta. Surface symmetry-breaking and strain effects on orbital occupancy in transition metal perovskite epitaxial films. *Nat Commun*, 3:1189, (2012).

[131] Y. Takamura, F. Yang, N. Kemik, E. Arenholz, M. D. Biegalski, and H. M. Christen. Competing interactions in ferromagnetic/antiferromagnetic perovskite superlattices. *Physical Review B*, 80(18):180417, (2009).

[132] M. Varela, M. P. Oxley, W. Luo, J. Tao, M. Watanabe, A. R. Lupini, S. T. Pantelides, and S. J. Pennycook. Atomic-resolution imaging of oxidation states in manganites. *Physical Review B*, 79(8):085117, (2009).

[133] S. P. Cramer, F. M. F. DeGroot, Y. Ma, C. T. Chen, F. Sette, C. A. Kipke, D. M. Eichhorn, M. K. Chan, and W. H. Armstrong. Ligand field strengths and oxidation states from manganese L-edge spectroscopy. *Journal of the American Chemical Society*, 113(21):7937–7940, (1991).

[134] Jiefang Li, Junling Wang, M. Wuttig, R. Ramesh, Naigang Wang, B. Ruette, A. P. Pyatakov, A. K. Zvezdin, and D. Viehland. Dramatically enhanced polarization in (001), (101), and (111)$BiFeO_3$ thin films due to epitiaxial-induced transitions. *Applied Physics Letters*, 84(25):5261–5263, (2004).

[135] Satoshi Okamoto. Magnetic interaction at an interface between manganite and other transition metal oxides. *Physical Review B*, 82(2):024427, (2010).

[136] I. V. Solovyev and K. Terakura. Magnetic spin origin of the charge-ordered phase in manganites. *Physical Review Letters*, 83(14):2825–2828, (1999).

[137] Jeroen van den Brink, Giniyat Khaliullin, and Daniel Khomskii. Charge and orbital order in half-doped manganites. *Physical Review Letters*, 83(24):5118–5121, (1999).

[138] G. Q. Gong, C. L. Canedy, Gang Xiao, J. Z. Sun, A. Gupta, and W. J. Gallagher. Colossal magnetoresistance in the antiferromagnetic $La_{0.5}Ca_{0.5}MnO_3$ system. *Journal of Applied Physics*, 79(8):4538–4540, (1996).

[139] M. Uehara, S. Mori, C. H. Chen, and S. W. Cheong. Percolative phase separation underlies colossal magnetoresistance in mixed-valent manganites. *Nature*, 399(6736):560–563, (1999).

[140] M. Huijben, L. W. Martin, Y. H. Chu, M. B. Holcomb, P. Yu, G. Rijnders, D. H. A. Blank, and R. Ramesh. Critical thickness and orbital ordering in ultrathin $La_{0.7}Sr_{0.3}MnO_3$ films. *Physical Review B*, 78(9):7, (2008).

[141] X. Hong, A. Posadas, and C. H. Ahn. Examining the screening limit of field effect devices via the metal-insulator transition. *Applied Physics Letters*, 86(14):3, (2005).

[142] D. Gutierrez, G. Radaelli, F. Sanchez, R. Bertacco, and J. Fontcuberta. Bandwidth-limited control of orbital and magnetic orders in half-doped manganites by epitaxial strain. *Physical Review B*, 89(7):8, (2014).

[143] E. Y. Tsymbal and H. Kohlstedt. Applied physics - tunneling across a ferroelectric. *Science*, 313(5784):181–183, (2006).

[144] Y. W. Yin, J. D. Burton, Y. M. Kim, A. Y. Borisevich, S. J. Pennycook, S. M. Yang, T. W. Noh, A. Gruverman, X. G. Li, E. Y. Tsymbal, and Qi Li. Enhanced tunnelling electroresistance effect due to a ferroelectrically induced phase transition at a magnetic complex oxide interface. *Nat Mater*, 12(5):397–402, (2013).

[145] M. Nakamura, Y. Ogimoto, H. Tamaru, N. Izumi, and K. Miyano. Phase control through anisotropic strain in $Nd_{0.5}Sr_{0.5}MnO_3$ thin films. *Applied Physics Letters*, 86(18):3, (2005).

[146] Y. Wakabayashi, D. Bizen, H. Nakao, Y. Murakami, M. Nakamura, Y. Ogimoto, K. Miyano, and H. Sawa. Novel orbital ordering induced by anisotropic stress in a manganite thin film. *Physical Review Letters*, 96(1), (2006).

[147] S. Shimomura, K. Tajima, N. Wakabayashi, S. Kobayashi, H. Kuwahara, and Y. Tokura. Effect of magnetic transitions and charge-ordering on crystal lattice in $Nd_{0.5}Sr_{0.5}MnO_3$. *Journal of the Physical Society of Japan*, 68(6):1943–1947, (1999).

[148] Yusuke Wakabayashi, Daisuke Bizen, Yugo Kubo, Hironori Nakao, Youichi Murakami, Masao Nakamura, Yasushi Ogimoto, Kenjiro Miyano, and Hiroshi Sawa. Orbital ordering structures in $(Nd,Pr)_{0.5}Sr_{0.5}MnO_3$ manganite thin films on perovskite (011) substrates. *Journal of the Physical Society of Japan*, 77(1), (2008).

[149] C. H. Du, M. E. Ghazi, P. D. Hatton, S. P. Collins, B. M. Murphy, B. G. Kim, and S. W. Cheong. Study of the phase transition and charge ordering in single-crystalline $Nd_{1/2}Sr_{1/2}MnO_3$ using x-ray scattering. *Journal of Applied Physics*, 104(2), (2008).

[150] J. Herrero-Martin, J. Garcia, G. Subias, J. Blasco, M. C. Sanchez, and S. Stanescu. Double stripe ordering in $Nd_{0.5}Sr_{0.5}MnO_3$ determined by resonant soft x-ray scattering. *Physical Review B*, 73(22), (2006).

[151] R. C. Yu, J. Tang, L. D. Yao, A. Matsushita, Y. Yu, F. Y. Li, and C. Q. Jin. Conjectured orbital ordering behavior of $Nd_{0.5}Sr_{0.5}MnO_3$ under high pressures. *Journal of Applied Physics*, 97(8), (2005).

[152] J. Z. Wang, J. R. Sun, W. Zhang, R. C. Yu, Y. Z. Chen, B. G. Shen, and W. B. Wu. Pressure effects on the charge ordering in $Bi_{0.4}Ca_{0.6}MnO_3$ films of different orientation. *Epl*, 82(1):6, (2008).

[153] K. Miyasaka, M. Nakamura, Y. Ogimoto, H. Tamaru, and K. Miyano. Ultrafast photoinduced magnetic moment in a charge-orbital-ordered antiferromagnetic $Nd_{0.5}Sr_{0.5}MnO_3$ thin film. *Physical Review B*, 74(1), (2006).

[154] N. Fukumoto, S. Mori, N. Yamamoto, Y. Moritomo, T. Katsufuji, C. H. Chen, and S. W. Cheong. Microscopic electronic phase separation and metal-insulator transition in $Nd_{0.5}Sr_{0.5}MnO_3$. *Physical Review B*, 60(18):12963–12967, (1999).

[155] Keji Lai, Masao Nakamura, Worasom Kundhikanjana, Masashi Kawasaki, Yoshinori Tokura, Michael A. Kelly, and Zhi-Xun Shen. Mesoscopic percolating resistance network in a strained manganite thin film. *Science*, 329(5988):190–193, (2010).

[156] M. Shayegan, K. Karrai, Y. P. Shkolnikov, K. Vakili, E. P. De Poortere, and S. Manus. Low-temperature, in situ tunable, uniaxial stress measurements in semiconductors using a piezoelectric actuator. *Applied Physics Letters*, 83(25):5235–5237, (2003).

[157] S. Kasahara, H. J. Shi, K. Hashimoto, S. Tonegawa, Y. Mizukami, T. Shibauchi, K. Sugimoto, T. Fukuda, T. Terashima, A. H. Nevidomskyy, and Y. Matsuda. Electronic nematicity above the structural and superconducting transition in $BaFe_2(As1\text{-}xPx)_2$). *Nature*, 486(7403):382–385, (2012).

[158] J. H. Chu, H. H. Kuo, J. G. Analytis, and I. R. Fisher. Divergent nematic susceptibility in an iron arsenide superconductor. *Science*, 337(6095):710–712, (2012).

[159] B. J. Kim, H. Ohsumi, T. Komesu, S. Sakai, T. Morita, H. Takagi, and T. Arima. Phase-sensitive observation of a spin-orbital mott state in Sr_2IrO_4. *Science*, 323(5919):1329–1332, (2009).

[160] G. Cao, J. Bolivar, S. McCall, J. E. Crow, and R. P. Guertin. Weak ferromagnetism, metal-to-nonmetal transition, and negative differential resistivity in single-crystal Sr_2IrO_4. *Physical Review B*, 57(18):11039–11042, (1998).

[161] J. W. Kim, Y. Choi, J. Kim, J. F. Mitchell, G. Jackeli, M. Daghofer, J. van den Brink, G. Khaliullin, and B. J. Kim. Dimensionality driven spin-flop transition in layered iridates. *Physical Review Letters*, 109(3):5, (2012).

[162] S. J. Moon, H. Jin, K. W. Kim, W. S. Choi, Y. S. Lee, J. Yu, G. Cao, A. Sumi, H. Funakubo, C. Bernhard, and T. W. Noh. Dimensionality-controlled insulator-metal transition and correlated metallic state in 5d transition metal oxides $Sr_{n+1}Ir_nO_{3n+1}$ (n=1, 2, and infinity). *Physical Review Letters*, 101(22):4, (2008).

[163] J. M. Longo, J. A. Kafalas, and R. J. Arnott. Structure and properties of high and low pressure forms of $SrIrO_3$. *Journal of Solid State Chemistry*, 3(2):174, (1971).

[164] G. Cao, V. Durairaj, S. Chikara, L. E. DeLong, S. Parkin, and P. Schlottmann. Non-fermi-liquid behavior in nearly ferromagnetic $sriro_3$ single crystals. *Physical Review B*, 76(10):100402, (2007).

[165] F. X. Wu, J. Zhou, L. Y. Zhang, Y. B. Chen, S. T. Zhang, Z. B. Gu, S. H. Yao, and Y. F. Chen. Metal-insulator transition in $SrIrO_3$ with strong spin-orbit interaction. *Journal of Physics-Condensed Matter*, 25(12):8, (2013).

[166] J. Matsuno, K. Ihara, S. Yamamura, H. Wadati, K. Ishii, V. Shankar, H. Kee, and H. Takagi. Engineering spin-orbital magnetic insulator by tailoring superlattices. *arXiv*, 1401(1066), (2014).

[167] K. H. Kim, H. S. Kim, and M. J. Han. Electronic structure and magnetic properties of iridate superlattice $SrIrO_3/SrTiO_3$. *Journal of Physics-Condensed Matter*, 26(18):5, (2014).

[168] I. Fina, X. Marti, D. Yi, J. Liu, J. H. Chu, C. Rayan-Serrao, S. Suresha, A. B. Shick, J. elezn, T. Jungwirth, J. Fontcuberta, and R. Ramesh. Anisotropic magnetoresistance in an antiferromagnetic semiconductor. *Nat Commun*, 5, (2014).

[169] R. P. van Gorkom, J. Caro, T. M. Klapwijk, and S. Radelaar. Temperature and angular dependence of the anisotropic magnetoresistance in epitaxial Fe films. *Physical Review B*, 63(13), (2001).

[170] M. Izumi, Y. Ogimoto, Y. Okimoto, T. Manako, P. Ahmet, K. Nakajima, T. Chikyow, M. Kawasaki, and Y. Tokura. Insulator-metal transition induced by interlayer coupling in $La_{0.6}Sr_{0.4}MnO_3/SrTiO_3$ superlattices. *Physical Review B*, 64(6):6, (2001).

[171] M. Izumi, Y. Ogimoto, T. Manako, M. Kawasaki, and Y. Tokura. Interface effect and its doping dependence in $La_{1-x}Sr_xMnO_3/SrTiO_3$ supertattices. *Journal of the Physical Society of Japan*, 71(11):2621–2624, (2002).

[172] K. Steenbeck and R. Hiergeist. Magnetic anisotropy of ferromagnetic La-0.7(Sr, Ca)(0.3)MnO3 epitaxial films. *Applied Physics Letters*, 75(12):1778–1780, (1999).

[173] M. Ziese, H. C. Semmelhack, and P. Busch. Sign reversal of the magnetic anisotropy in $La_{0.7}A_{0.3}MnO_3$ (A=Ca, Sr, Ba) films. *Journal of Magnetism and Magnetic Materials*, 246(12):327–334, (2002).

[174] Y. Ando, A. N. Lavrov, and S. Komiya. Anisotropic magnetoresistance in lightly doped $La_{2-x}Sr_xCuO_4$: Impact of antiphase domain boundaries on the electron transport. *Physical Review Letters*, 90(24), (2003).

[175] M. Bibes, B. Martinez, J. Fontcuberta, V. Trtik, C. Ferrater, F. Sanchez, M. Varela, R. Hiergeist, and K. Steenbeck. Anisotropic magnetoresistance of (0 0 h), (0 h h) and (h h h) $La_{2/3}Sr_{1/3}MnO_3$ thin films on (001) Si substrates. *Journal of Magnetism and Magnetic Materials*, 211(1-3):206–211, (2000).

[176] P. Li, E. Y. Jiang, and H. L. Bai. Fourfold symmetric anisotropic magnetoresistance based on magnetocrystalline anisotropy and antiphase boundaries in reactive sputtered epitaxial Fe_3O_4 films. *Applied Physics Letters*, 96(9):3, (2010).

[177] Hans Boschker, Mercy Mathews, Peter Brinks, Evert Houwman, Arturas Vailionis, Gertjan Koster, Dave H. A. Blank, and Guus Rijnders. Uniaxial contribution to the magnetic anisotropy of $La_{0.67}Sr_{0.33}MnO_3$ thin films induced by orthorhombic crystal structure. *Journal of Magnetism and Magnetic Materials*, 323(21):2632–2638, (2011).

[178] M. Mathews, F. M. Postma, J. C. Lodder, R. Jansen, G. Rijnders, and D. H. A. Blank. Step-induced uniaxial magnetic anisotropy of $La_{0.67}Sr_{0.33}MnO_3$ thin films. *Applied Physics Letters*, 87(24):3, (2005).

[179] A. Y. Borisevich, H. J. Chang, M. Huijben, M. P. Oxley, S. Okamoto, M. K. Niranjan, J. D. Burton, E. Y. Tsymbal, Y. H. Chu, P. Yu, R. Ramesh, S. V. Kalinin, and S. J. Pennycook. Suppression of octahedral tilts and associated changes in electronic properties at epitaxial oxide heterostructure interfaces. *Physical Review Letters*, 105(8):4, (2010).

[180] J. He, A. Borisevich, S. V. Kalinin, S. J. Pennycook, and S. T. Pantelides. Control of octahedral tilts and magnetic properties of perovskite oxide heterostructures by substrate symmetry. *Physical Review Letters*, 105(22):4, (2010).

[181] J. M. Rondinelli and N. A. Spaldin. Substrate coherency driven octahedral rotations in perovskite oxide films. *Physical Review B*, 82(11):4, (2010).

[182] D. Haskel, G. Fabbris, Mikhail Zhernenkov, P. P. Kong, C. Q. Jin, G. Cao, and M. van Veenendaal. Pressure tuning of the spin-orbit coupled ground state in sr_2iro_4. *Physical Review Letters*, 109(2):027204, (2012).

[183] S. J. Mugavero, M. D. Smith, W. S. Yoon, and H. C. zur Loye. $Nd_2K_2IrO_7$ and $Sm_2K_2IrO_7$: Iridium(VI) oxides prepared under ambient pressure. *Angewandte Chemie-International Edition*, 48(1):215–218, (2009).

Appendix A

List of Symbols and Abbreviations

α - First order magnetoelectric coupling coefficient
χ^e - Electric susceptibility
χ^m - Magnetic susceptibility
Δ_{cf} - Crystal field
ξ_{so} - Spin-orbital coupling energy
H_C - Coercive field
H_{EB} - Exchange bias field
P_s Ferroelectric polarization
T_C - Ferroelectric or ferromagnetic Curie temperature
T_N - Neel temperature of an antiferromagent
t - Kinetic energy
U - Coulomb repulsion
2DEG - 2 dimensional electron gas
AF - Antiferromagnetic
AFM - Atomic force microscopy
ALS - Advanced Light Source
AMR - Anisotropic magnetoresistance
APS - Advanced Photon Source
BFO - $BiFeO_3$
CMR - Colossal magnetoresistance
CO - Charge ordering
DE - Double exchange
DM interaction - Dzyaloshinskii-Moriya interaction
EB - Exchange bias
EELS - Electron energy loss spectroscopy
FE - Ferroelectric
FET - Field-effect-transistor
FM - Ferromagnetic
HAADF - High-angle-annular-dark-field imaging

IP - In-plane
LBL - Layer-by-layer
LCMO - $La_{0.5}Ca_{0.5}MnO_3$
LSMO0.5 - $La_{0.5}Sr_{0.5}MnO_3$
LSMO - $La_{2/3}Sr_{1/3}MnO_3$
ME - magnetoelectric
MBE - Molecular beam epitaxy
NSMO - $Nd_{0.5}Sr_{0.5}MnO_3$
OO - Orbital ordering
OOP - Out-of-plane
PEEM - Photoemission electron microscopy
PFM - Piezoelectric force microscopy
PLD - Pulsed laser deposition
PZT - $Pb(Zr_xTi_{1-x})O_3$
RHEED - Reflection high energy electron diffraction
RSM - Reciprocal spacing mapping
SE - Super-exchange
S2IO4 - Sr_2IrO_4
SIO - $SrIrO_3$
SL - Superlattice
SO - Spin ordering
SOC - Spin-orbit coupling
SRO - $SrRuO_3$
STEM - Scanning transmission electron microscopy
STO - $SrTiO_3$
TEY - Total electron yield
TMO - Transition metal oxides
XAS - X-ray absorption
XMCD - X-Ray Magnetic Circular Dichroism
XMLD - X-Ray Magnetic Linear Dichroism
XRD - X-ray diffraction
YBCO - $(Y,Ca)Ba_2Cu_3O_7$